

Design of Apoferritin-Based Nanoparticle MRI Contrast Agents Through

Controlled Metal Deposition

By

Maria Veronica Clavijo Jordan

A Dissertation Presented in Partial Fulfillment  
of the Requirements for the Degree  
Doctor of Philosophy

Approved November 2012 by the  
Graduate Supervisory Committee:

Kevin Bennett, Chair  
Vikram Kodibagkar  
A Dean Sherry  
Xiao Wang  
Jeffery Yarger

ARIZONA STATE UNIVERSITY

December 2012

## ABSTRACT

Sensitivity is a fundamental challenge for *in vivo* molecular magnetic resonance imaging (MRI). Here, I improve the sensitivity of metal nanoparticle contrast agents by strategically incorporating pure and doped metal oxides in the nanoparticle core, forming a soluble, monodisperse, contrast agent with adjustable  $T_2$  or  $T_1$  relaxivity ( $r_2$  or  $r_1$ ). I first developed a simplified technique to incorporate iron oxides in apoferritin to form “magnetoferritin” for nM-level detection with  $T_{2^-}$  and  $T_{2^*}$  weighting. I then explored whether the crystal could be chemically modified to form a particle with high  $r_1$ . I first adsorbed  $Mn^{2+}$  ions to metal binding sites in the apoferritin pores. The strategic placement of metal ions near sites of water exchange and within the crystal oxide enhance  $r_1$ , suggesting a mechanism for increasing relaxivity in porous nanoparticle agents. However, the  $Mn^{2+}$  addition was only possible when the particle was simultaneously filled with an iron oxide, resulting in a particle with a high  $r_1$  but also a high  $r_2$  and making them undetectable with conventional  $T_1$ -weighting techniques. To solve this problem and decrease the particle  $r_2$  for more sensitive detection, I chemically doped the nanoparticles with tungsten to form a disordered W-Fe oxide composite in the apoferritin core. This configuration formed a particle with a  $r_1$  of  $4,870\text{mM}^{-1}\text{s}^{-1}$  and  $r_2$  of  $9,076\text{mM}^{-1}\text{s}^{-1}$ . These relaxivities allowed the detection of concentrations ranging from 20nM – 400nM *in vivo*, both passively injected and targeted to the kidney glomerulus. I further developed an MRI acquisition technique to distinguish particles based on  $r_2/r_1$ , and show that three nanoparticles of similar size can be distinguished *in vitro* and *in vivo* with MRI. This work forms the basis for a new, highly flexible inorganic approach to design nanoparticle contrast agents for molecular MRI.

## DEDICATION

Several people have inspired me to strive to be a better person. But I will always keep my family in the highest regard of all. It is them who I can thank for teaching me to always aim high, and persevere in order to succeed. They have not only loved me for who I am, but also taught me important values that I carry within me and try to live by every day.

Also, this wonderful experience would have never been the same without the support of my beautiful friends. Thank you all.

## ACKNOWLEDGMENTS

This accomplishment would have not been possible without the support, mentorship, and friendship of Dr. Kevin Bennett. His incredible scientific vision has been the cornerstone of his mentorship and as my journey ends under his supervision, I can only hope to take some of it with me. Also, I greatly acknowledge my laboratory peers for their friendship and always-insightful scientific input.

Given the interdisciplinary nature of this work, I could have not accomplished this without the scientific expertise from Emmanuel Soignard in the SQUID and XRD experiments and Marco Flores in the EPR experiments and simulations. Also, Karl Weiss and David Lowry have provided tremendous help with all electron microscopy experiments and analyses.

I would like to thank my thesis committee for dedicating time and effort to help me throughout this research. In particular, Dr. Dean Sherry, as his expert opinion and suggestions were instrumental to this work.

Finally, I would like to acknowledge the Arizona Science Foundation for the financial support during my first two years. Their support during those years provided with the necessary help to launch this PhD experience.

## TABLE OF CONTENTS

	Page
LIST OF TABLES .....	vi
LIST OF FIGURES .....	vii
CHAPTER	
1. AN INTRODUCTION TO MRI CONTRAST AGENTS.....	1
1.1 Introduction .....	1
1.2 The Basics of Magnetic Resonance Imaging .....	2
1.3 Magnetic Nanomaterials .....	7
1.3.1 Diamagnetic, Paramagnetic, Superparamagnetic and Ferromagnetic Nanomaterials .....	8
1.4 Contrast Agent Relaxivity.....	15
1.4.1 Solomon Bloembergen Model of Dipolar Longitudinal Relaxation and Coordination Spheres.....	18
1.4.2 Chemical Exchange Model and Static Dephasing Regime for Transverse Relaxation .....	20
1.5 Engineering High Relaxivity Nanoparticle Contrast Agents .....	22
1.5.1 Chemical Doping .....	22
1.6 Ligand and Crystal Field Manipulation of Spin State.....	25
1.7 Current Efforts on the Increase of Nanoparticle Based Contrast Agent Relaxivity .....	27
1.8 Biological Considerationf for the Design of Nanoparticle Based Contrast Agents .....	29

CHAPTER	Page
2. FERRITIN AS A NATURAL CONTRAST AGENT .....	35
2.1 Introduction.....	35
2.2 Materials and Methods.....	36
2.2.1 Materials.....	36
2.2.2 Simplified Synthesis of Magnetoferritin .....	36
2.2.3 Protein and Metal Concentration Assays .....	37
2.2.4 Electron Microscopy.....	38
2.2.5 Relaxometry at 1.5T.....	39
2.2.6 Protein Integrity Studies via Gel Electrophoresis, and Immunoprecipitation.....	39
2.2.7 <i>In vivo</i> Detection of Magnetoferritin Particles .....	41
2.3 Results and Discussion .....	42
2.3.1 Synthesis and Particle Characterization .....	42
2.3.2 Protein Integrity and Relaxivity .....	44
2.3.3 MRI of Magnetoferritin <i>in vivo</i> .....	48
2.4 Conclusions.....	49
3. FEASIBILITY STUDY OF APOFERRITIN AS A NANO REACTOR TO TUNE $r_2$ AND $r_1$ .....	51
3.1 Introduction.....	51
3.2 Materials and Methods.....	51
3.2.1 Materials.....	51
3.2.2 Synthesis of $Mn^{2+}$ Adsorbed to Magnetoferritin.....	51
3.2.3 Synthesis of Tungsten-Iron (WFe) Nanoparticles .....	52
3.2.4 Synthesis of $Mn^{2+}$ WFe Nanoparticles.....	53

CHAPTER	Page
3.2.5 Electron Microscopy.....	54
3.2.6 Protein and Metal Assays .....	55
3.2.7 Relaxometry .....	56
3.2.8 Electron Paramagnetic Resonance .....	56
3.2.9 <i>In vivo</i> Imaging .....	57
3.3 Results and Discussion.....	58
3.3.1 Synthesis and Particle Characterization .....	58
3.3.1.1 Mn <sup>2+</sup> Adsorbed to Hydrophilic Channels of Magnetoferritin .....	58
3.3.1.2 Tungsten-Iron (WFe) Filled Apoferritin .....	60
3.3.1.3 Mn <sup>2+</sup> Adsorbed to Tungsten-Iron Filled Apoferritin	58
3.3.2 Relaxivity and <i>In vivo</i> imaging .....	62
3.3.3 Solomon Bloembergen Morgan (SBM) Simulations..	68
3.3.4 Electron Paramagnetic Resonance .....	69
3.4 Conclusions.....	72
 4. CHARACTERIZATION OF TUNGSTEN-IRON (W-FE) APOFERRITIN NANOPARTICLE .....	74
4.1 Introduction.....	74
4.2 Methods.....	77
4.2.1 Synthesis of Paramagnetic WFe Nanoparticle.....	77
4.2.2 Concentration Assays and Relaxometry .....	78
4.2.3 Size Exclusion Chromatography .....	78
4.2.4 Transmission Electron Microscopy.....	78
4.2.5 Energy Dispersive Spectroscopy.....	79

CHAPTER	Page
4.2.6 Electron Energy Loss Spectroscopy.....	79
4.2.7 Selected Area Electron Diffraction.....	80
4.2.8 X-Ray Diffraction.....	80
4.2.9 Superconducting Quantum Interference Device Magnetometry .....	80
4.2.10 In Vitro and In Vivo MRI.....	81
4.3 Results and Discussion.....	82
4.3.1 Synthesis and Nanoparticle Characterization .....	82
4.3.2 Crystal Structure Characterization.....	84
4.3.3 Magnetic Properties and Relaxivity .....	89
4.3.4 <i>In vitro</i> Phantom and <i>In vivo</i> MRI .....	94
4.4 Conclusions.....	95
5. <i>IN VIVO</i> DETECTION OF TARGETED WFE APOFERRITIN NANOPARTICLES AND <i>IN VITRO</i> TOXICITY.....	
5.1 Introduction.....	97
5.2 Methods.....	98
5.2.1 Synthesis of Cationized Tungsten-Iron Nanoparticle “ParaCF” .....	98
5.2.2 Intravenous Injection of ParaCF in Adult Rats .....	98
5.2.3 <i>In Vivo</i> Detection of Kidney Glomeruli, Liver and Spleen with MRI .....	98
5.2.4 Immunohistochemistry.....	98
5.2.5 Cytotoxicity of WFe-Apoferritin Nanoparticles .....	99

CHAPTER	Page
5.3 Results and Discussion.....	100
5.3.1 <i>In Vivo</i> Detection of Kidney Glomeruli, with T <sub>1</sub> – Weighting Techniques .....	100
5.3.2 Immunohistochemistry.....	102
5.3.3 Cell Viability and Toxicity .....	103
5.4 Conclusions .....	104
6. SUMMARY AND FUTURE WORK .....	106
6.1 Summary .....	106
6.2 Future Work .....	107
6.2.1 Adding Color to MRI with Doped Iron Oxide Crystals Inside Apoferritin .....	107
6.2.2 Cell Labeling with WFe-Apoferritin Nanoparticles .....	111
6.2.3 Chemical Doping with Different Ligands.....	112
References .....	113
Appendix	
A IACUC PROTOCOL APPROVAL FOR ANIMAL EXPERIMENTATION .....	124
B LICENCES TO REPRODUCE COPYRIGHTED MATERIAL .....	126
C STATEMENT OF PERMISSION FROM CO-AUTHORS .....	131

## LIST OF TABLES

Table		Page
1.	Magnetoferritin Relaxivity Summary .....	44
2.	Mn <sup>2+</sup> Adsorbed to Magnetoferritin Relaxivity Summary.....	61
3.	Wfe-Apoferritin Relaxivity Summary .....	63
4.	Mn <sup>2+</sup> Adsorbed to Apoferritin-Apoferritin Relaxivity Summary.....	65
5.	EPR Parameter List.....	69
6.	EELS Atomic Ratios for Apoferritin-Apoferritin Cores .....	84

## LIST OF FIGURES

Figure		Page
1.	Interaction of a proton with an external magnetic field .....	2
2.	Paramagnetism and Curie-Weiss behavior .....	9
3.	Superparamagnetic magnetic response to external field .....	11
4.	Ferromagnetic magnetic domain movement .....	13
5.	Ferromagnetic magnetization hysteresis loop .....	14
6.	Intrinsic relaxation tissue times .....	16
7.	Simulated detection window based on particle $r_2/r_1$ .....	17
8.	Chemical doping and spinel crystal structure .....	25
9.	Crystal and ligand field orbital splitting of $Fe^{2+}$ .....	27
10.	TEM characterization of magnetoferritin.....	43
11.	Native gel electrophoresis and immunoprecipitation of magnetoferritin .....	45
12.	Magnetoferritin relaxometry at 1.5T .....	47
13.	Magnetoferritin in vivo inoculation.....	49
14.	$Mn^{2+}$ adsorbed to magnetoferritin schematic and TEM .....	60
15.	Schematic and TEM of Wfe-apoferritin nanoparticle .....	61
16.	Schematic and TEM of $Mn^{2+}$ adsorbed to Wfe-apoferritin nanoparticle .....	62
17.	In vivo inoculation of $Mn^{2+}$ magnetoferritin and detection with IRTruFISP .....	64
18.	Relaxivity profile of Wfe-apoferritin with different tungstate addition rates .....	65

Figure	Page
19. SBM simulations predict high per-ion relaxivity in nanoparticle based agents .....	69
20. EPR simulations and experimental fit of Mn <sup>2+</sup> adsorbed magnetoferritin nanoparticles.....	70
21. Spin-coupling schematic of Wfe-apoferritin crystal core.....	76
22. Size and particle integrity characterization of Wfe-Apoferritin .....	83
23. TEM, STEM, EDX, SAED, and HREM of Wfe-apoferritin .....	86
24. EELS Wfe-Apoferritin .....	88
25. SQUID Magnetometry of Wfe-apoferritin.....	90
26. Temperature dependend susceptibility and Curie-Weiss temperature of Wfe-apoferritin .....	91
27. ZFC and FC Magnetometry of Wfe-apoferritin .....	92
28. In vitro and In vivo passive imaging of Wfe-apoferritin at 7T .....	96
29. In vivo targeting of kidney glomerulus at 7T with paraCF.....	101
30. Immunohistochemistry of kidney sections .....	102
31. Viability and Cytotoxicity of Wfe-Apoferritin .....	103
32. Simulation of particle separation based on $r_2/r_1$ .....	109
33. Experimental separation of particles at 7T with two colors.....	110
34. In vitro differentiation of two particles at 7T .....	111

## CHAPTER 1

# AN INTRODUCTION TO MAGNETIC NANOMATERIALS AND MRI CONTRAST AGENTS

### 1.1 Introduction

Magnetic nanomaterials are useful to a wide range of potential medical applications, including thermal ablation, drug targeting, implantable biomaterials, cell tracking, and imaging contrast agent design. A detailed understanding of the physics of magnetism is helpful in both the creation of nanomaterials and in gaining an understanding of how they interact with the surroundings. Importantly, the understanding of material magnetism at the nanometer scale has increased as new materials have been developed. This increased understanding has led to further innovations in nanomagnetic material design and has opened the door to novel inter-disciplinary applications. For example, noninvasive imaging techniques and multimodal approaches to treatment are being advanced with an increased knowledge of the molecular makeup of individual patients. Concurrent with these rapid improvements in radiological techniques, drugs and imaging probes are being developed at the nanometer scale to interact with individual molecules *in vivo* with improved specificity, sensitivity, and pharmacodynamics.

The search for a fuller understanding of nanomagnetic materials has led to a bridge between very disparate academic fields. These fields ranging from physics, chemistry, materials science, and biology work together in understanding the underlying concepts of magnetic materials in the nanometer scale especially for the applications in medicine.

This thesis concentrates on the ability to tune the magnetic properties of materials in the nanometer scale in order to develop a rational design of nanoparticle contrast agents for molecular magnetic resonance imaging.

## 1.2 The Basics of Magnetic Resonance Imaging

Approximately 60% of the total body weight of an adult male is water (Silverthorn, 2004). Magnetic Resonance Imaging (MRI) takes advantage of the abundance of water in the body to be able to see water content in tissues in three dimensions. Specifically, the hydrogen protons in water are directly imaged with MRI. Proton spins in a magnetic field precess at a specific frequency depending on the nuclei and the isotope. This frequency is known as the Larmor frequency, determined by the field itself, and the nuclei's gyromagnetic ratio as follows.

$$\omega(x) = \gamma \cdot B(x) \tag{Eqn 1.}$$

This rotational motion sets in a magnetic moment that has the tendency of aligning with the external magnetic field as illustrated below.

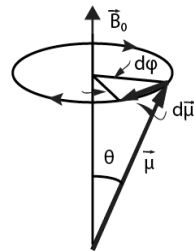


Figure 1. Interaction of a proton spin with an external magnetic field ( $B_0$ ) creating a current loop around the rotating axis. Adapted from Haacke B (B. R. Haacke M, 1999)

Hydrogen protons are in constant thermal energy exchange with the surrounding atoms (“lattice”). When a static field is applied, the magnetic energy is deposited into the proton’s overall energy and the protons align with the magnetic field in order to reach their minimum energy state. This new equilibrium state is preferred every time the spin ensemble is perturbed by external RF energy deposited in the sample. The rate at which this state of equilibrium is attained is characterized by the intrinsic properties of the proton and lattice interactions. The magnetization growth in the longitudinal direction is constrained by a time constant known as  $T_1$  or “longitudinal relaxation”.

The interaction of the magnetization vector with its surroundings has been described classically with the Bloch equations. These equations are the solutions to the differential equation relating the time varying magnetization to the growth and decay in longitudinal and transverse directions, respectively.

$$\frac{d\vec{M}}{dt} = \gamma\vec{M} \times \vec{B}_{ext} + \frac{1}{T_1}(M_0 - M_z)\hat{z} - \frac{1}{T_2}\vec{M}_\perp$$

*Eqn 2.*

In quantum terms, a population of protons exposed to an external static magnetic field has spins aligned either parallel or anti-parallel to the field. These states are then either  $m = +1/2$  or  $-1/2$ , being  $+1/2$  the state of lowest energy. Due to conservation of energy, a single spin transition from  $-1/2$  to  $+1/2$  does not occur without a transition up in energy from the lattice ( $+1/2$  to  $-1/2$ ). The rate of overall energy change from  $+1/2$  is determined using Schrödinger’s equation where the density of state change per unit energy is reduced as a finite state using a Dirac delta function. The rate of change is then identified as the spin-relaxation decay rate.

$$\frac{d(\Delta N)}{dt} = \frac{(\Delta N)_0 - \Delta N}{T_1} \quad \text{Eqn 3.}$$

Where N is the initial spin state either +1/2 or -1/2. And  $\Delta N$  is the spin excess of +1/2 over -1/2.

This equation is then manipulated in order to represent the magnetization in the z-direction and results in the following expression that matches the solution to the Bloch equation in the same direction where the rate of growth is characterized by the constant  $T_1$ .

$$\frac{dM_z}{dt} = \frac{M_0 - M_z}{T_1} \quad \text{Eqn 4.}$$

Spin-spin interactions among neighboring protons are represented by the decay rate in the transverse plane. Given that each precessing spin gives rise to an individual magnetic moment, one can visualize an individual spin as a minuscule magnet. If multiple minuscule magnets interact with one another, their local magnetic fields (although very small compared to the static  $B_0$ ) induce loss of spin coherence in the transverse plane. Due to this de-phasing effect, the magnetization in the transverse plane decays much faster than the growth in the longitudinal direction. These magnetization components are also the result from solving the differential equation introduced above.

$$\frac{dM_x}{dt} = \omega_0 M_y - \frac{M_x}{T_2} \quad \text{Eqn.5}$$

$$\frac{dM_y}{dt} = -\omega_0 M_x - \frac{M_y}{T_2} \quad \text{Eqn. 6}$$

There is also a contribution to the dephasing effect attributed to magnetic field inhomogeneities and this is described by the decay constant known as  $T_2^*$ .

Detecting the location of a specific population of spins is accomplished by means of their own magnetization and spatial encoding. Rotation of magnetization is accomplished by a “transmit coil”, a short radiofrequency (Karfeld, Bull, Davis, Meade, & Barron) pulse tuned to the resonance frequency “pushes” the magnetization vector toward a desired plane. By rotating the magnetization in a direction away from the equilibrium position (aligned with the static magnetic field) it is possible to perturb the spins and detect the changing flux via a secondary external coil. Much like in Faraday’s Law, a changing magnetic flux in a current loop induces an emf in an adjacent “receive coil”. This concept is explored and used to translate changing magnetic flux of the spin-generated magnetization into changing voltage in the receive coil. The general formula that relates *emf* to magnetization at a specific point source is the following (B. R. Haacke M, 1999).

$$emf = -\frac{d}{dt} \int_{sample} d^3r \vec{M}(\vec{r}, t) \cdot \vec{B}^{receive}(\vec{r}) \quad Eqn 7.$$

The addition of a spatially varying magnetic field confers the ability to spatially encode proton spins. Once the RF pulse excites the spin ensemble, it is possible to encode their locations by applying a gradient as shown in the equation below along the x-direction. Consequently, phase is accumulated over time.

$$\omega(x) = \gamma(B_0 + xG_x) \quad \text{Eqn 8.}$$

As the gradient is imposed in the sample, the signal coming from the detection coil is stored in 'K-space'. A typical cartesian coordinate K-space is a "grid" with all the signal information being stored following the following pattern.

$$K = \gamma \int G(\tau) d\tau \quad \text{Eqn 9.}$$

Phase encoded and frequency encoded information is stored in K-space and translated into image space via a half-space Fourier transform.

Collective spins are manipulated via a pre-determined sequence of RF pulses and gradient sets. These pulse sequences can be tailored to highlight and image specific structures in the body. For example, a pulse sequence that is heavily weighted in  $T_1$  changes in tissue is known as  $T_1$ -weighted pulse sequence. Similarly, sequences that are heavily weighed in  $T_2$  changes in tissue are known as  $T_2$ -weighted pulse sequences. There are a myriad of pulse sequences that have been developed for various applications in the last decades. Acquiring the MRI signal can be done in multiple ways, most pulse sequences are very versatile as the acquisition and manipulation scheme have multiple parameters such as the echo time, repetition time, inversion time, flip angle etc. By carefully selecting these parameters, it is possible to weight a certain signal to be highly sensitive to  $T_1$ ,  $T_2$ , diffusion coefficient, proton density etc.

Here, for simplicity, the signal equation for a spin echo pulse sequence is presented.

$$S = M_0(1 - 2e^{-(TR-TE/2)/T_1} + e^{-TR/T_1})e^{-TE/T_2}$$

*Eqn 10.*

In this equation, the signal is highly dependent on the echo times (TE), and repetition time (TR). The signal is weighted towards  $T_1$  tissues for a short TE and TR, while it is more  $T_2$  weighted when TE and TRs are long.

It is evident that if the intrinsic  $T_1$  and  $T_2$  could be reduced, the signal could be enhanced. This is the premise behind the use of exogenous contrast agents as they can alter the  $T_1$  and  $T_2$  of surrounding water protons and, hence, create local enhancement or decrease of signal. This paves the way for intensive research efforts towards the development of highly efficient contrast agents composed of magnetic materials.

### 1.3 Magnetic Nanomaterials

Magnetic materials are commonly synthesized from metals, such as transition or rare earth metals, to form a crystal. The magnetism of a material can be described classically by a net magnetic moment. Single-atom, paramagnetic materials have localized, unpaired valence electrons that give rise to the magnetic moment. The magnetic moment of a paramagnet increases approximately linearly with the strength of an applied field. This behavior is described by the susceptibility, which is the slope of the magnetization vs. field strength. The magnetic moment of a multi-atom crystal is not necessarily related to the magnetic susceptibility of each single atom due to the interactions between the individual electronic distributions. Here, I first describe the atomic basis of magnetism, and then provide an overview of how magnetism is formed in multi-atom macroscopic and nanometer-scale materials.

The basis of magnetism is spin, which is a fundamental property of matter. There are two major considerations to the interactions of electrons and the effect of the magnetism in solids: 1) Coulomb's repulsion between electrons and attraction to protons, and 2) Pauli's exclusion principle and the fact that electrons of the same spin state (up or down) cannot occupy the same orbital. These electromagnetic interactions result in the familiar electronic orbital around the atom. If the sum of these interactions results in a partially filled electronic shell, it creates a net magnetic moment in the atom. This is often the case for transition metals, leading to the complex interaction between electrons of neighboring atoms. The electronic distribution in transition metals can be complex. For example, in these metals, the 3d orbital has a localized but asymmetric distribution around the nucleus, while the 4s orbital has a highly symmetric but a broader distribution (Pepperhoff & Ancet, 2001). The collective interaction of electronic moments give rise to the magnetic characteristics of magnetic materials, usually rendering them diamagnetic, paramagnetic, superparamagnetic, ferro/ferrimagnetic or antiferromagnetic. These classifications are discussed here in the context of solid nanomagnetic materials.

### 1.3.1 Diamagnetic, Paramagnetic, Superparamagnetic and Ferromagnetic Nanomaterials

The bulk magnetic response of a material to an external field is usually described as its magnetic susceptibility ( $\chi$ ).

$$M = \chi H \qquad \text{Eqn 11.}$$

Where M is the magnetization of the material, H is the external magnetic field, and  $\chi$  is the magnetic susceptibility.

Diamagnetic materials are often the result of no interaction between electronic moments because all electrons are paired. Thus, there is no residual spin or moment alignment with the application of an external magnetic field, and instead a slight repulsion. Diamagnetic materials are characterized by having a negative magnetic susceptibility.

Paramagnetic materials are defined by the nearly linear increase in material magnetization with an applied field, and thus by a positive magnetic susceptibility ( $\chi$ ). Typically, paramagnetism arises from atoms with magnetic moments that are uncoupled because the energy of interaction is much less than the thermal energy ( $k_B T$ ) of spin fluctuation. Since there is no collective movement of moments (long-range order), the moments act individually and result in relatively low overall magnetic moments.

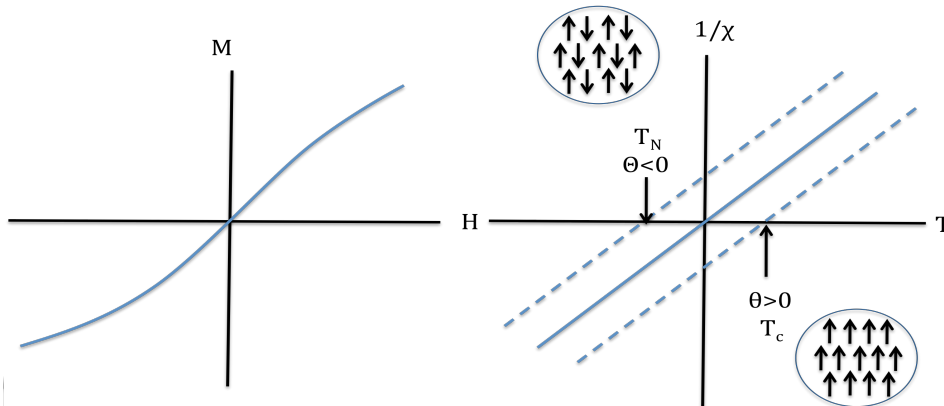


Figure 2. (Left figure) Paramagnetic magnetization as a function of applied magnetic field. Response is linear with no saturation magnetization visible. (Shaw, et al.). (Right figure) Susceptibility ( $1/\chi$ ) as a function of temperature. Temperature axis intercepts represent the Curie transition temperature for ferromagnetic materials ( $\theta > 0$ ) or the Néel transition temperature for antiferromagnetic materials ( $\theta < 0$ ).

There are various types of paramagnetism, Curie, Curie-Weiss, Pauli, and Van Vleck (McElfresh, 1994). These different types of paramagnetism are mainly characterized by their temperature dependence or lack thereof. The understanding of their respective temperature response provides with unique insight about the electronic interactions of individual moments within the magnetic solids.

In this work, I mainly concentrate on Curie and Curie-Weiss paramagnets. These paramagnets have the following magnetic susceptibility:

$$\chi = \frac{C}{(T - \theta)} \quad \text{Eqn. 12}$$

Where the temperature  $\theta$  is non-zero for Curie-Weiss paramagnets, and zero for Curie paramagnets. Figure 2 illustrates how the sign of this temperature  $\theta$  indicates the type of interaction between adjacent moments. For  $\theta < 0$  the individual moments are known to be antiferromagnetically-coupled (Figure 2 above). This interaction facilitates the opposite alignment between adjacent moments. For  $\theta > 0$  the individual moments are known to be ferromagnetically-coupled and thus adjacent moments are aligned in the same direction (Figure 2 above).

Curie-Weiss paramagnets have a linear  $1/\chi$  vs.  $T$  plot (Figure 2 above). The temperature  $\theta$  is represented in this plot as the temperature where the line intercepts the abscissa. For  $\theta > 0$  this temperature is known as the Curie temperature,  $T_c$ , and therefore has a ferromagnetic transition at that temperature. Conversely, for  $\theta < 0$  this temperature is known as the Néel temperature,  $T_N$ , these materials possess an antiferromagnetic transition near that temperature.

An example of Curie-Weiss paramagnets is amorphous spin-glass like materials in which there is some degree of long-range disorder.

Superparamagnetism has a stronger interaction between electronic moments and thus the susceptibility constant  $\chi$  is much larger than 0. However, the response to increasing applied field yields a non-linear magnetization of the sample. This magnetization curve results in saturation at lower magnetic fields than for paramagnetic materials as seen in Figure 3. Superparamagnetism is strongly size-dependent as the magnetic anisotropic energy barrier is proportional to the product of the magnetic anisotropic constant  $K_u$  and the volume of the particle (Jun, Seo, & Cheon, 2008). Therefore, materials that are in the nanometer scale (approximately  $<30\text{nm}$  diameter) have insufficient magnetic energy to overcome the intrinsic thermal energy that allows for spin fluctuations. Thus, in the absence of a magnetic field they result in a net magnetization of zero and no magnetic remanence as seen in Figure 3 below.

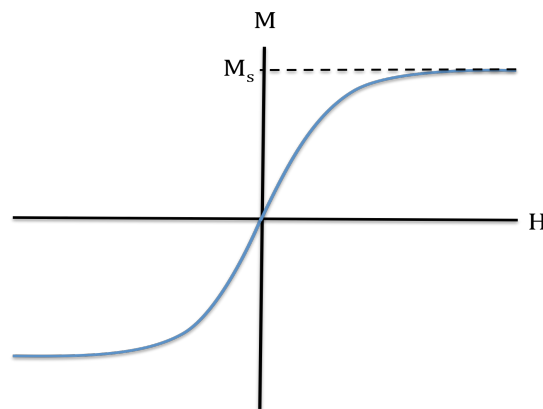


Figure 3. Magnetization as a function of external applied magnetic field.

Superparamagnetic materials possess full reversibility and saturation magnetization,  $M_s$ , as an intrinsic property of the materials.

The surface of nanomagnetic materials have more spin-glass like characteristics, where the individual spins lack coupling with one another due to surface defects and mainly due to structural disorder. As the size of the nanoparticle shrinks, then the volume ratio between the surface-disordered spins and the overall particle volume increases resulting in a reduced saturation magnetization and tipping the susceptibility closer to the paramagnetic regime as shown previously in ultra small nanoparticles (B. H. Kim, et al., 2011).

When atoms are coupled through shared electrons, such as in a crystal oxide, the magnetization also increases with the applied field. In certain nanoparticles, when the external magnetic field is removed, the magnetization remains fixed with finite remanence and coercivity ( $M_r$  and  $H_c$ ). These materials are known as “ferromagnetic.” The magnetization remains fixed in orientation in these materials because the thermal energy is not sufficient to overcome the coupling between spins in the material through the anisotropy energy.

Most nanoparticles are ferromagnetic due to the formation of magnetic domains within the crystals. But in some cases single-domain nanoparticles are still ferromagnetic because they possess an unusual magnetic anisotropic energy that result in a finite coercivity that is characterized by the following relationship (Jun, et al., 2008).

$$H_c = \frac{2k_u}{M_s} \left[ 1 - 5 \left( \frac{k_B T}{k_u V} \right)^{\frac{1}{2}} \right]$$

*Eqn. 13*

Where  $M_s$  is the saturation magnetization of the sample,  $k_u$  is the magnetic anisotropic constant,  $k_b$  is the Boltzmann constant,  $T$  is the temperature, and  $V$  is the particle volume.

Conceptually, domains represent a volume of homogeneous magnetization inside the crystal, although the domain can be dynamic and variable in size.

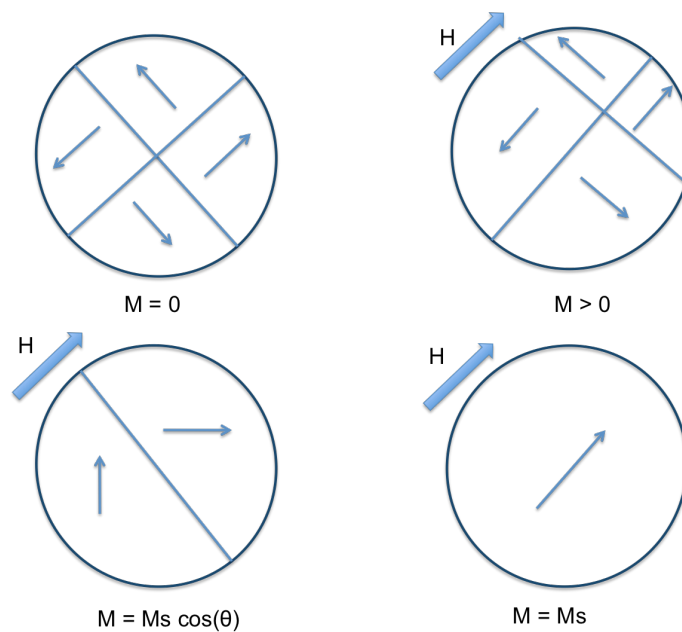


Figure 4. Schematic showing magnetic domains in a nanoparticle and their movement along their easy-axes in order to align with the external magnetic field.

Adapted from (McElfresh, 1994).

The above figure illustrates the formation of magnetic domains, not to be confused with crystallographic domains, and their movement in order to have all moments align with the applied external magnetic field. Coercivity mainly results in the inability for these domains to return to their original states unless an

additional reversal field is applied. When the field strength is reversed from magnetic saturation, domains return to their preferred crystallographic positions. Upon further field reversal, domain walls start to move towards their original states. However, due to the presence of grain boundaries, defects, and inclusions within the crystal, this movement is sometimes impeded. Thus, full return to the initial magnetic domain position is not accomplished resulting in residual magnetization (magnetic remanence  $M_r$ ) as illustrated in Figure 5.

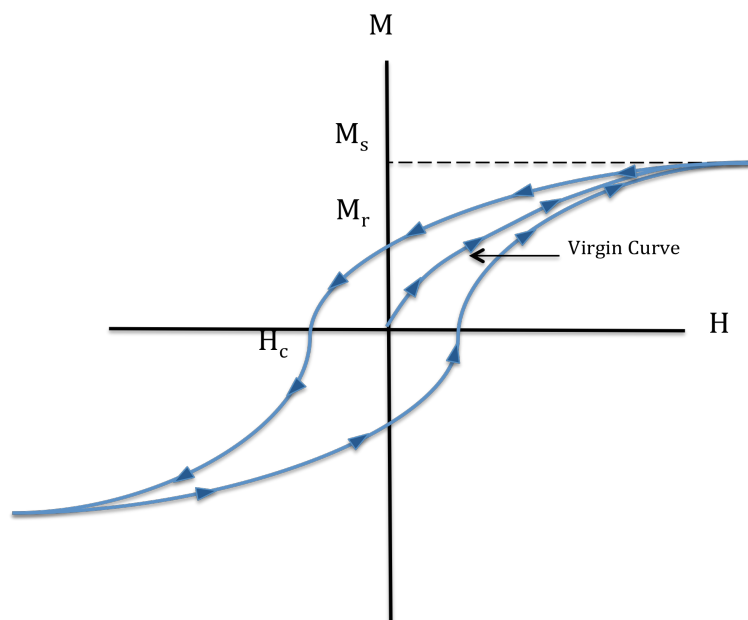


Figure 5. Magnetization reversal experiment on a ferromagnetic material. Magnetization curve shows the virgin curve initially formed when the material is first magnetized. Upon reversal from saturation,  $M_s$ , the sample shows irreversibility and displays a remanent magnetization,  $M_r$ , when the applied field is absent ( $H=0$ ). A negative field is needed to return the magnetization to zero ( $H_c$ ). Adapted from (McElfresh, 1994)

These principles and magnetism mechanisms of nanomagnetic materials are the basis for nanoparticle-based contrast agents. Although magnetic materials are widely understood and explained in a phenomenological manner it is crucial to obtain full understanding of the underlying spin mechanisms. Understanding the magnetization process at the level of individual and collective spins is of uttermost importance when designing magnetic materials in the nanometer scale as contrast agents for MRI.

#### 1.4 Contrast Agent Relaxivity

Recent advances in targeted molecular imaging have made it possible to image molecular events *in vivo* with MRI. Many of the probes used for molecular imaging involve the use of synthetic iron oxide nanoparticles for  $T_2$  and  $T_2^*$  - imaging, and chelates of paramagnetic ions for  $T_1$ -weighted imaging. Due to the inherent insensitivity of MRI to detect molecular probes, there is a need to develop techniques to synthesize higher relaxivity agents in order to use them as molecular probes for *in vivo* MRI. This sensitivity can be quantified by the agent's relaxivity (Querol & Bogdanov, 2006). Relaxivity is defined as the rate of relaxation of water protons in 1mmol/L solution of agent.

$$\frac{1}{T_x} = \frac{1}{T_{x,b}} + r_x \cdot C \quad x = 1, 2 \quad \text{Eqn. 14}$$

Per Equation 14, the term  $r_x$  determines the concentration that can be detected (Aime, Castelli, Crich, Gianolio, & Terreno, 2009; B. R. Haacke M, Thompson M, Venkatesan R, 1999b; Querol & Bogdanov, 2006) over background.

Tissue	T <sub>2</sub> —3 T [ms]		T <sub>1</sub> —3 T [ms]		T <sub>2</sub> —1.5 T [ms]		T <sub>1</sub> —1.5 T [ms]	
	This study	Literature	This study	Literature	This study	Literature	This study	Literature
Liver	42 ± 3		812 ± 64		46 ± 6	54 ± 8 <sup>(35)</sup>	576 ± 30	~600 <sup>(23)</sup>
Skeletal muscle	50 ± 4	32 ± 2 <sup>(25)</sup>	1412 ± 13	1420 ± 38 <sup>(25)</sup>	44 ± 6	35 ± 4 <sup>(25)</sup>	1008 ± 20	1060 ± 155 <sup>(25)</sup>
Heart	47 ± 11		1471 ± 31		40 ± 6	44 ± 6 <sup>(36)</sup>	1030 ± 34	
Kidney	56 ± 4		1194 ± 27		55 ± 3	61 ± 11 <sup>(37)</sup>	690 ± 30	709 ± 60 <sup>(37)</sup>
Cartilage 0°	27 ± 3	37 ± 4 <sup>(25)</sup>	1168 ± 18	~1240 <sup>(25)</sup>	30 ± 4	42 ± 7 <sup>(25)</sup>	1024 ± 70	~1060 <sup>(25)</sup>
Cartilage 55°	43 ± 2	45 ± 67 <sup>(26)</sup>	1156 ± 10		44 ± 5		1038 ± 67	
White matter	69 ± 3	56 ± 4 <sup>(27)</sup>	1084 ± 45	1110 ± 45 <sup>(29)</sup>	72 ± 4	79 ± 8 <sup>(38)</sup>	884 ± 50	778 ± 84 <sup>(38)</sup>
Gray matter	99 ± 7	71 ± 10 <sup>(27)</sup>	1820 ± 114	1470 ± 50 <sup>(29)</sup>	95 ± 8	~95 <sup>(39)</sup>	1124 ± 50	1086 ± 228 <sup>(38)</sup>
Optic nerve	78 ± 5		1083 ± 39		77 ± 9		815 ± 30	
Spinal cord	78 ± 2		993 ± 47		74 ± 6		745 ± 37	
Blood	275 ± 50		1932 ± 85	~1550 <sup>(30)</sup>	290 ± 30	327 ± 40 <sup>(14)</sup>	1441 ± 120	~1200 <sup>(30)</sup>

Figure 6. Intrinsic T<sub>2</sub> and T<sub>1</sub> relaxation times of different tissues *in vivo* at 3T and 1.5T. Reprinted with permission from (Stanisz, et al., 2005). Copyright John Wiley and Sons, 2005.

Intrinsic tissue background is an important parameter to consider when designing ultra-sensitive nanoparticle contrast agents for molecular MRI. Stanisz et al. introduced a comprehensive list of relaxation times for different tissues based on literature and experimental results (Figure 6). It is evident that for most tissues their intrinsic longitudinal relaxation rate is much longer than the transverse relaxation rate *in vivo* and at different field strengths. This offers an advantage for T<sub>1</sub>-weighted over T<sub>2</sub>-weighted imaging to detect lower concentrations *in vivo*. As shown in figure 7 below, it is clear that T<sub>1</sub>-shortening contrast agents do not require as high of a relaxivity in order to attain lower concentrations *in vivo*.

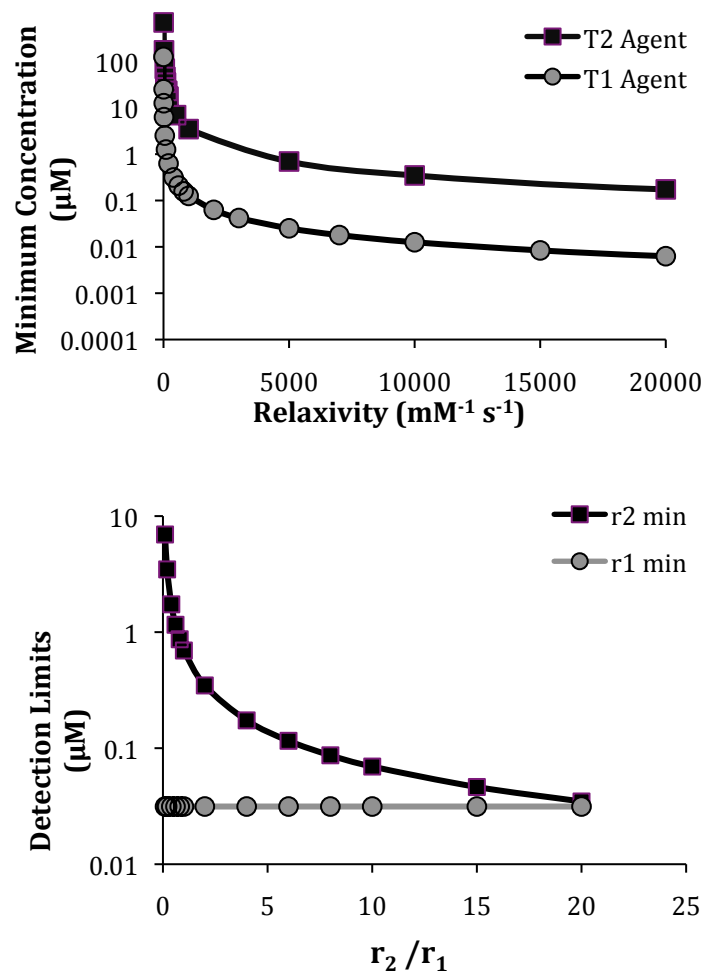


Figure 7. (Top plot) Simulated minimum concentrations that can be detected assuming an arbitrary minimum 10% change from signal to background for T<sub>1</sub>-shortening agents and 20% change for T<sub>2</sub>-shortening agents. (Bottom plot) Simulated detection window based on agents with increasing r<sub>2</sub>/r<sub>1</sub>.

Though an agent can have a high T<sub>1</sub> relaxivity (r<sub>1</sub>) its corresponding r<sub>2</sub> is important in order to assess its ability to be detected. As the r<sub>2</sub>/r<sub>1</sub> increases for any specific agent, the detection window narrows as the agent starts becoming more of a T<sub>2</sub>-shortening agent than a T<sub>1</sub>-shortening agent. This is illustrated in Figure 7 bottom panel, where it is evident that the concentration range at which

the agent can still be considered a  $T_1$ -shortening contrast agent decreases as its  $r_2$  effect increases and overrules the  $r_1$  effects in surrounding water. Therefore, for a wider concentration range of detection,  $T_1$ -shortening contrast agents are most desirable when its  $r_2/r_1$  is as low as possible. The ability to tune the  $r_2/r_1$  of a specific particle could provide with a pathway for more sensitive detection of molecular events *in vivo*. In order to tune each relaxivity individually, it is important to understand the interactions between the different magnetic materials and the surrounding water and their effects on the overall MRI signal. In order to attain this understanding, I discuss two well-known models for longitudinal and transverse relaxation effects on the water protons.

#### 1.4.1 Solomon Bloembergen Model of Dipolar Longitudinal Relaxation and Coordination Spheres

The Solomon-Bloembergen-Morgan (SBM) equations model the dipolar relaxation rate of water protons due to the effect that a paramagnetic moment has on the bulk water  $T_1$  relaxation. This model also describes the overall longitudinal relaxation rate to be the product of multiple contributions. These contributions are determined by the theory of coordination spheres (Caravan, Farrar, Frullano, & Uppal, 2009). More specifically, the observed relaxation rate ( $r_1^{\text{obs}}$ ) is the sum of the relaxation rates of water located within each of the coordination spheres.

This is:

$$r_1^{\text{obs}} = r_1^{\text{IS}} + r_1^{\text{SS}} + r_1^{\text{OS}} \quad \text{Eqn. 15}$$

Where,  $r_1^{IS}$  is the inner sphere relaxivity,  $r_1^{SS}$  is the second sphere relaxivity, and  $r_1^{OS}$  is the outer sphere relaxivity. The inner sphere (IS) is defined as water that is directly bound to the paramagnetic ion. The second sphere (SS) is defined as water that is bound weakly to ligands that are farther away from the paramagnetic ion, and therefore it is mostly a chemical exchange mechanism. And finally, the outer sphere (OS) is mostly the contribution from bulk water diffusion surrounding the agent at longer distances from the paramagnetic ion. For the purposes of this model its contribution is assumed to be constant ( $2\text{mM}^{-1}\text{s}^{-1}$ )(Caravan, et al., 2009).

$$r_1^y = \frac{q^y}{[H_2O]^y(T_1^y + \tau_M^y)} \quad , y = IS, SS \quad \text{Eqn.16}$$

$$\frac{1}{T_1} = \frac{2}{15} \left( \frac{\mu_0}{4\pi} \right)^2 \frac{\gamma_H^2 g_e^2 \mu_B^2 S(S+1)}{r_{MH}^6} \left[ \frac{3\tau_c}{1 + \omega_H^2 \tau_c^2} \right] \quad \text{Eqn.17}$$

$$\frac{1}{\tau_c} = \frac{1}{\tau_M} + \frac{1}{\tau_R} \quad \text{Eqn.18}$$

Where,  $q$  is the hydration number,  $\tau_M$  is the water residence time,  $T_1$  is the dipolar longitudinal relaxation rate,  $[H_2O]$  is the bulk water concentration,  $\mu_0$  is the permittivity of vacuum,  $\mu_B$  is the Bohr magneton,  $\gamma_H$  is the gyromagnetic ratio,  $r_{MH}$  is distance between the electron spin of the paramagnetic metal and the proton spin of the water molecule in the corresponding coordination sphere,  $\omega_H$  is the larmor frequency at 1.5T,  $\tau_c$  is the overall correlation time and  $\tau_R$  is the rotation correlation time, which can be calculated using Stoke's equation. Based on equation xx the dipolar relaxation rate is easily modulated by the distance

between the electronic moment of the paramagnetic atom and the water proton moment.

All these equations have been used to predict the longitudinal relaxation that a single paramagnetic nucleus ( $Gd^{3+}$  or  $Mn^{2+}$  macrocyclics and chelates) imposes on the surrounding water. Therefore, for nanoparticle based paramagnetic contrast agents the only moments contributing to an overall water longitudinal relaxation are those of the surface and in close contact with water protons.

#### 1.4.2 Chemical Exchange Model and Static Dephasing Regime for Transverse Relaxation

Similar to the longitudinal relaxation model that, relies on the dipolar interaction between the unpaired electron magnetic moment and the proton moment. The transverse relaxation model relies on the interaction of the magnetic moment and the dephasing of the surrounding water protons in the transverse plane.

In a medium with magnetized particles, as the particles become partially aligned with the external magnetic field, their induced magnetization creates a field gradient around the particle since the magnetic susceptibility constant is much greater than that of paramagnetic particles or atoms. Thus, there is a difference in local frequencies that water protons experience as they diffuse in and out of the local gradient field or bind and unbind to the particle surface that lead to an accumulation of different spin phases through the sample prior and during data acquisition (Yablonskiy & Haacke, 1994).

Transverse relaxation shortening due to magnetized particles is modulated mainly by the following parameters: 1) the particle size, 2) the measurement half echo time ( $\tau_{cp}$ ) and 3) the diffusion time ( $\tau_D$ ). As the size of the particle is not large enough to create large surrounding magnetic inhomogeneities, the chemical exchange model is an appropriate model for the transverse relaxation of the medium. Thus, a model for weakly magnetized particles where the maximum dephasing during an echo interval is less than one radian is considered. This is  $\tau_{CP} < 1/\Delta\omega$ .

Therefore, according to the chemical exchange model introduced by Gillis and coworkers and assuming a long echo limit, the transverse relaxation is described as the following (Brooks, Moiny, & Gillis, 2001).

$$\frac{1}{T_2} = \frac{4}{9} v \tau_D \Delta\omega_r^2 \left\{ 1 + \left( \frac{4}{9} \right)^2 \left( \frac{\tau_D}{\tau_{CP}} \right)^2 \left( \frac{\Delta\omega_r \tau_{CP}}{1.34} \right)^{\frac{5}{3}} \right\}^{-1} \quad \text{Eqn.19}$$

In the static dephasing regime, where particles are strongly magnetized, the mechanism for transverse relaxation is modulated mostly by the diffusion of the water molecules through the magnetic field created by the magnetized nanoparticle. Thus  $\tau_D$  is on the order of the time that it takes for a water molecule to diffuse a distance comparable with the field-creating object (Yablonskiy & Haacke, 1994). Since  $\tau_D$  increases proportionally with the size of the particle, the motional averaging effect is diminished setting a maximum for  $r_2$  for any material. Then  $R_2$  is described as follows.

$$\frac{1}{T_2} = \frac{\pi\sqrt{15}}{9} v \Delta\omega_r \quad \text{Eqn.20}$$

As outlined in Weissleder et al, the relaxivities can be modeled using these equations taking into account the particle size, magnetization and particle lattice parameters (Yoon, Lee, Shao, Hilderbrand, & Weissleder, 2011).

### 1.5 Engineering High Relaxivity Nanoparticle Contrast Agents

Since the efficiency of the agent can be quantified by its  $T_1$  relaxivity ( $r_1$ ) and  $T_2$  relaxivity ( $r_2$ ), I investigate the mechanisms to increase these relaxivities to be able to attain detection of agent at relevant biological concentrations. Current techniques to increase  $r_1$  in nanoparticles usually involve increasing the paramagnetic metal payload per nanoparticle. However, the sensitivity for detection with these methods is still in the nanomolar to micromolar range. Therefore, there is an increasing need to design nanoparticle based contrast agents of high efficiency such that they can be detected at concentrations that are relevant for molecular imaging.

#### 1.5.1 Chemical Doping

The ability to tune the magnetization of crystals by altering their composition has helped in the design of magnetic materials. Here, I concentrate mainly in oxide-based crystal structure manipulation.

The manipulation of oxides relies mostly on the concept of superexchange. In ionic solids superexchange operates by coupling localized 3d electron moments from transition metal cations. In an antiferromagnetic crystalline structure such as that of MnO for example, the transition metal magnetic moments align antiferromagnetically with respect to each other. This is, the spins in the transition metal cation located in the same (111) plane are

aligned parallel. But the nearest cation plane spins are aligned in the other direction. Regular Heisenberg exchange interaction must occur in an indirect manner since the cations are located too far apart to have wavefunction overlap. This exchange coupling is accomplished only via a mediator. In the case of the MnO lattice, the mediator is the Oxygen anion located in between planes. The oxygen anion  $p$  orbital exchanges an electron with the  $3d$  orbitals from the transition metal cation. The symmetry and the spin orientation (up or down) localization in the  $p$  anion versus the  $d$  cation allows for electron spin orientation conservation and thus for antiferromagnetic coupling of transition metal cation neighbors (O'Handley, 2000).

Since both cations possess the same  $3d$  electronic configuration the magnetic moments for each cation is the same and thus “cancel each other out”. Contributing with no net magnetization. Naturally, one could assume that if the electronic configuration of one of the  $3d$  cations were to be different, the magnetic moments would not “cancel out” and thus, result in an observed net magnetization in the crystal. This is where “doping” of crystals helps in increasing the net magnetization. One example of doping is the use of a mixed valence cation electron crystal such as magnetite. The formation of a lattice that is comprised of  $\text{Fe}^{3+}$  and  $\text{Fe}^{2+}$ , with  $3d^5$  and  $3d^6$  electronic configurations, respectively, leads to an un-even antiferromagnetic coupling. Although the lattice structure in iron oxides are much more complicated than the previous rock salt example, the superexchange phenomenon still holds.

Iron oxide crystal structures that possess a net magnetization are usually arranged in a spinel structure. This atomic configuration is very complex and the bonding is no longer linear (i.e. Transition metal-Oxygen-Transition metal).

Spinel structures have two preferential sites for cation dopant localization. These sites are known as tetrahedral (Silverthorn) and octahedral ( $O_h$ ) sites. In this structure these sites are antiferromagnetically coupled and experience superexchange facilitated by the oxygen anions in the lattice. Figure 8a shows the sublattice organization for a spinel lattice structure. Either one of the sites can be substituted with transition metal cations that can allow d-p orbital overlap. In Lee and coworkers, for instance, examples of ferrite doping included the substitution of  $Fe^{2+}$  or  $Fe^{3+}$  with  $Ni^{2+}$ ,  $Mn^{2+}$ ,  $Co^{2+}$  and  $Fe^{2+}$  in either  $O_h$  or  $T_h$  (Lee, et al., 2007). The change in oriented magnetic moments in the crystal by doping led to a net magnetization that was largest for  $Mn^{2+}$  doped and lowest in  $Ni^{2+}$  doped ferrites (Figure 8b). This effect corresponded to the maximum saturation magnetization and relaxivity coefficient for  $Mn^{2+}$  doped ferrites and the minimum for  $Ni^{2+}$  doped ferrites (Figure 8b and c).

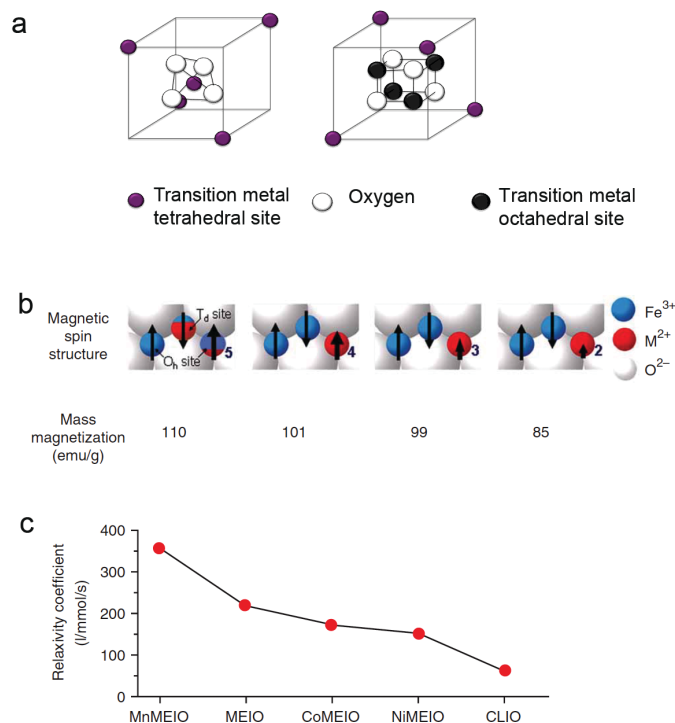


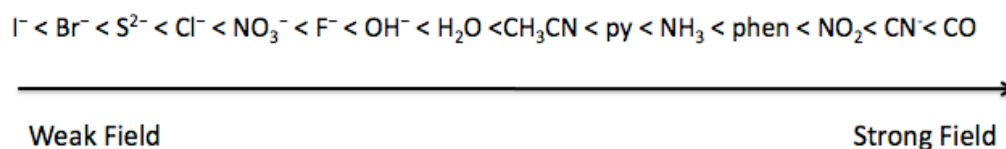
Figure 8. Ferrite spinel crystal structure illustrating possible octahedral (*Oh*) and tetrahedral (Silverthorn) dopant occupancy sites (a). Unit cell spin moments for magnetically engineered ferrites with  $Mn^{2+}$ ,  $Fe^{2+/3+}$ ,  $Co^{2+}$ , and  $Ni^{2+}$  doping (b) Respective mass magnetization values for Mn, Fe, Co, and Ni doped ferrites and their relaxivity coefficients (c). (b-c) Adapted and reprinted with permission from (Lee, et al., 2007) Copyright 2007 Nature Publishing Group.

### 1.6 Ligand and Crystal Field Manipulation of Spin State

Most inorganic nanoparticle based contrast agents are synthesized using 3d transition metal atoms either in the form of an oxide or an alloy. Coulomb interactions between the ligand and the metal atom electrons give rise to the crystal field configuration. The most common configuration is octahedral where 6 ligands come together and coordinate the metal atom, however, tetrahedral,

square planar, square pyramidal and other arrangements are also possible. The crystal field splitting arises from the arrangement and the location of the ligand bonding electrons with respect to the metal d-orbitals. Orbitals that are closer to the ligand will have a higher energy than orbitals farther away from the ligands.

Bonding between atoms in an oxide is facilitated by d-orbital overlap with surrounding atom orbitals of lower energy and appropriate symmetry, most of the cases p-orbitals. This bonding gives rise to the delocalization of electrons moving from the ligand to the coordinated metal. The classification of the ligand is determinant of the metal atom orbital energy splitting. The following is a list of common ligands and their classification based on their ligand field.



A strong field ligand coordinated to a 3d transition metal atom will split the degenerate state into  $t_{2g}$  and  $e_g$  states, where the pairing energy is lower than the electron orbital transition energy. For example,  $Fe^{2+}$  is a  $3d^6$  system with 6 electrons ready to occupy the 5 d-orbitals. When bound by a strong field ligand the energy splitting among the orbitals is increased making the electrons energetically more likely to pair first than to move toward higher energy orbitals. This changes the degenerate state to a low-spin configuration as illustrated in the figure below. Adopting a low spin configuration could then lead to a change in overall magnetic moment per atom. In this example, the coordination to a strong field ligand resulted in a change in the atom's magnetic properties. Mainly, a change from being paramagnetic to diamagnetic.

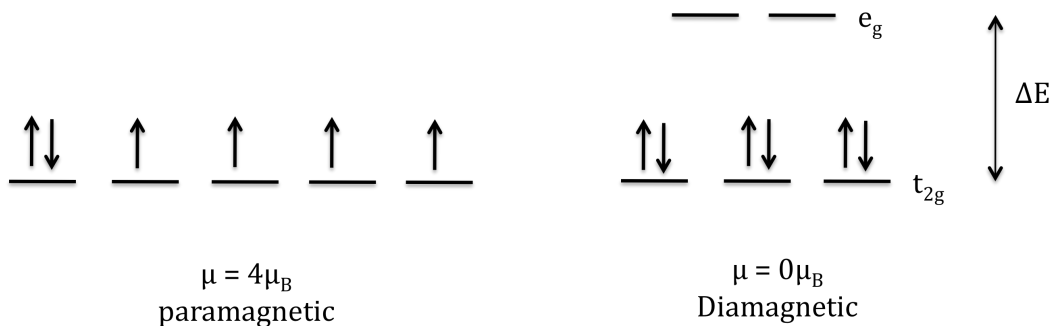


Figure 9. Spin configuration for  $\text{Fe}^{2+}$ . Left system shows the degenerate state for the  $3d^6$  system. Once coordinated to a strong field ligand, the spin configuration is that of a low spin system resulting in diamagnetism due to lack of unpaired electrons.

The rational selection of a ligand in the synthesis of a metal based magnetic material can provide the ability to induce a low spin or high spin configuration, which then can be used to manipulate the coupling and delocalization of magnetic moments within a crystal lattice and consequently the overall material magnetic properties.

### 1.7 Current Efforts on the Increase of Nanoparticle Based Contrast Agent Relaxivity

Macromolecules containing multiple paramagnetic ions are used to change the longitudinal relaxation rate,  $R_1$  (Accardo, et al., 2007), which typically brightens the MR image. Some common structures are liposomes, micelles, dendrimers, and peptides. The purpose of these structures is to increase the contrast agent metal payload in order to increase relaxivity. Paramagnetic macromolecular structures can be either biological or synthetic molecules. One example is the molecule developed by Karfeld et al (Karfeld, et al., 2007), with an engineered protein providing the backbone and repeating free lysines conjugated

to gadolinium chelates, achieving a per-agent  $r_1$  of  $62.6 \text{ mM}^{-1} \text{ s}^{-1}$ . Song et al. used small, synthetic, biocompatible molecules to increase the  $r_1$  of individual Gd(III) complexes by hindering the local rotation of the Gd(III) complex (Song, Kohlmeir, & Meade, 2008). Synthetic and biological molecules that include multiple gadolinium chelates are similar to nanoparticles in relaxivity, but have the advantage of structural flexibility; their backbone can be specifically designed for target delivery and membrane permeability, to carry other small molecules, or to bind to target tissue.

Recently, several porous nanostructures have been reported to greatly enhance paramagnetic relaxivity at clinical field strengths ( $\sim 1.5\text{T}$ ); their mechanisms are both intriguing and poorly understood. For instance, Sitharaman et al. developed “gadonanotubes” where  $\text{Gd}^{3+}$  ions were loaded onto the side-wall defects of single-walled carbon nanotubes (Sitharaman, et al., 2005). The reported per  $\text{Gd}^{3+}$  relaxivity was  $173 \text{ mM}^{-1}\text{s}^{-1}$ . Metal-doped carbon nanostructures are now being developed as a platform for increasing MRI relaxation (Choi, et al., 2007; Faraj, et al., 2009; Miyawaki, et al., 2006; Sitharaman & Wilson, 2006). Allen et al. bound  $\text{Gd}^{3+}$  to metal binding sites on the cowpea chlorotic mottle virus protein coat to obtain a per-ion  $r_1$  of  $202 \text{ mM}^{-1}\text{s}^{-1}$  (Allen, et al., 2005). A better understanding of the mechanisms of these types of agents may lead to new routes to develop high relaxivity  $T_1$  ( $1/R_1$ ) agents. Others have investigated how altering the metal content of a superparamagnetic nanoparticle can improve per-particle relaxivity; for example, Seo et al reported an iron-cobalt alloy crystal inside a graphite shell with a per-particle  $r_1$  of  $1.57 \times 10^6 \text{ mM}^{-1}\text{s}^{-1}$  and a  $r_2$  of  $6.47 \times 10^6 \text{ mM}^{-1}\text{s}^{-1}$  (W. Seo, et al., 2006).

## 1.8 Biological considerations for the Design of Nanoparticle Based Contrast

### Agents

The main biological considerations for nanoparticle based contrast agents are delivery, conjugation/functionalization, and toxicity and clearance after contrast agent administration.

The most important requirement is that the nanoparticles reach the intended target following systemic administration. Due to the active biochemical response of the host organism to the “foreign body” upon introduction, surface modifications are needed to the nanoparticles so as to prevent or reduce the “detection” and “elimination” by the body’s natural response system before the destination is reached. Surfactants and surface ligands used in the synthesis procedures not only control the growth of particles during synthesis but also act as a coating that can ensure stable dispersion of particles in solution and prevent aggregation. These coatings may also provide stealth properties to the particles and enable avoidance of body’s clearance mechanisms (Harris & Chess, 2003). However for *in vivo* use of these particles, further modifications of the surface coating may be necessary. The clearance route or accumulation of the particles in various organs depends on many factors such as size, shape and charge (M. Longmire, P. L. Choyke, & H. Kobayashi, 2008). Due to the leakiness of tumor vasculature and poor lymphatic clearance, “preferential” delivery and accumulation of nanoparticles as well as most small molecules is often observed in tumors through the enhanced permeability and retention effect (Maeda, Wu, Sawa, Matsumura, & Hori, 2000). Apart from such passive targeting, the targeted delivery and retention of nanoparticles into specific tissue of interest is of great interest for researchers developing diagnostic, theranostic, or therapeutic nano-

probes. Much research has focused on designing probes that “recognize” the vasculature or extravascular microenvironment of diseased tissue and display increased retention in such tissue over time while being cleared out of the normal tissue. Many biomolecules, such as small molecules, peptides, proteins, aptamers and antibodies have been identified that display specific affinities to the tissue microenvironment mediated by interactions with receptors on vascular endothelium or tissue cell surface. Following binding at the cell surface the particles can then be internalized and retained within the cells for a longer period. Such biomolecules have also been exploited for targeted delivery by attaching them to nanoparticles (Brannon-Peppas & Blanchette, 2004).

Conjugation of biomolecules to magnetic nanoparticles is a complicated multi-step process and has been reviewed recently (Sperling & Parak, 2010; Veiseh, Gunn, & Zhang, 2010). The choice of the core nanoparticle, ligand molecules that form the shell coating and targeting biomolecule are all critically dependent on the application. Typically conjugation techniques involve chemical or physical binding of the targeting moiety to the surface coating polymer. Chemical strategies involve covalent linkage strategies such as direct conjugation using the recently developed click chemistry approaches or use of linkers, while physical binding is based on electrostatic (E. Schellenberger, et al., 2008; Yiu, McBain, Lethbridge, Lees, & Dobson, 2010), hydrophilic/hydrophobic (Dilnawaz, Singh, Mohanty, & Sahoo, 2010; Jain, et al., 2008; Yu, et al., 2008) or affinity-based interactions (Artemov, Mori, Okollie, & Bhujwala, 2003; Gunn, et al., 2008). The specific conjugation strategy depends on the physicochemical properties the coating polymer and ligand to be linked and functional groups found on these. Detailed conjugation strategies are outlined in the literature

(Hermanson, 2008; Jolck, Feldborg, Andersen, Moghimi, & Andresen, 2011; Moghimi, Hunter, & Murray, 2001; Sperling & Parak, 2010; Veiseh, et al., 2010). The most important consideration is the continued ability to target the receptor despite chemical modifications. This necessitates binding of the ligand to the nanoparticle at a location away from the receptor recognition site. Direct covalent bonds can be formed between functional groups found on the nanoparticle shell and ligands to be conjugated. The choice of the polymer for the nanoparticle shell determines the type, number and location of these functional groups, which often also play a role in binding to the nanoparticle surface as well. Hence, polymers such as dextran, chitosan, or poly(ethyleneimine), bearing functional groups on the body, coat the nanoparticle with the backbone parallel to the surface, while polymers like poly(ethylene glycol) or phospholipids, with active groups at terminal ends, coat the nanoparticle with backbone parallel to the radius and form radial extensions similar to micelles or liposomes. Radial coatings can provide better steric access to the ligand for binding but the coupling to the nanoparticle may be less stable. Co-polymers (e.g. poly (acrylic acid)- poly(ethylene oxide)) can achieve both of the above effects; they can coat the nanoparticle surface uniformly and also provide binding sites for the ligand with less steric hindrance.

In direct reactions, functional groups such as amines, sulfhydryls, aldehydes, and thiols are directly bonded to reactive ligands, in some cases with the help of catalysts (Weissleder, Kelly, Sun, Shtatland, & Josephson, 2005). These strategies are particularly suitable for small molecule conjugation. Biomolecules may require modification prior to conjugation, thus increasing the likelihood of losing targeting ability unless modifications are minimal (E. A.

Schellenberger, Weissleder, & Josephson, 2004). Recently, a series of Cu-catalyzed azide–alkyne chemical reactions that are orthogonal to those of functional groups present within biological systems have enabled the selective tagging of biomolecules (Best, 2009; Hein, Liu, & Wang, 2008; Kolb, Finn, & Sharpless, 2001; Lutz & Zarafshani, 2008). These so called “click” reactions are highly specific, fast, efficient and require a relatively neutral pH aqueous environment (Best, 2009). A disadvantage is that these reactions require Cu as a catalyst and hence require its complete removal for in vivo use. Click chemistry has been used to attach cyclic LyP-1 targeting peptides to superparamagnetic iron oxide nanoparticles and used to target p32-expressing MDA-MB-435 cells in vitro and in vivo (von Maltzahn, et al., 2008). An alternate approach to covalent binding of ligands to magnetic nanoparticles involves the use of intermediate heterobifunctional linker molecules, which allows control over the orientation of bound ligands, thus potentially protecting targeting ligand functionality. Using the linker approach, magnetic nanoparticles have been conjugated to transferrin (Hogemann, Josephson, Weissleder, & Basilion, 2000), annexin V (E. A. Schellenberger, Sosnovik, Weissleder, & Josephson, 2004), folic acid (Kohler, Fryxell, & Zhang, 2004), chlorotoxin (Sun, et al., 2008; Veiseh, et al., 2005) siRNA (Medarova, Pham, Farrar, Petkova, & Moore, 2007), aptamers (Wang, et al., 2008) and HER2 antibody (Dilnawaz, et al., 2010).

The toxicity of a magnetic material depends on the material concentration, the organ or cell to which it is targeted, and the material chemical composition. Macromolecules such as dendrimer agents with conjugated paramagnetic ions are being developed with a wide range of specificity, biodistribution and enhanced magnetic properties (Bumb, Brechbiel, & Choyke;

Wiener, et al., 1994). Nanoparticle toxicity and clearance are active areas of investigation (M. Longmire, P.L. Choyke, & H. Kobayashi, 2008). The size and surface chemistry of a particle often determines whether the particle will reach and bind to a molecular target. In some instances, natural nanoparticles are desirable for both delivery and biocompatibility (Cormode, Jarzyna, Mulder, & Fayad, 2009). For example, cationized ferritin, a 13 nm protein-based iron oxide nanoparticle, is small enough to pass through the endothelial fenestrations on the kidney glomerular capillary wall (Bennett, Zhou, et al., 2008) and is able to bind to the anionic proteoglycans of the glomerular basement membrane (Beeman, Zhang, et al.). Furthermore, there are a number of particles designed to target over-expressed ligands in cancer cells as well as particles targeted to atherosclerotic plaques (Frias, Williams, Fisher, & Fayad, 2004; Nasongkla, et al., 2006). Some challenges to delivery in solid tumors include the increase in parenchymal pressure due to poor lymphatic drainage and increased extracellular matrix density. To overcome nonspecific retention, molecules have been developed with high target specificity, so that they are detected after low-dose intravenous injection. For example, Handl et al. and others have created multivalent peptides that bound with higher specificity to its ligand than the monovalent counterpart (Handl, et al., 2007; Li, Martin, & Gillies, 2007; Xu, et al., 2010; Xu, et al., 2009). Substantial physical barriers also prevent intravenously injected nanomaterials from reaching the target, and researchers have developed several emerging techniques that temporarily pass agents through these barriers using ultrasound, osmolar agents, or antibodies (Hynynen, 2008; Johansson, 1992; Kinoshita, 2006; C. H. Liu, D'arceuil, & De Crespigny, 2004; H. L. Liu, et al., 2010; Madsen & Hirschberg, 2010), or through intrathecal injection

(C. H. Liu, et al., 2004) or convection enhanced delivery (Bobo, et al., 1994; Lonser RR, 2002).

## CHAPTER 2

### FERRITIN AS A NATURAL CONTRAST AGENT

#### 2.1 Introduction

There are several commercially available and synthesizable nanoparticle contrast agents. Most of them are about 50 nm in size or larger, though some have recently been created in the 10 nm range (Ocean Nanotech, Springdale AR). Natural nanoparticles, such as ferritin, may have some advantages over synthetic nanoparticles for *in vivo* use as discussed in previous articles (Cormode, et al., 2009). Ferritin is a 13 nm protein nanoparticle with an iron oxide core. Ferritin has been used as a targeted contrast agent, and is small enough to be delivered through fenestrated endothelia (Bennett, Zhou, et al., 2008). Because native ferritin is only partially filled with a weakly superparamagnetic iron core, it has been reconstituted to fully fill the protein core with highly magnetic iron oxide cores to increase its MRI transverse relaxivity (Bulte, Douglas, Mann, Frankel, Moskowitz, Brooks, Baumgarner, Vymazal, Strub, et al., 1994). The efficacy and kinetics of ferritin as an *in vivo* agent were first reported to provide negative contrast to the liver, spleen and lymph nodes when injected systemically (Bulte, et al., 1995).

The  $T_2$  relaxivity of native ferritin is  $1\text{-}10\text{mM}^{-1}\text{s}^{-1}$  (Bennett, Shapiro, Sotak, & Koretsky, 2008). About tens of  $\mu\text{M}$  of native ferritin would be required to detect a 20% difference in shortened signal in grey matter tissue (assuming an intrinsic  $T_2$  of 100ms (B. R. Haacke M, Thompson M, Venkatesan R, 1999a)). Reconstituted "magnetoferritin" has been reported using chemically (Meldrum, Heywood, & Mann, 1992) or genetically modified ferritin (Uchida, et al., 2008).

Previous preparations of magnetoferritin have yielded a moderate  $r_2/r_1$  ratio, and required relatively complicated synthesis techniques. In this chapter, I present a simple chemical procedure to create a superparamagnetic magnetoferritin using commercially available apoferritin, with about a 25-fold increase in per iron relaxivity over native ferritin and an  $r_2/r_1$  of 1114. The magnetoferritin particles consistently stuck in a magnetic column, allowing them to be easily isolated and filtered. The resulting nanoparticles were made monodisperse and readily transferred between buffers to be functionalized. This work should make it possible to quickly and simply create uniform, functional nanoparticles for molecular MRI inside an endogenous protein.

## 2.2 Materials and Methods

### 2.2.1 Materials

Apoferritin from horse spleen (Sigma Aldrich), Iron (II) Chloride (Sigma Aldrich, 98%), 2 - N - Morpholino Ethane Sulfonic Acid (Alfa Aesar, 98%), and Bovine Serum Albumin (Pierce Biotechnology) were used as received. Anti-horse spleen ferritin antibody (Sigma Aldrich) was diluted 100 times prior use for immunoprecipitation experiments.

### 2.2.2 Simplified Synthesis of Magnetoferritin

The technique presented here is derived from various synthesis schemes (Kasyutich O, 2008; Meldrum, et al., 1992; Webb, Frame, Zhao, Lee, & Watt, 1994; Wong K.K.W, 1998) but uses horse spleen apoferritin and magnetic filtration to make monodisperse magnetoferritin. I suspended 2 $\mu$ M apoferritin (Sigma Aldrich, St Louis) or bovine serum albumin (BSA) (Pierce Biotechnology,

Rockford) in 0.05M MES buffer, pH 8.5. I prepared 48mM Fe (II) Chloride (Sigma Aldrich, St. Louis) in a separate flask. Both solutions were de-gassed with N<sub>2</sub> gas (50psi). The apoferritin or BSA solution were kept in a water bath at a constant temperature of 55-60°C, the pressure of the N<sub>2</sub> gas was reduced until no bubbles were formed. Every ten minutes, I then added 125µl of Fe(Miyawaki, et al.)Chloride to the de-gassing apoferritin or BSA solution and mixed with a pipette. The solution was covered with a rubber bung and sealed with paraffin film. This procedure was repeated a total of 20 times until the solution turned a slightly gray-turquoise color. The sample was removed and dialyzed overnight against 0.15M NaCl using a 10,000 MW cut off Dialysis Cassette (Pierce Biotechnology, Rockford, IL) and filtered magnetically with a micro magnetic column (Miltenyi Biotec, Gladbach, Germany), into 150 mM NaCl buffer (pH=7.4).

### 2.2.3 Protein and Metal Concentration Assays

The resulting protein concentration was obtained using the Better Bradford Assay (Thermo Scientific, Rockford). Briefly, known serial dilutions of Bovine Serum Albumin (BSA) were stained with Coomassie Plus Reagent. The reagent binds with certain aminoacids, which in turn result in a spectral shift (from brown to blue). This shift can be measured using a spectrophotometer or a plate reader measuring absorbance at around 595nm. For the experiments presented in this work, a wavelength of 570nm was used. The Bovine Serum Albumin concentrations and absorbances are used as a standard curve and the unknown sample concentrations are obtained interpolating their absorbance to those of the BSA standard curve.

Metal concentrations were obtained by means of Inductively Coupled Plasma-Optical Emission Spectroscopy. Briefly, the unknown samples were suspended in a solution containing 2% Nitric Acid. The acidic sample solution was then sprayed into the plasma flame from the ICP-OES where the molecules of interest collide with the electrons from the plasma flame and produce radiation at specific wavelengths. This radiation is categorized by wavelength and intensity to determine the concentration of each element of interest. Similarly to the protein colorimetric assay, a standard curve is used as a reference to determine the overall sample metal concentrations.

#### 2.2.4 Electron Microscopy

Samples were adsorbed on 400 mesh formvar coated carbon-copper grids (Pacific GridTech, San Francisco, CA). 50 $\mu$ l of magnetically filtered particles were placed on paraffin film and a grid was placed on top of the drop (formvar film side on sample). The sample was adsorbed for 5 minutes and excess water and sample were removed by slightly touching the edge of the grid with filter paper. Transmission electron microscopy (Artemov, et al.) images were obtained using a Philips CM12S Scanning Transmission Electron Microscope with EDAX 9800 plus energy dispersive x-ray spectrometer fitted with a Gatan model 791 CCD camera for direct digital image acquisition (Electron Microscopy Facilities, Arizona State University). The microscope was loaded with a tungsten film and used with an accelerating voltage of 80keV. High resolution transmission electron microscopy (HRTEM) images were obtained using a Philips FEI CM-200 Transmission Electron Microscope fitted with a Gatan Orisis CCD camera for

image acquisition. The microscope was loaded with a field emission gun (FEG) and used with an accelerating voltage of 200kV.

The average particle size was calculated by measuring the diameter of the particles using the Image J software (National Institutes of Health, Bethesda, MD). Each image was divided into four quadrants and 30 particles were measured at random from each quadrant, yielding a total of 120 particles per image. Three images were analyzed per sample.

### 2.2.5 Relaxometry at 1.5T

Relaxivity measurements were made with a 1.5T Minispec relaxometer (Bruker Optics, The Woodlands, TX.) The magnetoferritin solution was diluted and vortexed to make a 1% low melt agarose gel suspension. To find the corresponding  $T_2$  values, a Carr-Purcell-Meiboom-Gill (CPMG) sequence with inter pulse spacing ( $\tau$ ) of 20ms, gain of 70, and 200 points was used.

Alternatively, a spin echo sequence (W. S. Seo, et al.) was performed with TE=9, 13, 20, 31, 46, 70, 106 and 160 ms and TR=12s. In order to measure longitudinal relaxivity, I used an inversion recovery (IR) sequence with TI=400ms, TR=12s, and 16 averages. All samples were maintained at 37°C by the temperature controlled probe. The Bruker's Minispec software and the exponential curve-fitting feature were used to measure the relaxation times of each gel suspension.

### 2.2.6 Protein Integrity Studies via Gel Electrophoresis, and Immunoprecipitation

In order to confirm that filtered magnetoferritin was still immunologically equivalent to native ferritin, I performed immunoprecipitation of native ferritin, filtered magnetoferritin, unfiltered magnetoferritin, and apoferritin. The samples

were diluted to 30nM and labeled with anti-horse spleen ferritin antibody (Sigma Aldrich, St Louis). The antibody-ferritin complex was incubated with protein A Microbeads (Miltenyi Biotec, Gladbach, Germany) Samples were filtered using a magnetic column (Miltenyi Biotec, Gladbach, Germany) and rinsed with buffer. Samples were eluted with preheated (95°C) Novex Tris-Glycine SDS Sample Buffer (Invitrogen, Carlsbad CA) and incubated at room temperature for 5 minutes. The running solution was collected while the column remained in the magnetic field.

Samples were stained with Bromphenol Blue (Sigma Aldrich, St Louis) before loading into a 4-20% Novex Tris-glycine gel (Invitrogen, Carlsbad CA). As a standard I used Novex Sharp Pre-stained Protein Standards ladder (Invitrogen, Carlsbad CA) 10 $\mu$ l of stained sample was loaded into the gel wells and the gel was run for 100 minutes using 125 V of constant voltage, 30-40mA(start) and 8-12mA (end). The gels were then washed and stained with Simply Blue (Invitrogen, Carlsbad CA) for 1 hour.

Native Electrophoresis was also performed, and the samples were buffered in Novex Native Tris-Glycine Sample Buffer (Invitrogen, Carlsbad CA), 10 $\mu$ l of either native ferritin, magnetoferritin, or apoferritin samples were loaded into wells of a 4-20% Novex Tris-glycine gel. The gel ran for 4 hours using a constant voltage of 125V, 6-12mA/ gel (start) and 3-6mA/gel (end). The gels were then washed and stained with Simply Blue (Invitrogen, Carlsbad CA) for 1 hour.

### 2.2.7 *In vivo* Detection of Magnetoferritin Particles

All animal experiments were approved by an institutional animal care and use committee. *In vivo* injections were performed in three adult Sprague Dawley rats anesthetized with a Ketamine/Xylazine cocktail (90 mg/kg ketamine and 5 mg/kg xylazine). The coordinates of injection were identified as the caudate/putamen and were 1.6mm anterior, 3mm lateral from the bregma and 5mm interior from the dura. These coordinates were measured using a MRI compatible stereotaxic frame (David Kopf Instruments, Tujunga CA) and burr holes were made in the skull using a pneumatic drill. A 10 $\mu$ l Hamilton syringe was mounted onto the microinjector unit of the frame and the needle was first inserted 6mm interior from the dura where a pocket was formed by waiting 1 minute at that location and retracting to 5mm interior from the dura. Once located in the correct coordinates 10 $\mu$ l of 30nM native ferritin and 30nM magnetoferritin were injected over the course of 5 minutes on each hemisphere of the brain respectively. The animal was removed from the frame after injection and placed inside a 7 Tesla Bruker Pharmascan scanner with a three-axis gradient slew rate of 150 T/m/s. The animal was supplied with constant isofluorane gas during the scanning experiments; Rectal temperature was monitored and regulated by a feedback-controlled water bath. Scans were performed using a surface RF coil, gradient echo pulse sequence (TE/TR = 3.8/350ms, NEX = 4, matrix 256x192).

## 2.3 Results and Discussion

### 2.3.1 Synthesis and Particle Characterization

Partially- filled apoferritin nanoparticles, prepared using previously published protocols, are shown in TEM images in Figure 10a. Fully filled

magnetoferritin, prepared using the protocol outlined here, is shown in Figure 10d. The particles had core diameters ranging from 4nm to 6nm and HRTEM of a magnetoferritin particle is shown indicating crystal formation in the core of the protein. Bulk native ferritin contains some aggregated and partially filled cores (Figure 10b) and magnetically filtered native ferritin resulted in fully filled, aggregated sample with a low protein yield (Figure 10c). On average, magnetoferritin nanoparticles had larger magnetic cores (4nm-6nm) than native ferritin (2nm). This can be seen in Figure 10g, where 40% of the magnetoferritin particles ranged from 4-6nm and 50% of the native ferritin particles ranged from 1.5-2nm.

The yield of available protein after filtration depended on the volume of buffer that the particles are suspended in after filtration. When re-suspending 200 $\mu$ l of the magnetically selected particles in the 200 $\mu$ l of 0.15M NaCl, the yield was 4%. As a negative control, the synthesis was performed using 48mM of bovine serum albumin (BSA) (Pierce Biotechnology, Rockford, IL) instead of apoferritin.

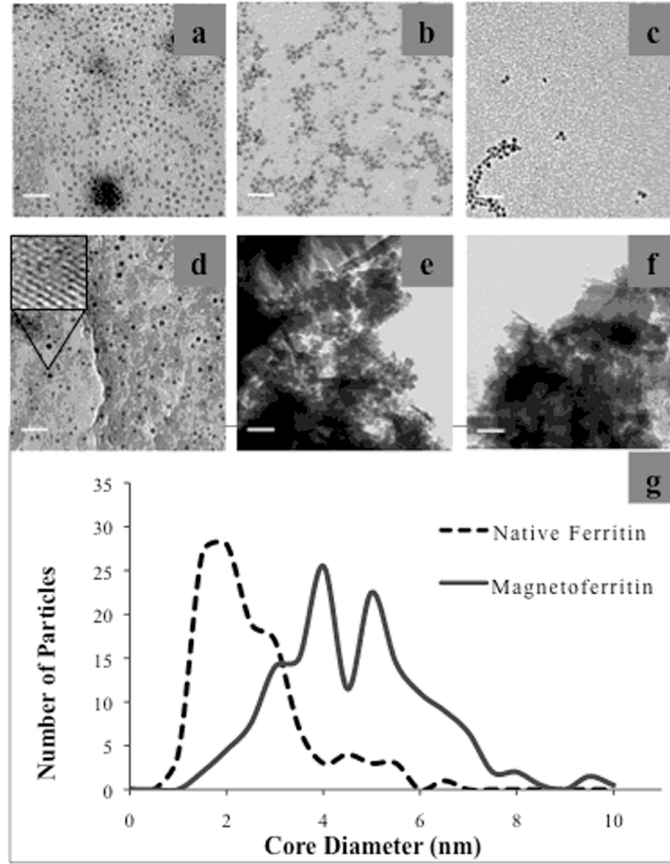


Figure 10. TEM images of a) Magnetoferritin unfiltered following published protocols b) Native Ferritin c) magnetically filtered native ferritin d) Magnetically filtered magnetoferritin and HRTEM of a magnetoferritin particle e) Unfiltered iron loaded bovine serum albumin f) Magnetically filtered iron loaded bovine serum albumin. Scale bars are 50nm at 88kX magnification. g) Size distribution of magnetoferritin particles (solid line) and native ferritin particles (dashed line).

Figure 10e and f show that BSA formed amorphous and aggregated crystals with no distinct shape or pattern before filtration or after filtration. After magnetic filtration, the TEM grid did not show electron dense areas except for the area shown in figure 10f. Therefore, it is likely that the iron oxidized and

adsorbed to the BSA surface aggregating and not forming a monodisperse or homogeneous particle solution.

Here, it is demonstrated a simplified method for synthesizing an iron oxide based contrast agent for visualization with MRI. Iron oxide particles have been extensively studied, and new particles are currently synthesized to visualize molecular events *in vivo* and drug delivery agents. However, small particles (tens of nanometers) are difficult to develop. Ferritin can be used as a reaction chamber to obtain homogeneous spherical particles. Ferritin loaded with iron oxide allows for an easy surface conjugation to antibodies, targeting peptides, or fluorescent markers. In comparison to other iron oxide agents currently available, the proposed magnetoferritin particle is simple to create. To incorporate Fe(III) into the core, ferritin uses O<sub>2</sub> as an oxidant and a catalytic site located in the center of the protein (Arosio, Ingrassia, & Cavadini, 2009). Two routes of iron loading have been identified, a catalytic pathway (due to the ferroxidase on H-ferritin) and an auto oxidative route that becomes important once the metal core has started to form (Levi, et al., 1988; Yang & Chasteen, 1999). This synthesis likely minimizes the auto-oxidation by displacing the oxygen with N<sub>2</sub> gas and, maximizes the catalytic iron deposition. This is supported by the fact that particles were not formed when BSA was used with same synthesis procedure.

### 2.3.2 Protein Integrity and Relaxivity

Native gel electrophoresis showed that native ferritin, magnetoferritin synthesized with the protocol outlined here, and apoferritin, all ran at the same molecular weight (Figure 11a). The immunoprecipitated samples of native ferritin,

magnetically filtered magnetoferritin, un-filtered magnetoferritin and apoferritin all showed bands at 200kDa. (Figure 11b)

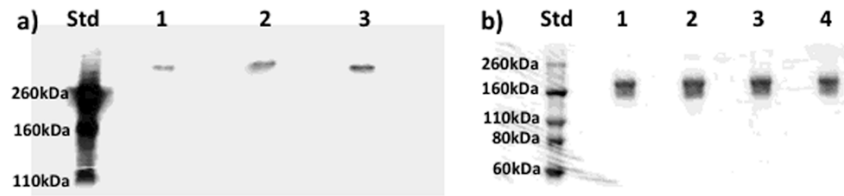


Figure 11. a) Native Gel of (Lane 1)Native Ferritin (Lane 2) Magnetoferritin (Lane 3) Apoferritin gel ran for 4.5h. b) SDS Gel of immunoprecipitated and denatured (Lane 1) Native Ferritin (Lane 2) Filtered Magnetoferritin (Lane 3) Unfiltered Magnetoferritin (Lane 4) Apoferritin. Gel was run for 100 min.

Magnetically filtered magnetoferritin had a 216-fold increase in protein relaxivity over native ferritin, and a 25-fold increase in iron relaxivity. In order to compare current relaxivity values of iron oxide particles already in use as contrast agents, I measured the relaxivity of magnetoferritin and native ferritin using a spin echo sequence. The increase is 31-fold and 275-fold of iron and protein relaxivity, respectively, when compared to native ferritin. Figure 12 shows the linear fit of the CPMG data for magnetoferritin and native ferritin both based on iron and protein concentrations. Table 1 provides a summary of  $T_1$  and  $T_2$  relaxivities using a CPMG, SE and IR pulse sequences of magnetoferritin, native ferritin and commercially available iron oxides.

Table 1.  
Magnetoferritin Relaxivity Summary

	Transverse Relaxivity			
	CPMG		Spin Echo	
	Iron (mM <sup>-1</sup> s <sup>-1</sup> )	Particle (mM <sup>-1</sup> s <sup>-1</sup> )	Iron (mM <sup>-1</sup> s <sup>-1</sup> )	Particle (mM <sup>-1</sup> s <sup>-1</sup> )
<b>Native Ferritin</b>	3	1868	4	2455
<b>Magnetoferritin</b>	78	404045	130	675476
<b>10nm PDDA Iron Oxide</b>	260.63	N/A*	268.2	N/A*

	Longitudinal Relaxivity	
	Inversion Recovery	
	Iron (mM <sup>-1</sup> s <sup>-1</sup> )	Particle (mM <sup>-1</sup> s <sup>-1</sup> )
<b>Magnetoferritin</b>	0.07	407
<b>10nm PDDA Iron Oxide</b>	5.099	n/a
<b>10nm PDDA Iron Oxide R2/R1</b>	51.11	n/a
<b>Magnetoferritin r<sub>2</sub>/r<sub>1</sub></b>	1114	993

*Note.* Native ferritin, magnetoferritin and 10nm PDDA Iron Oxide particles relaxivities based on iron and particle concentrations for two types of pulse sequences. Carr-Purcell-Meiboom-Gill (CPMG) and Spin Echo (SE) sequence. The ratio is the increase in relaxivity for magnetoferritin compared to native (i.e. Magnetoferritin relaxivity/Native ferritin relaxivity.) Longitudinal relaxivity of magnetoferritin based on iron and protein concentrations using an inversion recovery (IR) pulse sequence.

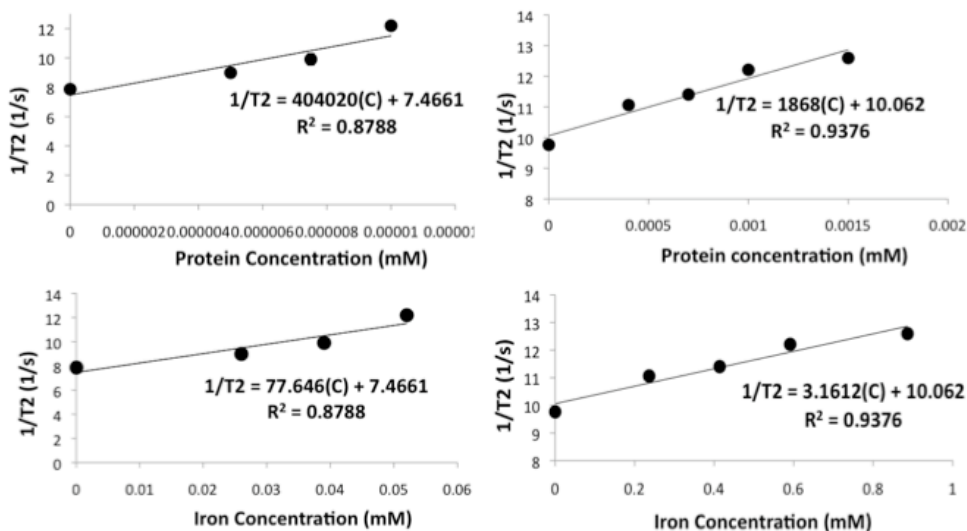


Figure 12. Linear fit for magnetoferritin and native ferritin in 1% agarose gels.

The transverse relaxation time ( $T_2$ ) was acquired using a CPMG pulse sequence in a Bruker 1.5T relaxometer with  $T_2$  exponential curve fit. 4 scans,  $\tau = 20\text{ms}$ ,  $TR = 15\text{s}$ , 200 points, at  $37^\circ\text{C}$ .

Magnetic filtration is a crucial step in creating magnetoferritin nanoparticles with a high per-iron transverse relaxivity of  $78\text{mM}^{-1}\text{s}^{-1}$  with a CPMG sequence, and a  $130\text{mM}^{-1}\text{s}^{-1}$  using a Hahn spin echo pulse sequence. The per-particle transverse relaxivity of  $404,045\text{mM}^{-1}\text{s}^{-1}$  with a CPMG sequence and  $675,476\text{mM}^{-1}\text{s}^{-1}$  with the spin echo sequence make it possible to detect nanomolar concentrations of ferritin nanoparticles. Also, immunoprecipitation and SDS electrophoresis indicate that the protein remains intact, and has the same molecular weight as filtered, unfiltered, native ferritin or apoferritin. Even though it would be expected that denatured protein would disassemble into its subunits and have bands between the 15-25KDa range, it has been shown that unboiled,

immunoprecipitated native ferritin has prominent bands around 200KDa (Passaniti & Roth, 1989), which is consistent with the results. A native gel was also run, and native ferritin, magnetoferritin and apoferritin all ran at the same molecular weight.

### 2.3.3 MRI of Magnetoferritin *in vivo*

The detection of low concentrations of agents is crucial for *in vivo* imaging. To study the detection of the synthesized magnetoferritin, I injected 30nM native ferritin or magnetoferritin into the caudate nucleus in adult rats. Figure 13 shows the scan of the 10 $\mu$ l injection of agent on each side. The image ipsilateral to the magnetoferritin was hypointense, indicating a strong susceptibility effect and T<sub>2</sub> weighting. In contrast, native ferritin was undetectable at 30nM concentration and at 7 Tesla.

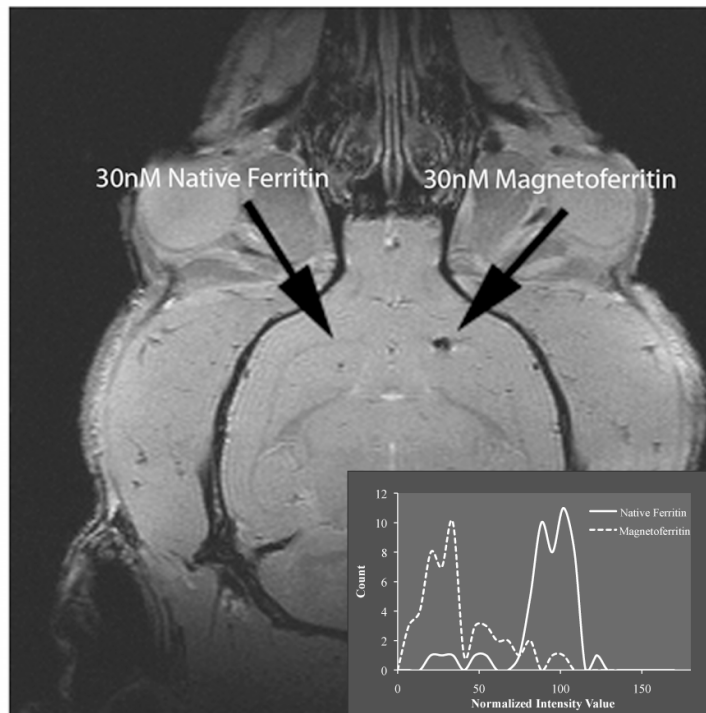


Figure 13. (a) Coronal gradient echo image of 30nM native ferritin (left) and Magnetoferritin (Shaw, et al.) infused into rat's Caudate/Putamen using a syringe microinjector device. (TE/TR = 3.8/350ms). Inset shows the distribution of pixel intensities at the site of injection for Native Ferritin and for Magnetoferritin normalized to surrounding tissue. (n=3 rats).

## 2.4 Conclusions

A simple method of synthesizing iron oxide particles with commercially available apoferritin as the platform is introduced here. The magnetoferritin synthesis includes a magnetic filtration step that separates the protein cages that are highly filled and ferromagnetic using a permanent magnet. After exhaustive dialysis and magnetic separation, the particles show to be monodisperse and uniform in size with their core sizes ranging from 4 to 6nm. Relaxometry indicates

that these particles exhibit a high per-iron transverse relaxivity of  $130\text{mM}^{-1}\text{s}^{-1}$  and per-particle relaxivity of  $404,045\text{mM}^{-1}\text{s}^{-1}$ . The fact that the protein remains immunologically equivalent to native ferritin and apoferritin after synthesis suggests that this synthesis scheme does not alter the protein antibody recognition sites for further detection or microscopy imaging. These results not only provide a facile technique for the incorporation of metallic elements inside the apoferritin core, but also facilitate the ability to magnetically engineer the crystal composition inside this versatile apoprotein platform.

## CHAPTER 3

### FEASIBILITY STUDY OF APOFERRITIN AS A NANO-REACTOR TO TUNE $r_2$ AND $r_1$

#### 3.1 Introduction

The ability to tune relaxivity in a natural nanoparticle contrast agent may provide unique advantages for magnetic resonance imaging. These advantages include the ability to tailor the desired relaxivity in a uniform and consistent platform such as apoferritin and increasing the detection window based on particle  $r_2/r_1$ . Here I explore several mechanisms in which  $r_2$  and  $r_1$  can be manipulated within the apoferritin protein. With the knowledge obtained previously on the metal deposition inside ferritin, it is possible to manipulate the structure and composition of the nanoparticle metal cores, and as a result tune the magnetic properties.

#### 3.2 Materials and Methods

##### 3.2.1 Materials

Apoferritin from horse spleen (Sigma Aldrich), Iron (Miyawaki, et al.) Chloride (Sigma Aldrich, 98%), 2 - N - Morpholino Ethane Sulfonic Acid (Alfa Aesar, 98%), Manganese (Miyawaki, et al.) Chloride (Sigma Aldrich, 1M solution), Sodium Tungstate Dihydrate (Sigma Aldrich), and Bovine Serum Albumin (Pierce Biotechnology) were used as received.

##### 3.2.2 Synthesis of $Mn^{2+}$ Adsorbed to Magnetoferritin

To synthesize magnetoferritin with manganese ions adsorbed to surface hydrophilic channels, 2 $\mu$ M Apoferritin (Sigma Aldrich, St. Louis, MO) buffered in 0.05M MES at pH 8.5, 48mM  $FeCl_2$  (Sigma Aldrich) and 4.8mM  $MnCl_2$  (Sigma

Aldrich) were de-aerated for 20 minutes with  $N_2$ . The solution was kept in a water bath at 55 to 60°C. I added 125µl of and 125µl of  $FeCl_2$  in sequence to the apoferritin solution. I made a total of 12  $MnCl_2$  and 8  $FeCl_2$  additions, ensuring that manganese was added first in the sequence. Samples were dialyzed against 0.15M NaCl, and filtered using a magnetic column (Miltenyi Biotec, Galdbach, Germany), eluted into 0.15 NaCl buffer. As a control, 2µM bovine serum albumin (Thermo Scientific, Rockford, IL) was used instead of apoferritin. The sample was removed and dialyzed overnight against 0.15M NaCl using a 8,000 MW cut off dialysis tubing (BioDesignDialysis Tubing, Carmel, NY)

### 3.2.3 Synthesis of Tungsten-Iron (WFe) Nanoparticles

To synthesize a tungsten and iron oxide filled apoferritin, tungstate was added at different rates. 2µM apoferritin (Sigma Aldrich, St. Louis, MO) was buffered in 0.05M Morpholino Ethanesulfoxide (MES) at pH 8.5. In separate containers I used 48mM  $FeCl_2$  (Sigma Aldrich), and 48mM  $Na_2WO_6$  (Sigma Aldrich). All solutions were de-aerated for at least 15 minutes with  $N_2$ , then kept in a water bath at 55 to 60°C under vacuum. Any apoferritin solution that evaporated during the de-aerating process was compensated by adding a previously de-aerated 0.05M MES buffer to maintain a constant volume throughout the reaction. I added the de-aerated 48mM  $FeCl_2$  at a rate of 12.5µl/min, 45µl/min, and 85µl/min to the apoferritin solution using a syringe pump for a total of 140 minutes. Fifty minutes into  $FeCl_2$  delivery, the de-aerated 48mM  $Na_2WO_6$  was added at a rate of 12.5µl/min using a syringe pump for a total of 40 minutes. A total of 1.75ml of  $FeCl_2$  and 500µl of  $Na_2WO_6$  were added to the protein solution. 200µl of 300mM sodium citrate was added to the solution

to chelate any remaining metal ions. The solution was then sonicated for 10 minutes and spun for 10 minutes at  $957 \cdot g$ . Finally, the supernatant solution was collected and dialyzed overnight against 3L of de-ionized water using a 8,000 MW cut off dialysis tubing (BioDesignDialysis Tubing, Carmel, NY). Once dialyzed, the protein solution was filtered using 0.8 $\mu$ m and 0.2 $\mu$ m surfactant free cellulose acetate syringe filters (Corning Incorporated, Corning, NY) to rid the solution of coarse non-specific metal oxides. Total protein concentration was obtained with a Coomassie Plus Bradford Assay Kit (Thermo Scientific, Rockford, IL). Inductively coupled plasma – optical emission spectroscopy (ICP-OES) of particles suspended in 2% nitric acid was used to measure metal concentrations. I repeated WFe-apoferritin nanoparticle synthesis and analysis six times, with similar results.

### 3.2.4 Synthesis of $Mn^{2+}$ WFe Nanoparticles

To synthesize a tungsten and iron filled apoferritin with  $Mn^{2+}$  ions adsorbed in the pores, both previous synthesis schemes (WFe and  $Mn^{2+}$  - magnetoferritin) were combined. Firstly, a previously characterized WFe nanoparticle solution was obtained as described herein. The concentration of  $MnCl_2$  and  $FeCl_2$  solutions were tailored depending on the protein concentration. A ratio of 2400 Mn and 24000 Fe ions per protein was calculated. The solution was suspended in 0.05M MES buffer at pH 8.5. The protein solution was de-aerated for at least 15 minutes and compensated for evaporation with previously de-aerated and heated 0.05M MES buffer.  $MnCl_2$  and  $FeCl_2$  were pumped at a rate of 12.5 $\mu$ l/min in alternate intervals of 10 minutes each for a total of 50 minutes. 200 $\mu$ l of 300mM of Sodium Citrate was added to chelate any unbound

metal. The solution was then sonicated for 10 minutes, spun for 10 minutes at 957 · g. And finally, the supernatant solution was collected and dialyzed overnight against deionized water using a 8,000 MW cut off dialysis tubing (BioDesignDialysis Tubing, Carmel, NY).

### 3.2.5 Electron Microscopy

Samples were adsorbed on 400 mesh Cu-C grids (Pacific GridTech, San Francisco, CA) and transmission electron microscopy (Artemov, et al.) images were obtained using a Philips CM12S Scanning Transmission Electron Microscope with EDAX 9800 plus an energy dispersive x-ray spectrometer fitted with a Gatan model 791 CCD camera for image acquisition (Electron Microscopy Facilities, Arizona State University). The microscope was loaded with a tungsten film and run at an accelerating voltage of 80keV. High Resolution Electron Microscopy (HREM) images were obtained using a Philips FEI CM-200 Transmission Electron Microscope fitted with a Gatan Orisis CCD camera for digital image acquisition and analysis. The microscope was loaded with a field emission gun (FEG) and used with an accelerating voltage of 200kV. Fast Fourier Transform patterns of the HRTEM images were obtained from 4 different particles and analyzed using ImageJ software (National Institutes of Health, Bethesda, MD).

### 3.2.6 Protein and Metal Assays

The resulting protein concentration was obtained using the Better Bradford Assay (Thermo Scientific, Rockford). Briefly, known serial dilutions of Bovine Serum Albumin (BSA) were stained with Coomassie Plus Reagent. The

reagent binds with certain aminoacids, which in turn result in a spectral shift (from brown to blue). This shift can be measured using a spectrophotometer or a plate reader measuring absorbance at around 595nm. For the experiments presented in this work, a wavelength of 570nm was used. The Bovine Serum Albumin concentrations and absorbance are used as a standard curve. The unknown sample concentrations are then obtained by interpolating their absorbance to those of the BSA standard curve.

Metal concentrations were obtained by means of Inductively Coupled Plasma-Optical Emission Spectroscopy. Briefly, the unknown samples were suspended in a solution containing 2% Nitric Acid. The acidic sample solution was then sprayed into the plasma flame from the ICP-OES where the molecules of interest collide with the electrons from the plasma flame and produce radiation at specific wavelengths. This radiation is categorized by wavelength and intensity to determine the concentration of each element of interest. Similarly to the protein colorimetric assay, a standard curve is used as a reference to determine the overall sample metal concentrations.

### 3.2.7 Relaxometry

Relaxometry was performed on the  $Mn^{2+}$  adsorbed magnetoferritin samples as follows. The samples were removed from dialysis and suspended in a 1% low melt agarose gel and vortexed to ensure homogeneous mixing. Relaxivity was measured using a MQ60 1.5T Bruker Minispec relaxometer (Bruker Optics, The Woodlands, TX). Bruker's curve-fitting tool was used to find the corresponding  $T_2$  values using a Carr-Purcell-Meiboom-Gill pulse sequence (CPMG) (Inter pulse  $\tau = 10ms$ , gain = 70, 200 points).  $T_1$  values were obtained

using the curve-fitting and the relaxation times were obtained with an Inversion Recovery (IR) pulse sequence (TI = 400ms, TR = 12s, 16 averages). Samples were maintained at 37°C during measurements.

Relaxometry was performed on the tungsten-iron (WFe) samples and the Mn<sup>2+</sup> adsorbed to tungsten iron particles as follows. 500µl samples of different ferritin concentrations were prepared and mixed with 500µl of 2% agarose gel to yield a 1% agarose/sample mix. Each gel solution was refrigerated for at least 15 minutes and later brought up to 37°C before measurement. Relaxivity was measured using a MQ60 1.5T Bruker Minispec relaxometer (Bruker Optics, The Woodlands, TX). Bruker's curve-fitting tool was used to find the corresponding T<sub>2</sub> values using a Carr-Purcell-Meiboom-Gill pulse sequence (CPMG) (Inter pulse τ = 4ms, gain = 62, TR = 15s, 75 points). T<sub>1</sub> values were obtained using the curve-fitting and the relaxation times were obtained with an Inversion Recovery pulse sequence (First TI = 5ms, last TI = 20,000ms, duration factor = 2.513, TR = 15s, 8 averages, 10 points).

### 3.2.8 Electron Paramagnetic Resonance

Electron paramagnetic resonance (EPR) experiments were performed at the EPR Facility at Arizona State University. EPR spectra were recorded at 5 K using a Bruker ELEXSYS 580 X-band spectrometer (Bruker, Silberstreifen, Germany) equipped with an Oxford Model 900 EPL liquid helium cryostat (Oxford Instruments, Oxfordshire, UK). The magnetic field modulation frequency was 100 kHz, the amplitude was 1 mT, the microwave power was 1 mW, the microwave frequency was approximately 9.42 GHz and the sweep time was 168 seconds. The spectra were obtained by averaging several scans.

The EPR spectra were simulated using EasySpin (v 3.1.1), a computational package developed by Stoll and Schweiger and based on Matlab (The MathWorks, Natick, MA, USA). One single  $Mn^{2+}$  ion ( $S = 5/2$ ,  $I = 5/2$ ) was considered for the simulations. The fitting parameters were the following: the isotropic  $g$  value, the line width,  $\Delta B$ , the zero-field splitting parameters,  $D$  and  $E$ , and the isotropic hyperfine coupling,  $a$ .

### 3.2.9 *In vivo* Imaging

All animal experiments were approved by the animal care and use committee and complied with the National Institutes of Health guidelines. Adult male Sprague Dawley rats were anesthetized with a Ketamine/Xylazine cocktail (90mg/kg ketamine, 5mg/kg xylazine). The coordinates for injection were identified as the caudate/putamen, 1.6mm anterior, 3mm lateral (each hemisphere) from the bregma and 5mm interior from the dura. Once the points were identified, burr holes were made using a pneumatic drill. A Hamilton syringe was mounted onto the microinjector unit of the 900M model Stereotactic frame (David Kopf Instruments, Tujunga, CA). 10 $\mu$ l of either the experimental agent or native ferritin at the same concentration were injected over the course of 5min. Once injected, the animals were scanned in a 7T small animal, 30cm-horizontal bore magnet, and Biospec Advanced III Spectrometer (Bruker, Billerica, MA), 116mm high power gradient set (600mT/m) and a whole body rat transmit/receive surface coil. An IRTrueFISP sequence (TE/TR= 2.2/4.4ms, flip angle= 60 $^{\circ}$ ) and a MSME sequence (TE/TR= 11/2500ms, flip angle= 180 $^{\circ}$ ) were performed to obtain the  $T_1$  and the  $T_2$  weighted images for the  $Mn^{2+}$  adsorbed magnetoferritin. While for the WFe apoferritin nanoparticles the *in vivo* imaging

parameters were the following. The particles were injected into the striatum of a rat in the caudate/putamen 1.6mm anterior and 3mm lateral from the bregma. To breach the skull, I created two burr holes in the skull bilaterally at the stereotactic coordinates using a drill. A 10 $\mu$ L Hamilton syringe needle (Sigma Aldrich, St. Louis) was inserted 6mm below the dura. The needle remained in place for 1 minute and then was retracted to 5mm below the dura. 8 $\mu$ L of WFe and control (native ferritin) were injected over the span of 5 minutes into the left and right hemispheres, respectively. The rat was imaged on a Bruker 7T/30 scanner (three-axis gradient, slew rate of 150 T/m/s) using a rat surface RF coil. Isoflurane gas and oxygen were delivered during the scan. To image the striatum, a fast low-angle shot pulse sequence (FLASH) was used (TE/TR= 3.8ms/55.9ms, NEX 4), and a T<sub>1</sub>-map RARE pulse sequence, TE/TR = 10.88ms/233.3ms, 500ms, 1200ms, 2500ms, 5000ms, NEX 1.

### 3.3 Results and Discussion

#### 3.3.1 Synthesis and Particle Characterization

##### 3.3.1.1 Mn<sup>2+</sup> Adsorbed to Hydrophilic Channels of Magnetoferritin

To fill the protein and adsorb Mn<sup>2+</sup> to the hydrophilic channels, the reconstituted protein was synthesized by incubating 2 $\mu$ M apoferritin with 4.8mM MnCl<sub>2</sub> and 48mM FeCl<sub>2</sub> under N<sub>2</sub>. Briefly, four MnCl<sub>2</sub> additions of 125 $\mu$ l every ten minutes were alternated with four additions of 48mM FeCl<sub>2</sub> for a total reaction time of 200 minutes (total of 20 metal additions, 12 MnCl<sub>2</sub> and 8 FeCl<sub>2</sub>). Subsequently, the product was dialyzed overnight against 0.15M NaCl and filtered using a magnetic column. Protein and metal concentrations were obtained with a Bradford assay and ICP-OES, respectively. Incorporating iron

into the core through the ferroxidase of the protein and binding  $Mn^{2+}$  into the hydrophilic channels of the protein allow for the surrounding water molecules to interact with both the superparamagnetic crystal core and the paramagnetic ions as it exchanges with the bulk water (Figure 14a).

Transmission electron microscopy (TEM) of the resulting nanoparticles showed a monodisperse particle distribution and highly filled protein cores (Figure 14b). When bovine serum albumin was added instead of apoferritin, no particles formed (data not shown). Figure 14c shows the particle size distribution measured from images of native ferritin, magnetoferritin, and  $Mn^{2+}$ -Magnetoferritin. Native gel electrophoresis showed that the manganese magnetoferritin particles, native ferritin, and apoferritin all ran at the same molecular weight (Data not shown). Evidence of a crystalline oxide formation in the core of the protein is shown on the HREM images (Figure 14b). All particles in the sample had a lattice spacing of  $2.5\text{\AA}$ , consistent with the 222 and 311 interplanar spacing of magnetite crystals (Cranfield, et al., 2004). I conclude that the manganese ions did not disrupt the lattice formation of the iron oxide.

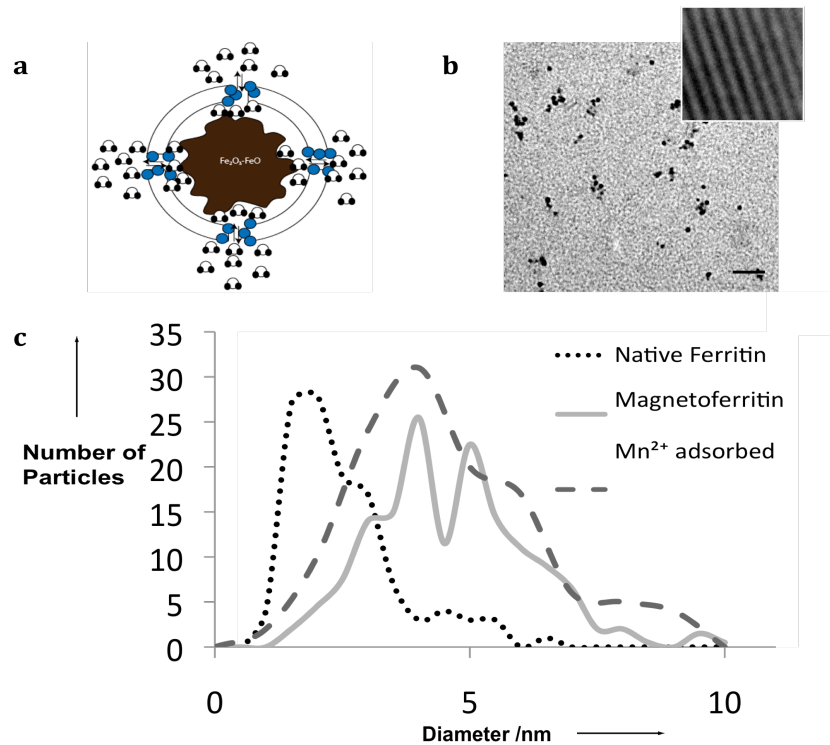


Figure 14. (a) Schematic Mn<sup>2+</sup> adsorbed to a partially loaded apoferritin cavity. Blue circles represent Mn<sup>2+</sup> interacting with water molecules. (b) TEM and HREM of Mn<sup>2+</sup>-magnetoferritin, (c) Size distribution of native ferritin (dotted line), magnetoferritin (solid line) and Mn<sup>2+</sup>-magnetoferritin (dashed line). Scale bars are 50nm.

### 3.3.1.2 Tungsten-Iron (WFe) Filled Apoferritin

A mixed metal oxide was formed in the apoferritin protein. Apoferritin is useful as a “natural” contrast agent for MRI because it is uniform in size, contains multiple surface functional groups, and is relatively immunologically inert (Beeman, Georges, & Bennett; Bulte, et al., 1995). To create the WFe composite, an iron oxide core was formed in apoferritin, as previously described (Jordan,

Caplan, & Bennett), by filling apoferritin with iron using the intrinsic ferritin ferroxidase. I incorporated both tungsten and iron into the apoferritin core. After synthesis, dialysis, and purification, the ferritin nanoparticle core comprised an electron-dense metal crystal about 6nm in diameter, as demonstrated with transmission electron microscopy (TEM, Figure 15b). The WFe-apoferritin yield was 10%.

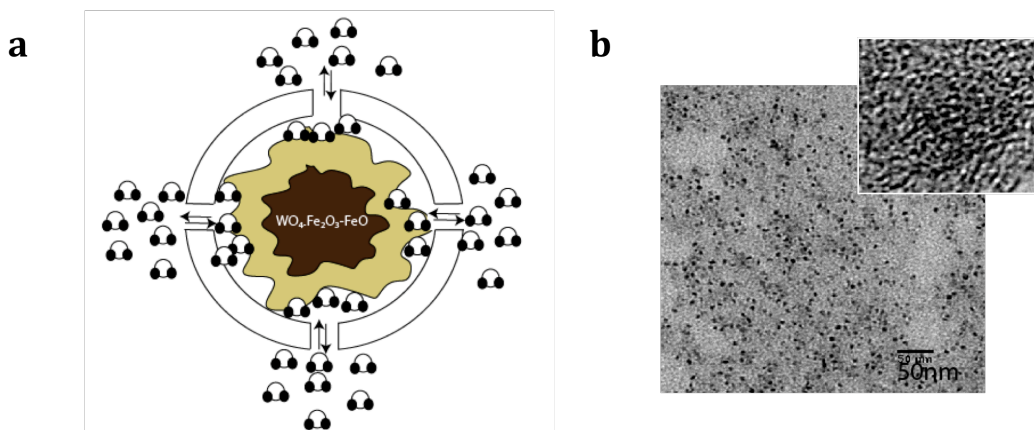


Figure 15. a) Schematic illustrating the interaction between the crystal and the surrounding water molecules in the WFe-apoferritin particle. Yellow shell indicates the tungsten-iron composite surrounding a small iron oxide core. b) TEM and HREM of WFe-Apoferritin, electron dense cores are the composite formed inside the protein shell. HREM shows no lattice spacings in the crystal core.

### 3.3.1.3 $Mn^{2+}$ Adsorbed to Tungsten-Iron Filled Apoferritin

In order to optimize the  $r_2$  and  $r_1$  characteristics of the particles I combined the synthesis of  $Mn^{2+}$  adsorbed to apoferritin, and the tungsten-iron composite. To create this new particle, the synthesis scheme was split in two stages. The first stage was to load the apoferritin core with the tungsten iron composite as

outlined previously. Subsequently, once the tungsten-iron composite was characterized, the manganese ions were adsorbed onto the hydrophilic channels (Figure16). After synthesis, dialysis, and purification, the resulting particle suspension was observed under the transmission electron microscope (Artemov, et al.). Figure 16b shows the images of the MnWFe particles dispersed onto the TEM grids. The yield of reaction was 5%.

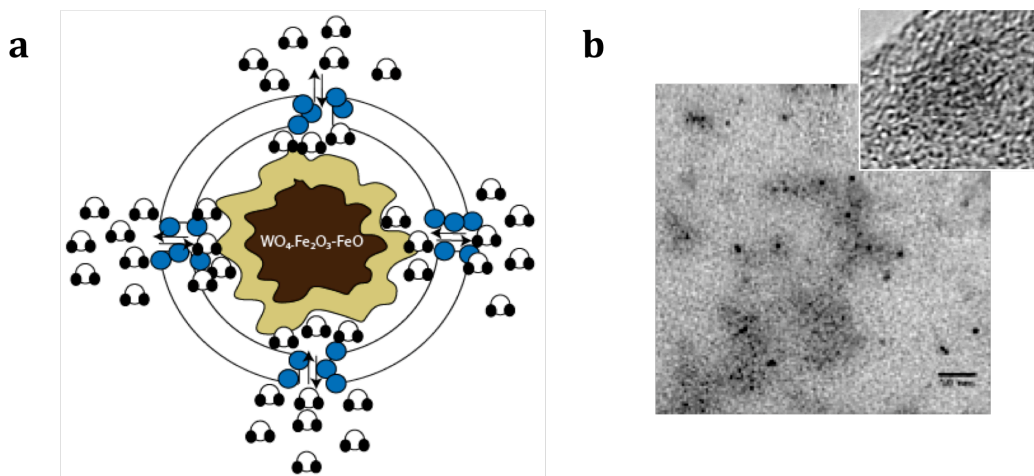


Figure 16. a) Schematic of the particle metal atoms and their interaction with the water molecules. Blue circles are  $Mn^{2+}$  atoms adsorbed to apoferritin hydrophilic channels. b) TEM and HREM of MnWFe particles. Scale bar is 50nm.

### 3.3.2 Relaxivity and *in vivo* imaging

To determine the effectiveness of these particles, their respective transverse and longitudinal relaxivities were obtained for all the particles proposed herein.

Different synthesis schemes were performed to optimize the combination of  $MnCl_2$  and  $FeCl_2$ .  $r_1$  was the most sensitive to manganese concentration; the optimal concentration results in a relaxivity change of approximately 80%. This is

likely due to the fact that  $\text{Fe}^{2+}$  and  $\text{Mn}^{2+}$  compete for the same binding sites located in the hydrophilic channels of the protein. Relaxometry results of particles synthesized with 48mM  $\text{FeCl}_2$  and 4.8mM  $\text{MnCl}_2$  showed an enhanced per-particle and per-ion relaxivity, as shown in Table 2. Interestingly, manganese adsorbed particles only show an increase in  $r_1$  when the core is magnetically filtered and highly filled. The per-ion  $r_1$  for the  $\text{Mn}^{2+}$  adsorbed particles increased by a factor of 40 compared to  $\text{MnCl}_2$  in solution ( $R_1= 330 \text{ mM}^{-1}\text{s}^{-1}$ ). Similarly, the per-ion  $r_2$  increased by a factor of  $\sim 10$  compared to native ferritin. Using volumetric relaxivity, which takes into account the particle relaxivity and nanoparticle size, this agent is more effective than magnetoferritin as a  $T_1$  agent, with a volumetric relaxivity of  $2.1 \text{ mM}^{-1}\text{s}^{-1}\text{nm}^{-3}$  (for  $\text{Mn}^{2+}$ - Magnetoferritin) compared to  $0.35 \text{ mM}^{-1}\text{s}^{-1}\text{nm}^{-3}$  (for magnetoferritin). Conversely, its volumetric  $T_2$  relaxivity of  $193.4 \text{ mM}^{-1}\text{s}^{-1}\text{nm}^{-3}$  is less than that of magnetoferritin.

Table 2  
 *$\text{Mn}^{2+}$  Adsorbed to Magnetoferritin Relaxivity Summary*

		$r_2$	$r_1$
Mn <sup>2+</sup> adsorbed particles	Fe	133	1.449
	Mn	31,112	338.6
	Particle	222,481	2421
	Volumetric	193.40	2.10
Magnetoferritin particles	Fe	78	0.07
	Particle	404,045	407
	Volumetric	351.23	0.35

Mn<sup>2+</sup> adsorbed particles, and magnetoferritin particles relaxivities based on iron, particle concentrations and volume of particle. For transverse ( $r_2$ ) and longitudinal ( $r_1$ ) relaxivities, a CPMG and an IR pulse sequence was used, respectively.

To investigate their utility for *in vivo* applications, the  $Mn^{2+}$  magnetoferritin particles were injected into a rat striatum and imaged in a 7T animal scanner. Although the  $T_2$  relaxivity was still high in comparison to existing iron oxide agents, the  $T_1$  effect was nonetheless detected *in vivo* using an IRTrueFISP pulse sequence. Figure 17 shows the stereotactic injection into the caudate/putamen of a male adult Sprague Dawley rat. 10 $\mu$ l of 76nM of agent and native ferritin were injected to both sides of the brain. Using the IRTruFISP pulse sequence the agent was detected with  $T_1$  weighting, while the native ferritin side did not show any hyperintensity in the area of injection. With a MSME pulse sequence, a  $T_2$  weighted image was created and at that concentration native ferritin was not detectable while the  $Mn^{2+}$  magnetoferritin agent showed a clear hypointensity on the area of injection.

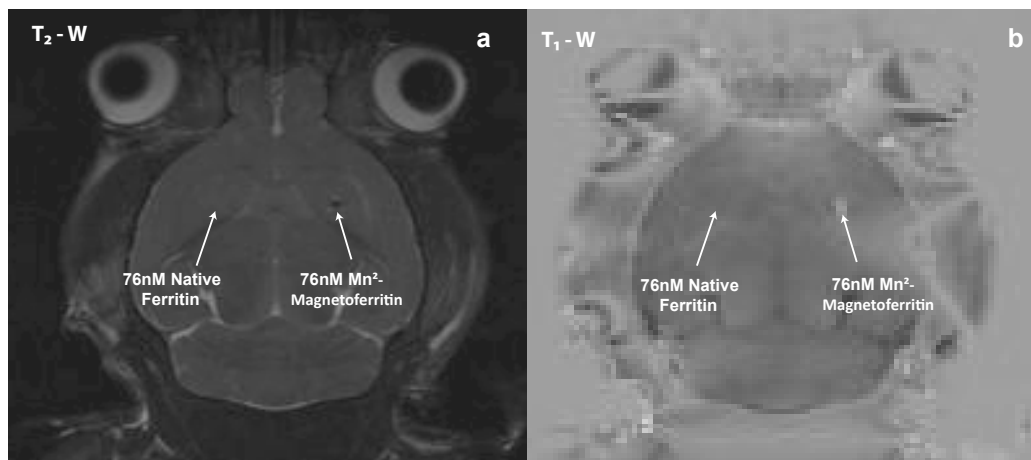


Figure 17. (a) 3D imaging of Sprague Dawley rats injected with 76nM native ferritin (left hemisphere) and manganese doped magnetoferritin (right hemisphere) MSME  $T_2$  map TE/TR=111/2500ms. (b) 76 nM Manganese doped Magnetoferritin IR TrueFISP  $T_1$  weighted image TE/TR= 2.2/4.4, flip angle= 60°, TI=90ms.

Although this agent was detected *in vivo*, it is important to denote that in order to be able to detect this agent using  $T_1$ -weighting techniques, a specific sequence needed to be used. The main limitation of this technique is that as it can be seen in Figure 17b much of the anatomical detail is lost since the hyperintensity was only observed at high flip angles ( $\alpha=60^\circ$ ). Therefore, this specific  $r_2/r_1$  configuration poses a limitation for imaging and agents with a low  $r_2/r_1$  are much needed.

The tungsten-iron composites in apoferritin performed much better since they resulted to be agents with the lowest  $r_2/r_1$  reported to date. Making them very attractive for *in vivo* imaging with  $T_1$  weighting pulse sequences.

Table 3.  
*WFe-Apoferritin Relaxometry Summary*

	WFe- apoferritin particle relaxivity ( $\text{mM}^{-1}\text{s}^{-1}$ )	WFe - apoferritin metal relaxivity ( $\text{mM}^{-1}\text{s}^{-1}$ )	WFe - apoferritin surface metal relaxivity ( $\text{mM}^{-1}\text{s}^{-1}$ )
$r_1$	4870.27	0.63	2.62
$r_2$	9076.67	1.04	4.89
$r_2/r_1$	1.86	1.67	1.86

Relaxometry of WFe-apoferritin nanoparticles *in vitro*. All relaxivity measurements were performed at 1.5T, 37°C with particles suspended in 1% agarose.  $T_2$  and  $T_1$  relaxation times were obtained with a Carr-Prucell-Meiboom-Gill and an Inversion Recovery pulse sequence, respectively.

The addition of sodium tungstate during reaction at different levels resulted in the following relaxivity profile.

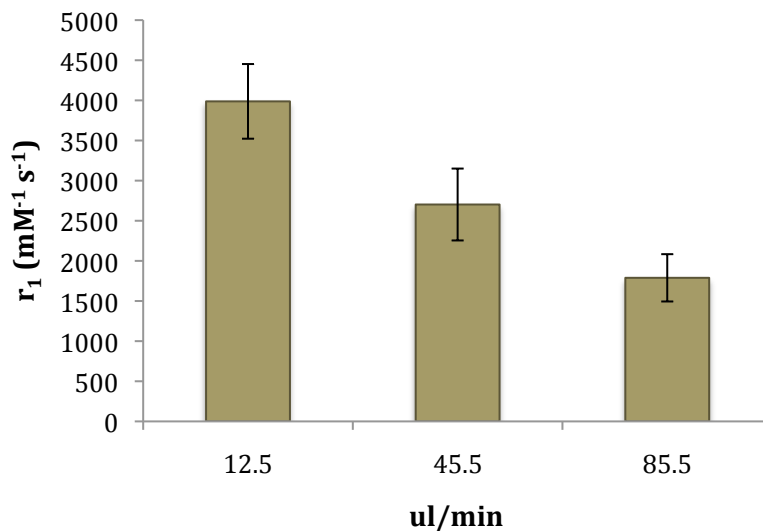


Figure 18.  $T_1$  relaxivity profile for increasing tungstate additions. As the rate increases the measured  $r_1$  decreases significantly.  $T_2$  relaxivity was not included in this plot as it was negligible.

This technique offers a viable way to tune  $T_1$  relaxivity by tuning the tungsten addition rate.

The WFe nanoparticles had a particle  $r_1$  of  $4870 \pm 1199 \text{mM}^{-1} \text{s}^{-1}$  and an  $r_2/r_1$  ratio of 1.86 at a magnetic field strength of 1.5T, as summarized in Table 4. To my knowledge, this is the lowest  $r_2/r_1$  reported in a nanoparticle agent. Because the interaction between the magnetic moment of the water protons and the electronic moment of the nanoparticle is local, the increased  $r_1$  of the WFe nanoparticle is likely due to an interaction with protons at the outer surface of the crystal. This increased  $r_1$  can be likely due to the enhanced proton exchange at the surface of apoferritin observed by Vasalatiy et al. (Vasalatiy, Zhao, Zhang, Aime, & Sherry, 2006) To account for the expected strong surface contribution to  $r_1$ , I computed a “surface relaxivity” that is the atomic relaxivity of the estimated

number of atoms on the crystal surface (Table 3, third column). With this relaxivity, WFe-apoferritin should be detectable with  $T_1$ -weighting in the brain, for example, in about 20nM-400nM concentrations, assuming a normal tissue  $T_1$  and  $T_2$  of 1084ms and 69ms, respectively (Stanisz, et al., 2005). Above these concentrations, I expect the WFe particles to be primarily detected as  $T_2$ -shortening agents. The WFe nanoparticles are therefore practical for  $T_1$ -weighted MRI in sub- $\mu$ M concentrations, *in vivo*.

The main goal of combining the synthesis schemes ( $Mn^{2+}$  adsorbed apoferritin and the WFe composite) was to minimize the particle  $r_2$  and maximize the particle  $r_1$ . In these particles, adding  $Mn^{2+}$  during synthesis led to an increased  $r_2$  of  $29046\text{mM}^{-1}\text{s}^{-1}$  and decrease per ion  $r_1$  to  $118\text{mM}^{-1}\text{s}^{-1}$ , suggesting that water access to the W-Fe core is critical for the high  $r_1$  of the W-Fe composite nanoparticles. This combined approach particle should be detectable with  $T_1$ -weighting in 40-125nM concentrations, narrowing the window of detection significantly.

The MnWFe particles had similar relaxivities but the per- $Mn^{2+}$   $r_1$  was significantly reduced when adsorbed to these WFe-filled apoferritins.

Table 4.  
*Mn<sup>2+</sup> Adsorbed to WFe-Apoferritin Relaxivity Summary*

	Particle $\text{mM}^{-1}\text{s}^{-1}$	Metal $\text{mM}^{-1}\text{s}^{-1}$	$Mn^{2+}$ $\text{mM}^{-1}\text{s}^{-1}$
$r_1$	2306.00	0.26	118.81
$r_2$	29046.00	3.45	1686.63
$r_2/r_1$	12.6	11.7	14.2

$Mn^{2+}$  adsorbed to WFe longitudinal and transverse relaxivities at were performed at  $37^\circ\text{C}$ , 1.5T, and in 1% agarose.

### 3.3.3 Solomon Bloembergen Morgan (SBM) Simulations

As described in the introductory section, the SBM Equations describe proton relaxation due to local dipolar coupling between the electronic paramagnetic moment and the water proton moment.

With this model in mind, one possible explanation for the increase in longitudinal relaxivity, is that by adsorbing these ions onto the channels, where water exchange occurs, both the inner and outer sphere relaxation contributions ( $r_1^{IS}$  and  $r_1^{SS}$ ) are maximized. Figure 19b shows that the relaxivity of  $330\text{mM}^{-1}\text{s}^{-1}$  obtained experimentally, can be attained for a frequency of approximately 60MHz. This result was obtained by manipulating the following parameters: Reducing the ionic radius ( $r_{MH}$ ), increasing the hydration number (Querol & Bogdanov), and the rotation correlation time ( $\tau_R$ ). In turn, I believe that the residence time ( $\tau_M$ ) can be increased due to apoferritin catalytic effects on water proton exchange. Figure 19a shows the simulated  $r_1^{IS}$ , and the residence times ( $\tau_M$ ) that lead to the highest relaxivities. The simulation parameters that were adjusted are the following:  $\tau_M=50\text{ns}$ ,  $\tau_R = 50\text{ns}$ ,  $r_{MH} = 2.14 \text{ \AA}$ ,  $q^{IS} = 6$ , and  $q^{SS} = 15$ . All other variables were considered constant and obtained from literature (Caravan, et al., 2009). With these parameters, it is possible to achieve relaxivities that result in approximately a  $r_1^{\text{obs}}$  of  $200\text{-}300\text{mM}^{-1}\text{s}^{-1}$  for clinical field strengths (0.5-3T)

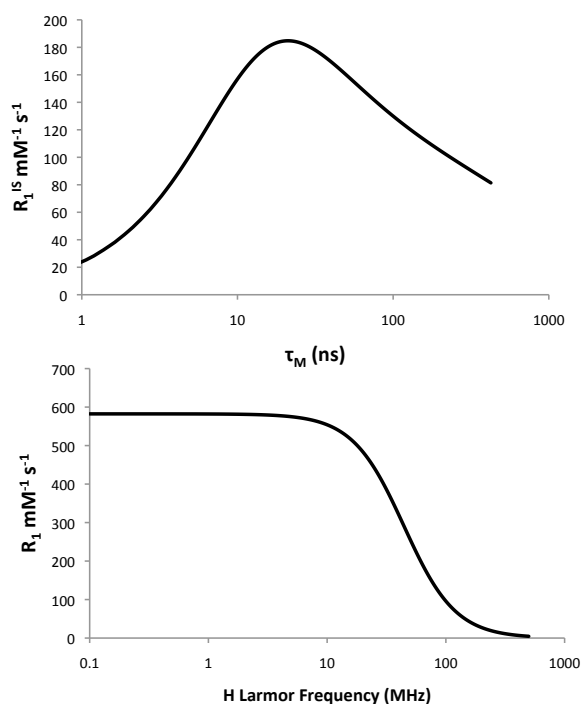


Figure 19. a) Inner sphere relaxivity ( $r_1^{IS}$ ) simulated with Solomon-Bloembergen-Morgan model. Inner sphere relaxivity  $r_1^{IS}$  is highest for a residence time within 10-100ns. b) Nuclear magnetic resonance dispersion (NMRD) simulation for  $\text{Mn}^{2+}$  adsorbed Magnetoferritin showing an observed relaxivity ( $r_1^{obs}$ ) of  $\sim 300 \text{mM}^{-1} \text{s}^{-1}$  at clinical strength frequencies (i.e.  $\sim 60 \text{mHz}$ ).

### 3.3.4 Electron Paramagnetic Resonance

To confirm that the  $\text{Mn}^{2+}$  ions were coordinated to the protein rather than in solution or inserted into the iron oxide crystal core, electron paramagnetic resonance (EPR) was performed on a buffered  $\text{MnCl}_2$  solution, magnetoferritin and  $\text{Mn}^{2+}$ -magnetoferritin. X-band EPR spectra were measured at 5 K for all samples. For manganese chloride in solution, a multi-line EPR spectrum is observed containing sixteen peaks centered at the magnetic field corresponding

to  $g = 2.0$  (Figure 20, solid line top). This spectrum is very similar to those previously reported for Mn (Miyawaki, et al.) (Stich, et al., 2007). Figure 20 (solid line bottom panel) shows the EPR spectrum corresponding to  $\text{Mn}^{2+}$  adsorbed magnetoferritin. The spectrum also contains sixteen peaks centered at the field corresponding to  $g = 2.0$ . However, a close inspection reveals subtle differences in the shape and intensity of several peaks in the spectrum. Most notably, the resonances at the lowest  $g$  values around  $g = 1.89$  are observably different.

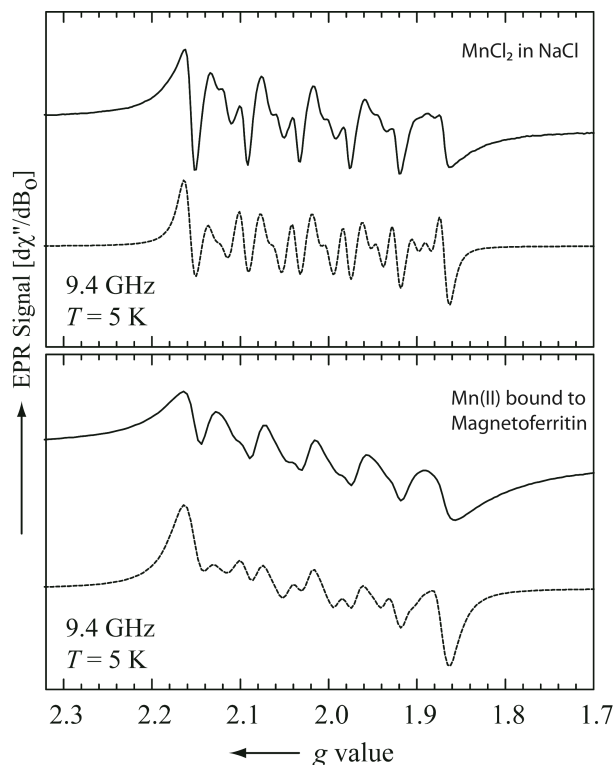


Figure 20. Original and simulated EPR spectra of  $\text{MnCl}_2$  in NaCl (top panel) and  $\text{Mn}^{2+}$  adsorbed to magnetoferritin (bottom panel). Total manganese concentration was 1mM.

To understand the differences mentioned above, the spectra were simulated and fitted to the following parameters: the isotropic g value, the line width, DB, the zero-field splitting, D and E, and the isotropic hyperfine coupling, a (Weil, Bolton, & Wertz, 1994). Figure 20 (dashed lines) also shows the simulated spectra. The fitting parameters corresponding to the samples are summarized in Table 5. Thus, the main difference between the spectra is associated with their line width. For  $\text{MnCl}_2$  in solution the line width is 2.2 mT, which is due to a weak interaction with distant protons in the solvent. Whereas for  $\text{Mn}^{2+}$  adsorbed magnetoferritin the line width is 4.0 mT (almost double). The increase in the line width indicates a definite coordination to the protein matrix. In which a  $\text{Mn}^{2+}$  ion interacts with other incorporated  $\text{Mn}^{2+}$  ions and possibly with iron ions at the core. Most likely, both interactions are dipole-dipole interactions. However, this coordination seems to be weak because the value for D is small, which is consistent with long electronic spin distances. In contrast, magnetoferritin only showed signal corresponding to  $\text{Fe}^{3+}$  within the crystal (g-value = 4.3).

Table 5  
EPR Parameter List

<b>Parameters</b>	<b>MnCl<sub>2</sub> in NaCl</b>	<b>Mn<sup>2+</sup> - Magnetoferritin</b>
<i>g</i>	2.000	1.999
$\Delta B$ (Nasongkla, et al.)	2.2	4.0
D (MHz)	< 200	< 200
E (MHz)	< 67	< 67
<i>a</i> [MHz]	268	261

Parameters used in the simulations of EPR spectra of Mn<sup>2+</sup> in solution and as bound to magnetoferritin. The sub-spectra corresponding to allowed and forbidden transitions were calculated separately and combined in an approximate 1:1 ratio to yield the final spectrum.

### 3.4 Conclusions

I conclude that the strategic placement of manganese ions near sites of water exchange can significantly enhance the per-ion  $r_1$ , suggesting a mechanism for increasing the per-ion relaxivity in porous nanoparticle agents. Together, the increased per-ion  $r_1$  and the EPR data indicate that the manganese ions are indeed coordinated to the protein and most likely clustered in the hydrophilic channels as identified by Wardeska et al. (Wardeska, Viglione, & Chasteen, 1986). Thus, by clustering the manganese ions to the channels and confining the water molecules within the iron crystal and the protein core, it is possible to enhance  $r_1$ . Vasalaty and co-workers showed that the core of the apoferritin protein possesses catalytic effects on the proton exchange and that it could be enhanced if the water exchange through the protein hydrophilic pores were to be hindered. Specifically for the particles in this work, it was noted that

the magnetic filtration step yields protein cores that are filled and likely create a smaller water-filled cavity. This is supported by the fact that relaxivity only increased in particles that were magnetically filtered.

The particle  $r_1$  can be increased without increasing  $r_2$  by forming a W-Fe composite inside apoferritin. SBM simulations support the idea that by confining paramagnetic moments to the surface of the particle either in the form of adsorbed paramagnetic atoms or in the form of uncoupled crystal surface moments, it is possible to maximize  $r_1$ . While allowing for water to access the crystal core and to interact with surface magnetic moments and also tumble at the right rate due to the particle size, it is possible to maximize  $r_1$  and minimize  $r_2$ . With this low  $r_2/r_1$  it is possible to detect concentrations ranging in the tens of nanomolar *in vivo*. The discovery of a synthesis scheme that results in particles with the lowest reported  $r_2/r_1$  to date is of great interest in the field of magnetic resonance molecular imaging. Thus, a more in depth study of the mechanism of action and its applications was deemed appropriate and is presented in the following sections.

## CHAPTER 4

### CHARACTERIZATION AND ANALYSIS OF TUNGSTEN-IRON (W-FE)

#### APOFERRITIN NANOPARTICLE

##### 4.1 Introduction

Researchers often improve MRI contrast agents by increasing the transverse ( $T_2$  or  $T_2^*$ ) or longitudinal ( $T_1$ ) relaxivity. The relaxivity ( $r_2$  or  $r_1$ ) is a model of the impact of the agent on the relaxation times and consequently on image contrast. Since most tissues have longer intrinsic  $T_1$  compared to  $T_2$  (Stanisz, et al., 2005), a  $T_1$ -shortening agent can be detected in ~30-fold lower concentrations than a  $T_2$ -shortening agent of similar relaxivity.  $T_1$ -shortening agents may also be more readily distinguished in practice because  $T_2$  or  $T_2^*$  changes can resemble intrinsic image artifacts.  $T_1$ -shortening agents are often formed by the localized magnetic moment of unpaired electrons in a valence orbital of single atoms. In comparison, many  $T_2$ - and  $T_2^*$ -shortening contrast agents are often formed by exchange coupling between multiple atoms in an oxide crystal. This coupling yields a greater net magnetic moment than the sum of the uncoupled moments of the component metal atoms. Thus, while  $T_1$ -shortening agents are often more desirable,  $T_2$ - and  $T_2^*$  shortening agents can be more readily conferred a high relaxivity and metal payload. An example of this phenomenon is seen in the development of magnetic nanoparticles. Magnetic nanoparticles are useful as contrast agents because they are often stable *in vivo*, have a high metal payload, and can be readily functionalized. Unfortunately, attempts to create nanoparticle agents with high  $r_1$  usually result in a simultaneous enhancement in  $r_2$  and  $r_2^*$  (Kalman, Geninatti-Crich, & Aime; T. Kim, Momin, et al.; Sana, Poh, & Lim; W. S. Seo, et al., 2006; Taylor, Rieter, & Lin,

2008). This limits the range of concentrations over which the agent can be detected with  $T_1$ -weighted imaging and limits the sensitivity to the imaging target.

Several groups have developed  $T_1$ -shortening agents with enhanced  $r_1$  (Aime, Frullano, & Geninatti Crich, 2002; Kalman, et al.; T. Kim, Cho, et al.; T. Kim, Momin, et al.; Na, et al., 2007; Sana, et al.). Kim et al reported a metal oxide based 2-10 nm particle with a relatively low  $r_2/r_1$  of  $\sim 4$ -25 (T. Kim, Momin, et al.). The smallest nanoparticles had a low  $r_2$  because of surface defects that created localized, rather than de-localized spins. Modulating  $r_2/r_1$  with nanoparticle size is an important advance in nano-scale magnetism and magnetic resonance relaxation. Because of the wide range of applications for MRI contrast agents of varying sizes, there is still a need for a general, flexible technique to create nanoparticles with low  $r_2/r_1$ .

To address this need, chemical doping is proposed to create a  $T_1$ -shortening nanoparticle with low transverse relaxivity. In crystals of  $3d$  transition metals, the atoms are often coupled through electron exchange. Paramagnetic metals contain atoms with localized magnetic moments, either because the electronic wave functions of the atoms do not overlap, or because they are physically separated, as illustrated in Figures 21a and 21b. If a dopant is strategically incorporated into the metal crystal, it may be possible to prevent exchange coupling and localize the magnetic moments of the component atoms, creating a paramagnetic,  $T_1$ -shortening nanoparticle contrast agent with a high metal payload. If established, chemical doping could facilitate metal oxide nanoparticles with tunable size and  $r_2/r_1$ .

To investigate this concept, I formed a mixed metal oxide in the apoferritin protein. Apoferritin is composed of 24 subunits (of either H- or L- forms) that form

a spherical cage with ~ 13 nm diameter and a ~8nm core. The H-ferritin subunit contains a ferroxidase that converts  $\text{Fe}^{2+}$  to  $\text{Fe}^{3+}$ . The ferroxidase can be used to create a nanoparticle contrast agent from apoferritin, suitable for *in vivo* targeting and delivery for MRI (Aime, et al., 2002; Arosio, et al., 2009; Bulte, Douglas, Mann, Frankel, Moskowitz, Brooks, Baumgarner, Vymazal, & Frank, 1994; Cormode, Jarzyna, Mulder, & Fayad; Jordan, et al.; Meldrum, Douglas, Levi, Arosio, & Mann, 1995; Meldrum, et al., 1992; Uchida, et al., 2008). Apoferritin is useful as a “natural” contrast agent for MRI because it is uniform in size, contains multiple surface functional groups, and is relatively immunologically inert (Beeman, Georges, et al.; Bulte, et al., 1995).

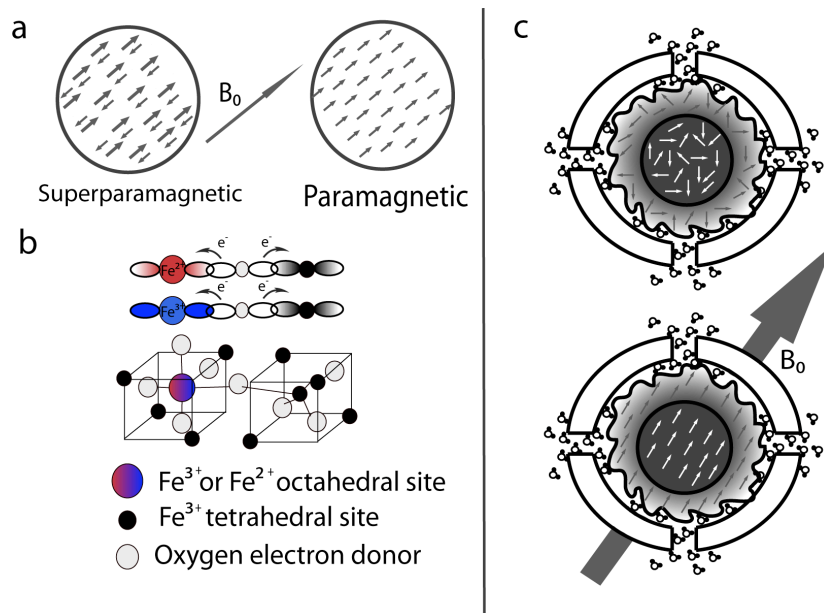


Figure 21. Schematic of atomic spin coupling in a nanoparticle to form a superparamagnetic or paramagnetic crystal. a) De-localized electron spins in a super-paramagnet and localized electron spins in a paramagnet, both exposed to an external magnetic field. b) Metal and oxygen atoms in a spinel crystal arrangement with octahedral and tetrahedral sites occupied by  $\text{Fe}^{2+}$  or  $\text{Fe}^{3+}$

atoms.  $3d$  orbital and  $p$  orbital overlap, facilitating electron spin coupling. c) Randomly aligned spins without an external field and aligned spins with an external magnetic field inside the apoferritin shell. Water molecules in close proximity interact with the surface of the paramagnetic crystal core.

## 4.2 Methods

### 4.2.1 Synthesis of Paramagnetic WFe Nanoparticles with Different Tungsten Loadings

To synthesize a tungsten and iron oxide filled apoferritin,  $2\mu\text{M}$  apoferritin (Sigma Aldrich, St. Louis, MO) was buffered in 0.05M Morpholino Ethanesulfoxide (MES) at pH 8.5. In separate containers I used 48mM  $\text{FeCl}_2$  (Sigma Aldrich), and 48mM  $\text{Na}_2\text{WO}_6$  (Sigma Aldrich). All solutions were de-aerated for at least 15 minutes with  $\text{N}_2$ , then kept in a water bath at 55 to 60°C under vacuum. Any apoferritin solution that evaporated during the de-aerating period was compensated by adding a previously de-aerated 0.05M MES buffer to maintain a constant volume throughout the reaction. I added the de-aerated 48mM  $\text{FeCl}_2$  at a rate of  $12.5\mu\text{l}/\text{min}$  to the apoferritin solution using a syringe pump for a total of 140 minutes. Fifty minutes into  $\text{FeCl}_2$  delivery, the de-aerated 48mM  $\text{Na}_2\text{WO}_6$  was added at a rate of  $12.5\mu\text{l}/\text{min}$ ,  $45.5\mu\text{l}/\text{min}$ , and  $85\mu\text{l}/\text{min}$  using a syringe pump for a total of 40 minutes. A total of 1.75ml of  $\text{FeCl}_2$  and 500 $\mu\text{l}$  of  $\text{Na}_2\text{WO}_6$  were added to the protein solution. 200 $\mu\text{l}$  of 300mM sodium citrate was added to the solution to chelate any remaining metal ions. The solution was then sonicated for 10 minutes and spun for 10 minutes at  $957 \cdot g$ . Finally, the supernatant solution was collected and dialyzed overnight against 3L of de-ionized water using a 8,000 MW cut off dialysis tubing (BioDesignDialysis

Tubing, Carmel, NY). Once dialyzed, the protein solution was filtered using 0.8 $\mu$ m and 0.2 $\mu$ m surfactant free cellulose acetate syringe filters (Corning Incorporated, Corning, NY) to rid the solution of coarse non-specific metal oxides.

#### 4.2.2 Concentration Assays and Relaxometry

Total protein concentration was obtained with a Coomassie Plus Bradford Assay Kit (Thermo Scientific, Rockford, IL) as outlined in the previous chapters. Inductively coupled plasma – optical emission spectroscopy (ICP-OES) of particles suspended in 2% nitric acid was used to measure metal concentrations also outlined in previous chapters.

#### 4.2.3 Size Exclusion Chromatography

Size exclusion chromatography (SEC) was used in order to determine the monodispersity of the samples and rule out non-specific oxidation outside the protein. Samples suspended in water were injected into a Beckman System Gold HPLC mounted with a Phenomenex BioSep-SEC-S4000 column and 0.05M NaCl at pH 7.12 mobile phase. 100 $\mu$ l of sample was injected at a time and absorbance was monitored for at least 35minutes at 280nm and 410nm for elution of protein and metal, respectively.

#### 4.2.4 Transmission Electron Microscopy

Samples were adsorbed on 400 mesh Cu-C grids (Provided by the WM Keck Bioimaging Laboratory) and transmission electron microscopy, TEM, images were obtained using a Philips CM12S Scanning Transmission Electron

Microscope with EDAX 9800 plus an energy dispersive x-ray spectrometer fitted with a Gatan model 791 CCD camera for image acquisition (Electron Microscopy Facilities, Arizona State University). The microscope was loaded with a tungsten film and run at an accelerating voltage of 80keV. High Resolution Electron Microscopy (HREM) images were obtained with a Philips FEI CM-200 Transmission Electron Microscope fitted with a Gatan Orisis CCD camera for image capture.

#### 4.2.5 Energy Dispersive Spectroscopy

Energy Dispersive Spectroscopy was used as a tool to obtain elemental information from the particles. By focusing the electron beam to a small area full of particles, an energy spectrum is obtained with the distribution of elements coming from the grid and sample. The microscope was loaded with a field emission gun (FEG) and used at an accelerating voltage of 200kV. Energy dispersive X-Ray (EDX) spectra were obtained for native ferritin and tungsten-iron apoferritin with a Philips FEI CM-200 mounted X-Ray for comparison. The microscope was then put in scanning mode to obtain Scanning Transmission Electron Image.

#### 4.2.6 Electron Energy Loss Spectroscopy

Electron Energy Loss Spectroscopy (EELS) was used to obtain elemental analysis and chemical composition of the crystals. EELS provides the ability to obtain elemental and electronic information on the oxygen K-edge and the Iron L-edge. With this technique it is possible to differentiate between crystal structures of iron. Samples were adsorbed on a Holey- copper-carbon grid (provided by the

LeRoy Eyring Center for Solid State Science). The samples were loaded into a TOPCON 002B high-resolution electron microscope running at an accelerating voltage of 200kV, and with a 10° double-tilt specimen holder.

#### 4.2.7 Selected Area Electron Diffraction

Samples were adsorbed on a holey-copper grid and loaded in a JEOLARM200F aberration corrected scanning transmission electron microscope. The scope was set to diffraction mode and the diffraction patterns were compared to that of a silicon standard at the same camera length to obtain the respective d-spacings.

#### 4.2.8 X-Ray Diffraction

Samples were first frozen to -80°C overnight, then lyophilized for 24 hours or until dry. Once dry, the powder was dispersed on a zero background holder with 1mm cavity and held together by applying pressure on the powder sample. The holder was loaded on a SIEMENS D5000 powder X-Ray Diffractometer with a fixed horizontal stage. X-Ray radiation was emitted by a CuK $\alpha$ 1 source. The range for diffraction detection was run from 2 $\theta$  values of approximately 10° to 95°. The data was then plotted and indexed with a DIFFRAC Plus measurement software with EVA evaluation software.

#### 4.2.9 Superconducting Quantum Interference Device Magnetometry

Samples were freeze-dried using a lyophilizer after freezing at -80°C overnight. Each sample was weighed before measurements. The sample was loaded into a SQUID magnetometer sample holder. A Quantum Design MPMS-

5S Superconducting Quantum Interference Device (SQUID) was used for all measurements. Hysteresis curves were obtained at 5K from +30000Oe to -30000Oe. Zero field cooled measurements were obtained by first cooling the sample from room temperature to 2K at zero field. Once the temperature stabilized, a small field of 200Oe was turned on and magnetization measurements were collected upon warm up. Similarly field cooled measurements were performed by cooling the sample to 2K with an on-field of 200Oe and measurements were collected during warm up. Temperature dependent reversal curves were performed at 5K, 10K, 50K, and 150K and the slope of the linear reversals were obtained for further magnetic susceptibility calculations, effective magnetic moment and curie constant calculations ( $T_c$ ).  $\mu_{\text{eff}}$  was obtained with the formula.  $\mu_{\text{eff}} = 2.82\sqrt{C_m} \mu_B$ .

#### 4.2.10 *In Vitro* and *In Vivo* MRI

*In vitro* relaxometry measurements at 7T were obtained from a  $T_1$  map of a 1% agarose phantom at different concentrations and with a  $T_1$ -map RARE pulse sequence, TE/TR = 10.88ms/233.3ms, 500ms, 1200ms, 2500ms, 5000ms, NEX 1 and heated to  $\sim 37^\circ\text{C}$  using a water-bath-heated blanket.

All *in vivo* animal experiments were approved by the Arizona State University Institutional Animal Care and Use committee. Adult Sprague Dawley rats were anesthetized with a Ketamine - Xylazine cocktail (90mg/kg and 5mg/kg, respectively) and secured to a stereotactic frame (David Kopf Instruments, Tujunga, CA). The particles were injected into the striatum of a rat in the caudate/putamen, 1.6mm anterior and 3mm lateral from the bregma. To breach the skull, I created two burr holes in the skull bilaterally at the stereotactic

coordinates using a drill. A 10 $\mu$ L Hamilton syringe needle (Sigma Aldrich, St. Louis) was inserted 6mm below the dura. The needle remained in place for 1 minute and then was retracted to 5mm below the dura. 8 $\mu$ L of WFe and control (native ferritin) were injected over the span of 5 minutes into the left and right hemispheres, respectively. The rat was imaged on a Bruker 7T/30 scanner (three-axis gradient, slew rate of 150 T/m/s) using a rat surface RF coil. Isoflurane gas and oxygen were delivered during the scan. To image the striatum, a fast low-angle shot pulse sequence (FLASH) was used (TE/TR= 3.8ms/55.9ms, NEX 4), and a T<sub>1</sub>-map RARE pulse sequence, TE/TR = 10.88ms/233.3ms, 500ms, 1200ms, 2500ms, 5000ms, NEX 1. The T<sub>1</sub> map was color coded and overlaid onto a T<sub>1</sub>-weighted scan for reference. The overlay was set to 50% transparency using Adobe Illustrator software.

## 4.3 Results and Discussion

### 4.3.1 Synthesis and Nanoparticle Characterization

To create the paramagnetic WFe composite, an iron oxide core was formed in apoferritin, as previously described (Jordan, et al.), by filling apoferritin with iron using the intrinsic ferritin ferroxidase. Then, both tungsten and iron were incorporated iron into the apoferritin core at the same time. After synthesis, dialysis, and purification, the ferritin nanoparticle core comprised an electron-dense metal crystal about 6nm in diameter, as demonstrated with transmission electron microscopy (TEM, Figure 24a). The WFe-apoferritin yield was 10%, which is about 5 times more than that of magnetoferritin.

The distribution of the WFe-apoferritin particle sizes, monodispersity, and stability were characterized with size exclusion chromatography (SEC) and

native gel electrophoresis as seen in Figure 22. The WFe-apoferritin particles were monodisperse and stable after weeks of storage Figure 22b, making them practical for *in vivo* imaging experiments.

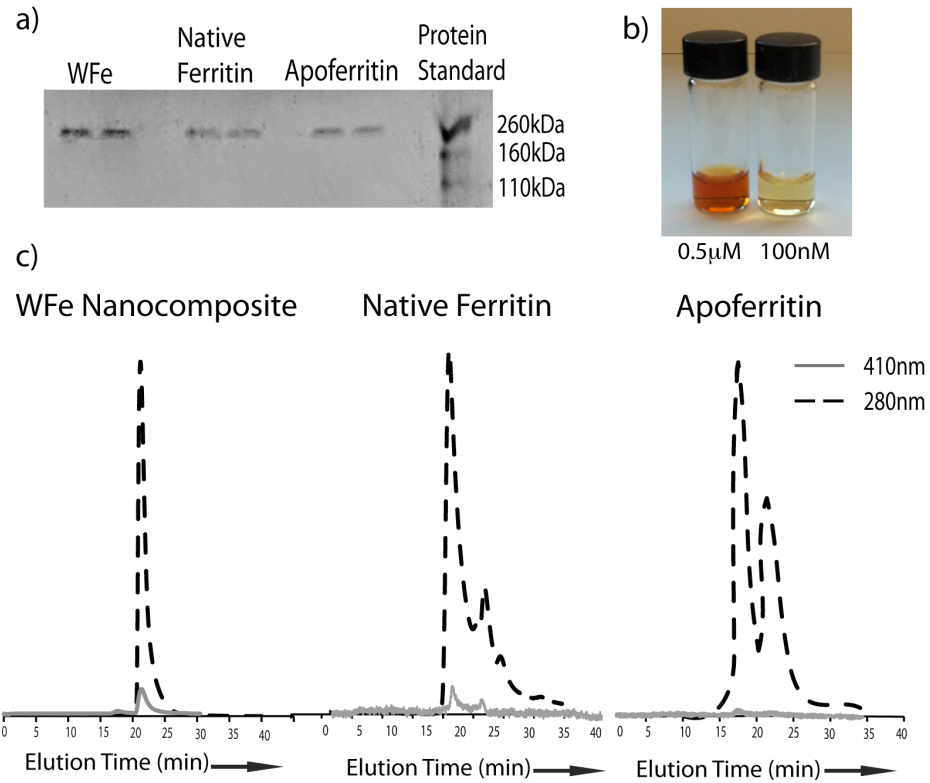


Figure 22. a) Native tris-glycine gel electrophoresis showing that similar molecular weight for the composite, native ferritin and apoferritin. b) Photograph showing concentrated WFe particle solution (left) and solution after purification (Shaw, et al.). c) Size exclusion chromatography (SEC) of WFe nanocomposite, Native Ferritin, and Apoferritin, showing same elution time before, and after mineralization.

The elution peaks were monitored by measuring absorbance of protein (280nm) and iron (510nm) as the particle solution traversed through the exclusion column. The presence of both iron and protein peaks (gray line and black dotted line respectively) at the same elution time indicate that the mineralization process and that the purification process were successful and that any non-specific oxidation outside the protein was discarded. The elution time peak for the WFe-apoferritin composite at ~20 minutes correlate with the elution time for native ferritin and apoferritin. These results suggest that the WFe-apoferritin nanoparticle is comparable to off-the-shelf native ferritin and apoferritin in monodispersity. The peaks obtained at ~25 minutes indicate that those are larger molecules taking longer to traverse through the column. This could be attributed to the presence of apoferritins and ferritins with a higher ratio of Heavy to light chain peptides. Also, possible dimers or trimers could be found when the protein is in its native form.

#### 4.3.2 Crystal Structure Characterization

The metal cores of the WFe nanoparticles were homogeneously filled (Figure 23a). There were no visible lattice fringes in high-resolution electron microscopy (HREM, Figure 23b). The Fourier transform of the HREM image of the particle, shown in the inset of Figure 23b, contained no diffraction spots, indicating the absence of a crystalline lattice. In contrast, the Fourier transform of the HREM image of native ferritin contained diffraction peaks consistent with a magnetite/maghemite crystal with a lattice spacing of ~ 0.25nm (see supporting information). The WFe-apoferritin nanoparticles were visible in scanning transmission electron microscopy (STEM), as shown in Figure 23c. Based on the

energy dispersive spectrum (EDS) across the particle, the core diameter was ~7 nm, consistent with the inner diameter of apoferritin. Line profiles of the EDS signal, shown in Figure 23c, indicated that tungsten and iron were both evenly distributed in the core, suggesting that both metals were incorporated evenly into the crystal lattice. WFe nanoparticles exhibited no X-ray diffraction patterns, (Figure 23d, bottom panel), confirming that cores of the WFe nanoparticles were amorphous. In contrast, the cores of native ferritin exhibited the characteristic peaks of magnetite/maghemite, (Figure 23d, top panel). WFe nanoparticles exhibited no distinct d-spacings in selected area electron diffraction (SAED), while native ferritin exhibited the characteristic d-spacings for magnetite/maghemite of 0.25nm, 0.205nm, 0.154nm, and 0.130nm. There were approximately  $8788 \pm 3272$  metal atoms ( $8743 \pm 3277$  iron and  $77 \pm 55$  tungsten) inside each nanoparticle, measured by inductively-coupled plasma-optical emission spectroscopy (ICP-OES). These data confirmed that an amorphous tungsten-doped nanoparticle had formed inside the apoferritin protein.

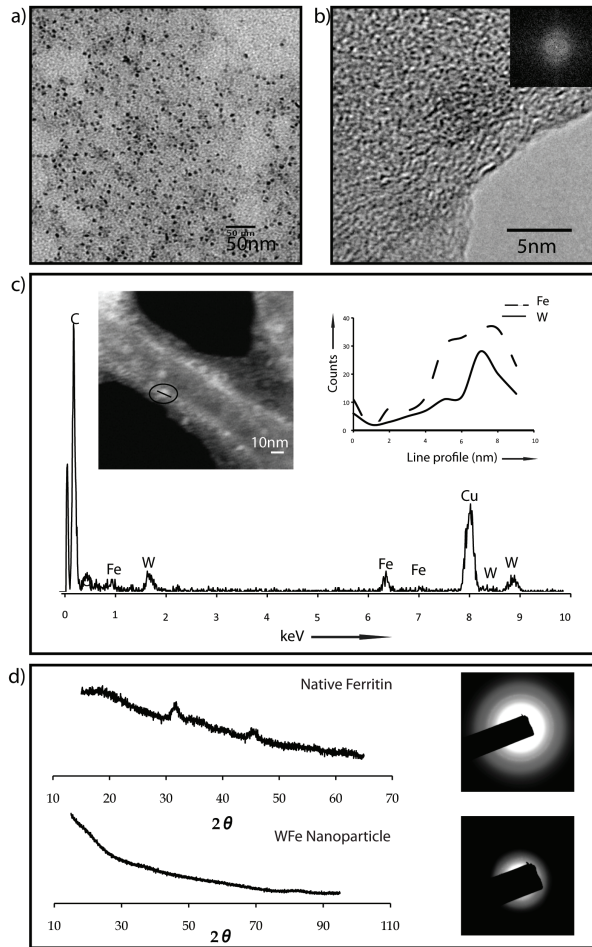


Figure 23. a) Transmission electron microscopy (Artemov, et al.) of WFe composite cores showing ~ 6-8nm cores. b) High resolution electron microscopy (HREM) of a WFe nanoparticle and FFT pattern inset. c) Energy Dispersive Spectrum (EDS) of a selected region of the WFe apoferritin. Insets: Scanning Transmission Electron Microscopy (STEM). Line profile indicates a ~3-4nm core with both W and Fe. d) X-Ray Diffraction (XRD) peaks native ferritin (top spectrum), and WFe nanoparticle (bottom spectrum). Selected area electron diffraction (SAED) of WFe (bottom panel). Native ferritin had several diffraction rings with d-spacings consistent with magnetite/maghemite (top panel).

Electron energy loss spectroscopy was performed on native ferritin and the WFe-apoferritin nanoparticles to obtain the oxygen to iron ratios for each sample. Analyzing the signal ( $S_i$ ) for each edge after background subtraction can provide quantitative elemental information. This is due to the fact that the energy loss is proportional to the number of atoms giving rise to it. Colliex C et al., outlined a method to determine concentration-ratios based on the signal at the high energy Oxygen K-edge and Iron  $L_{2,3}$  edge (Colliex, Manoubi, & Ortiz, 1991). Firstly, the background signal was subtracted by a power-law model  $AE^{-r}$  (figure 24) Secondly, an integration area long enough to cover the L edge and the O edge in its entirety was selected ( $\Delta$ ). Finally, the integrated signal was substituted into the following equation.

$$\frac{N_{Fe}}{N_O} = \frac{S_{Fe}(\alpha, \Delta) \sigma_O(\alpha, \Delta)}{S_O(\alpha, \Delta) \sigma_{Fe}(\alpha, \Delta)} \quad \text{Eqn 21}$$

Using the Hartree-Slater values for the cross sections  $\frac{\sigma_O(\alpha, \Delta)}{\sigma_{Fe}(\alpha, \Delta)}$ , and with a

$\Delta = 50\text{eV}$ . The ratios  $\frac{N_{Fe}}{N_O}$  found for the particles are the following.

Table 6  
*EELS Atomic Ratios for WFe-Apoferritin Cores*

	$\frac{S_{Fe}(\alpha, \Delta)}{S_O(\alpha, \Delta)}$	$\frac{\sigma_O(\alpha, \Delta)}{\sigma_{Fe}(\alpha, \Delta)}$	$\frac{N_{Fe}}{N_O}$
Native Ferritin	0.62	0.676	0.418
WFe-Apoferritin	0.3918	0.676	0.265

EELS Iron to oxygen ratios to determine stoichiometries. Hartree-Slater values for the O-Fe cross-sections were obtained from Hofer at al. (Hofer, 1991)

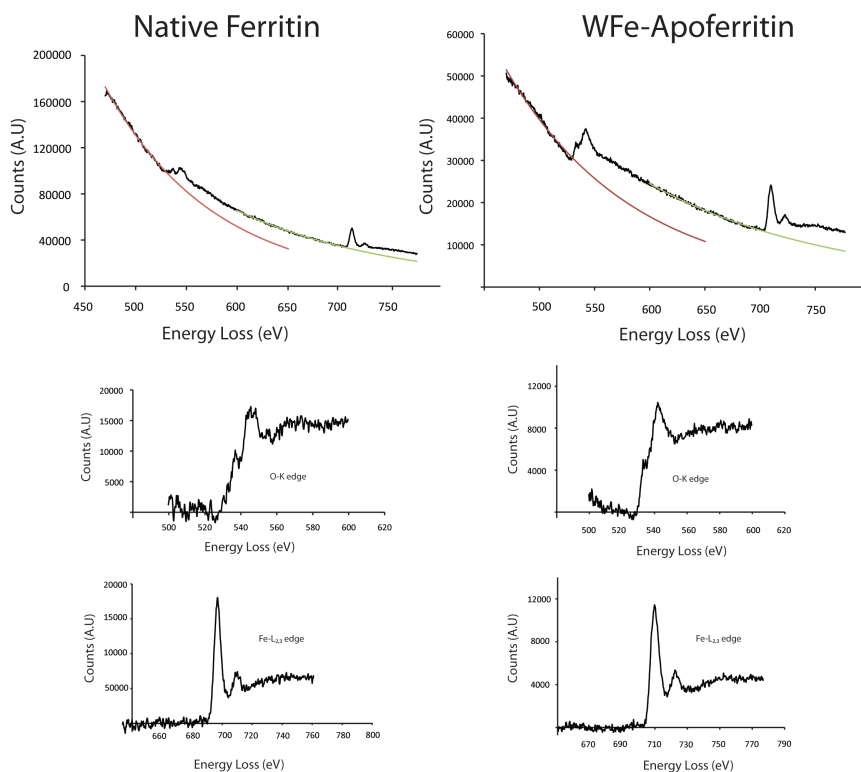


Figure 24. Complete Electron Energy Loss spectra of Native Ferritin and the WFe-apoferritin particles. Bottom panels display the respective O-K edge and the Fe L<sub>2,3</sub> for Native Ferritin and WFe-Apoferritin nanoparticles. O K-edge and Fe-L<sub>2,3</sub> spectra were corrected by subtracting the delineated background lines (red and green respectively)

Using the atomic ratios obtained in table 6, the sample formula unit can be inferred. For the WFe-apoferritin it is clear that there is 3.77 times more oxygen atoms than iron, suggesting a formula in the following stoichiometry Fe<sub>x</sub>W<sub>y</sub>O<sub>4x</sub>. On the other hand, native ferritin calculations showed different ratios; there is 2.39 times more oxygen than iron in the formula unit of the crystal core.

The reported formula for the ferrihydrite core in native ferritin is  $[\text{FeO}(\text{OH})]_8[\text{FeO}(\text{H}_2\text{PO}_4)]$ . With a  $N_{\text{O}}$  to  $N_{\text{Fe}}$  ratio of approximately 2.33, which is in agreement with the EELS data.

#### 4.3.3 Magnetic Properties and Relaxivity

To determine whether tungsten doping made the nanoparticle paramagnetic, magnetometry was performed using a superconducting quantum interference device (SQUID). Figure 25 shows the SQUID magnetization curves at 5K. The WFe nanoparticles exhibited increasing magnetization with applied field (up to 3T), almost no saturation, and showed no hysteresis, all characteristic of paramagnetism. In contrast, native ferritin exhibited saturation at  $\pm 20000\text{Oe}$  and hysteresis, characteristic of superparamagnetism below the blocking temperature, in this case, 5K. The effective paramagnetic moment of the WFe particle was  $\sim 63\mu_{\text{B}}$  based on temperature-varied measurements of magnetization reversals.

Since the calculations were performed based on molar susceptibility measurements,  $63\mu_{\text{B}}$  is the per-apoferritin particle moment. Thus, since the main paramagnetic moments present within the lattice are those of  $\text{Fe}^{3+}$ , it is possible to obtain the number of paramagnetic atomic elements by dividing the total moment by  $5\mu_{\text{B}}$  ( $\text{Fe}^{3+}$  moment). This calculation results in a total of 12.6 paramagnetic atoms. Given that the particle  $T_1$  relaxivity was  $4870\text{mM}^{-1}\text{s}^{-1}$ , it is possible to determine the per-paramagnetic-atom  $T_1$  relaxivity. This calculation then results in a per- $\text{Fe}^{3+}$  relaxivity of  $\sim 386\text{mM}^{-1}\text{s}^{-1}$

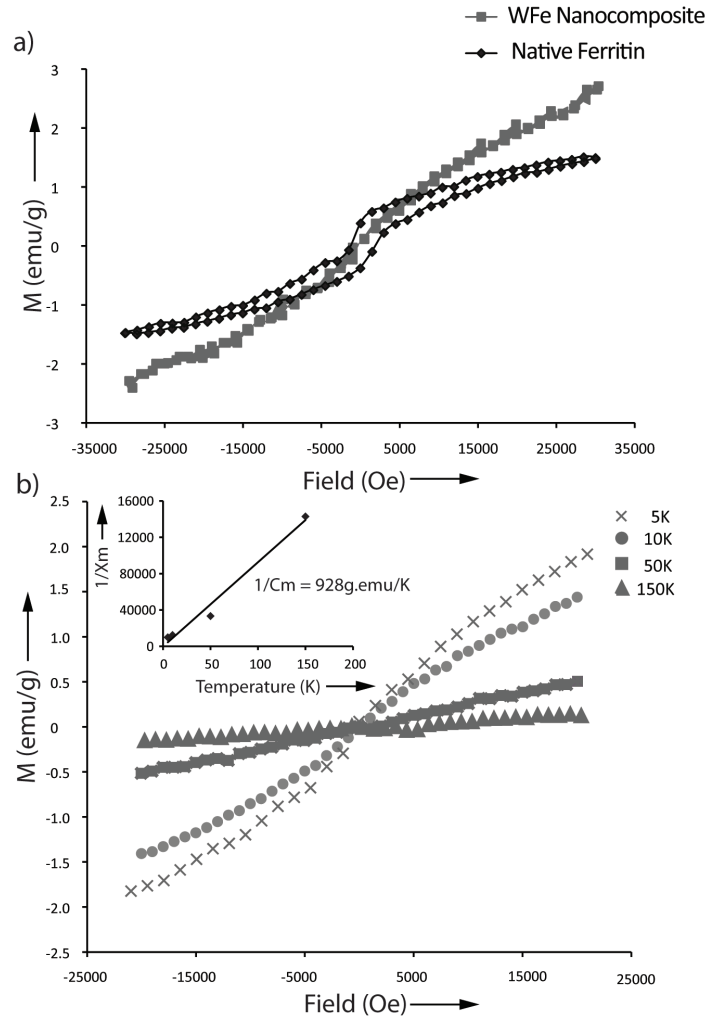


Figure 25. Superconducting Quantum Interference Device (SQUID) magnetometry for WFe-apoferritin nanoparticles. a) SQUID reversal curves for WFe nanoparticles and native ferritin at 5K showing paramagnetism in WFe nanoparticles and superparamagnetism in native ferritin. b) Temperature dependent magnetization reversals were performed at 5K, 10K, 50K, and 150K.

The slope of the curve as a function of temperature was measured to calculate the magnetic susceptibility and the Curie constant. The WFe nanoparticles were paramagnetic at different temperatures and exhibited curie-

weiss paramagnetic behavior. From equation 12 the magnetic curie-weiss susceptibility is characterized by a shift along the temperature axis, thus the presence of the curie-weiss temperature “ $\theta$ ”. In the case of the WFe composite, this temperature corresponds to the point where the linear fit in figure 26 intercepts the abscissa. This indicates that there is an exchange interaction between magnetic moments between atoms in the crystal in addition to an interaction with the external magnetic field. The positive value of  $\theta$  suggests that the inter-atomic interaction is ferromagnetic, aligning nearest magnetic moments along the same directions.

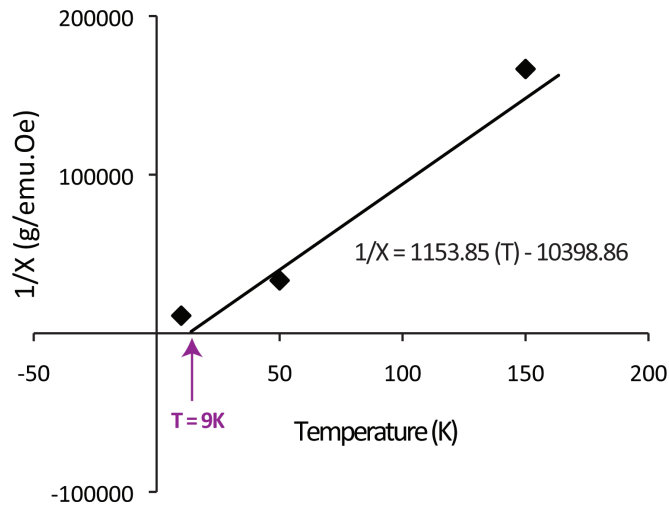


Figure 26. Linear fit of  $1/X$  obtained from temperature dependent magnetization reversals. Only the linear portion of the curves was used for the susceptibility calculations.

Field cooled (FC) and zero field cooled (ZFC) magnetization measurements are a good way to determine the intrinsic magnetic characteristics of a material. Here, FC and ZFC on the tungsten-iron apoferritin and on ferritin in

its native form was performed. The results indicated that the paramagnetic WFe nanoparticles had a reduced blocking temperature ( $\sim 3.5\text{K}$ ) compared to that of native ferritin ( $\sim 13\text{K}$ ). (Figure 27 ZFC). Previous ZFC and FC studies on native ferritin have shown a blocking temperature in agreement to what was found here, however, the thermal behavior when cooled at 200Oe was unusual showing a larger gap between the FC and the ZFC curve. This could be due to aggregation of the particles or a large number of magnetite ferritin particles in the sample.

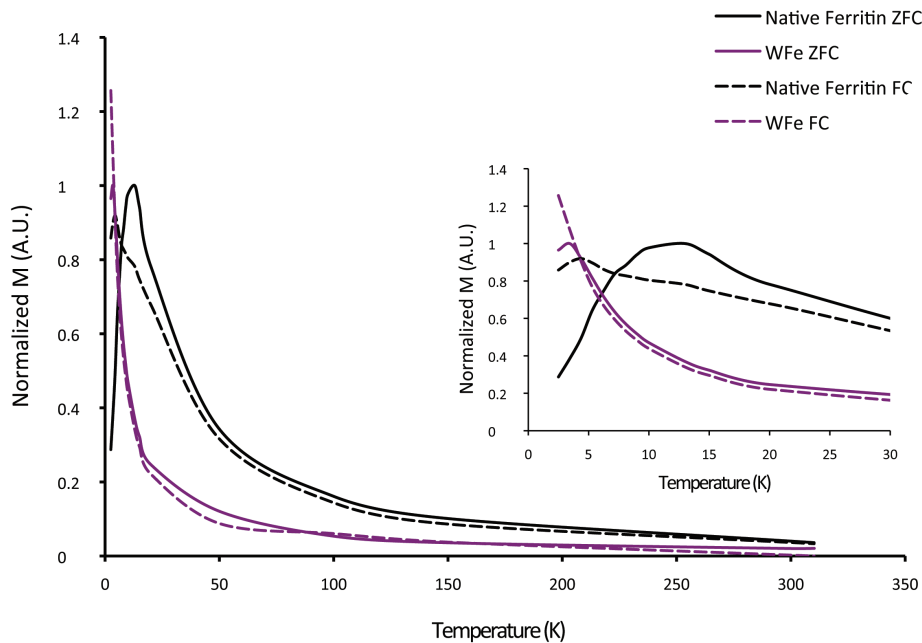


Figure 27. Zero field cooled (ZFC) and field cooled (FC) experiments for WFe nanoparticle and native ferritin. The WFe nanoparticles had an approximate  $T_b$  of 3K while native ferritin had a  $T_b$  of approximately 13K.

These results are in agreement with the formation of a disordered and amorphous spin-glass like crystal. Shaw et al investigated the magnetic characteristics of antiferromagnetic spin glass-like iron phosphates (Shaw, et al., 2004). The introduction of phosphates to coordinate to the iron atoms create a

direct linkage between phosphorous and iron bridged by oxygen. Fe-O-P. These amorphous materials show almost identical ZFC and FC data than the WFe apoferritin nanoparticle. These spin glass-like iron phosphate materials had susceptibility data that suggested that their paramagnetism was of curie-weiss type. With a Néel temperature around -80K suggesting antiferromagnetic coupling below the blocking temperature. Due to the antiferromagnetic spin-glass behavior in these iron-phosphate glasses, the FC curve shows a magnetization that is constant regardless of the reduction of thermal energy below the blocking temperature. This confirms the ferromagnetic spin coupling found below the blocking temperature for the WFe apoferritin composite. The FC curve illustrates an increase in magnetization as the thermal energy is decreased below the blocking temperature, which is in agreement of ferromagnetic spin coupling.

Taken together, the magnetization measurements confirmed that the WFe-apoferritin nanoparticles were paramagnetic at temperatures higher than 3K. Also, the composite showed curie-weiss behavior similar to amorphous spin-glasses.

Barbosa et al. investigated the incorporation of heteropolytungstates as ligands for coordination with  $\text{Eu}^{3+}$  lanthanides. Previous work of theirs had shown that polyphosphate ligands coordinated to  $\text{Eu}^{3+}$  resulted in stable strong complexing agents with powerful luminescent characteristics (Barbosa, et al., 2010). With the premise that the ligand field can affect the spectrochemical emission due to energy absorption, this group studied the substitution of tungstate ligands instead of the polyphosphate chains. Their results showed nanoparticles of comparable size to the WFe-apoferritin crystals and with surprisingly high  $^5\text{D}_0$  emission quantum efficiencies due to the strong ligand field

provided by the tungstates. This gives tremendous insight in the mechanism of action of the tungsten-doped iron oxide crystals. If similar to Barbosa et al, tungstate ligands in the WFe apoferritin crystals could be complexing the  $\text{Fe}^{3+}$  or  $\text{Fe}^{2+}$  atoms present within the lattice. Since tungstate imparts a strong ligand field, the complexed metal atoms would then be forced to have large orbital splittings and therefore be in a low spin state.

With this theory in mind,  $\text{Fe}^{2+}$  a  $d^6$  bare metal electronic configuration would then be diamagnetic in its low spin state having no unpaired electrons to exchange and no magnetic moment. On the other hand,  $\text{Fe}^{3+}$  a  $d^5$  bare metal electronic configuration, would then be paramagnetic with only one unpaired electron in its lowest energy orbital. Therefore, the magnetic moment  $1\mu_B$  for  $\text{Fe}^{3+}$  would most likely remain decoupled and thus the overall oxide would result in an amorphous paramagnetic crystal.

#### 4.3.4 *In vitro* Phantom and *In vivo* MRI

To confirm that the WFe nanoparticles are detectable *in vivo* with  $T_1$ -weighted MRI, I injected 8ul of 195nM nanoparticles into the caudate/putamen of adult Sprague Dawley rat brains and the same volume of native ferritin in the contralateral side as a control. Figure 28b shows a typical *in vivo*  $T_1$ -weighted gradient-echo MRI (TE/TR=3.8ms/55.9ms) of the brain after injection, acquired at 7T. The injection site for the WFe nanoparticles was hyperintense (left side of the brain). Native ferritin was not detected (right side of the brain). The  $T_1$  was 22% shorter at the site of WFe injection (2.02 s) than at the contralateral site of native ferritin (2.61 s), as shown in Figure 29c. Based on the measured  $r_1$  of WFe nanoparticles of  $2200\text{mM}^{-1}\text{s}^{-1}$  at 7T (Figure 28a), I estimated that  $\sim 50\text{nM}$  was

detected *in vivo*. Thus, WFe nanoparticles are useful as passive (un-targeted) agents with  $T_1$ -weighted MRI at concentrations in 10s of nanomolar at 7T.

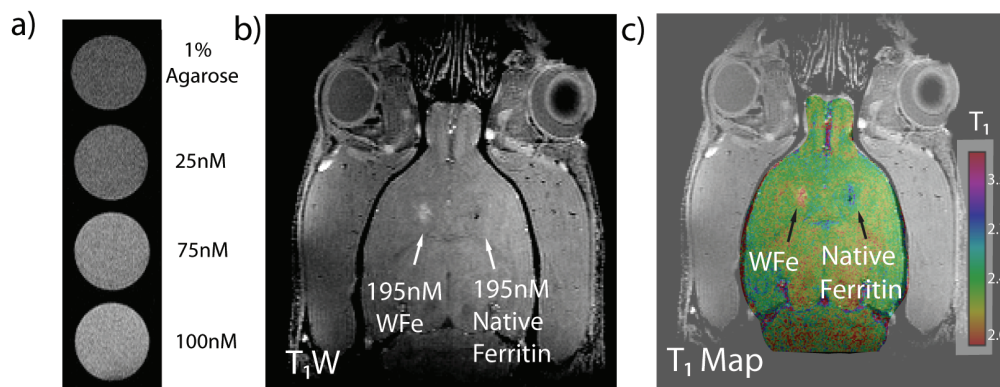


Figure 28. WFe nanoparticles are detected *in vivo* with  $T_1$ -weighted MRI. a) 2D Gradient Echo  $T_1$ -weighted image of a 1% agarose phantom. Increasing concentrations of WFe-apoferritin result in increased positive image contrast. b) 3D Gradient Echo  $T_1$ -weighted image of an *in vivo* inoculation of 8ul of 195nM WFe nanoparticles and native ferritin into a rat striatum. Images were acquired on a 7T Bruker small animal scanner. c)  $T_1$  map color overlay showing an average  $T_1$  for each ROI at the injection sites. The injection of WFe nanoparticle had an average  $T_1$  22% shorter than the contra lateral ROI.

#### 4.4 Conclusions

Chemical doping is used to create an amorphous WFe nanoparticle with high  $T_1$  relaxivity. To my knowledge this is the first report of a tungsten-doped iron oxide to form an MRI contrast agent. Tungstate ligands disrupted the exchange coupling between spins to reduce  $r_2$  and consequently reduce  $r_2/r_1$ .

WFe-apoferritin nanoparticles were detected in the brain *in vivo* in ~10s-100s of nM concentrations with conventional T<sub>1</sub>-weighted MRI.

## CHAPTER 5

### *IN VIVO* DETECTION OF TARGETED WFE APOFERRITIN NANOPARTICLES AND *IN VITRO* TOXICITY

#### 5.1 Introduction

The tungsten-iron apoferritin nanoparticles proved to be highly sensitive *in vivo*. Their increased  $r_1$  and reduced  $r_2$  allowed for sensitive detection of a bolus injection directly into the brain and imaged at 7T in a living rat. However, in order to prove their functionality as targeting agents the agent needs to be functionalized and targeted against a specific marker. Nanoparticle  $T_1$ -shortening contrast agents are usually tested *in vivo* as passive targeting agents, namely targeting accumulation in tumors via leaky vasculature or as blood pool agents ((B. H. Kim, et al., 2011; Na, et al., 2007; W. S. Seo, et al., 2006), delivery and targeting to specific markers has been shown in very few instances (Geninatti Crich, et al., 2006; Kalman, Geninatti-Crich, & Aime, 2010). Aime et al loaded the empty cavity of apoferritin with Gd-HP-DO3A (Prohance) and also with approximately 1000  $Mn^{2+}$  ions, functionalized the surface of the protein with targeting moieties to target angiogenesis of grafted tumors in mice and also to target hepatocarcinomas *in vivo*, these are some of the few examples of active targeted  $T_1$ -shortening nanoparticles. Here, the surface of the apoferritin loaded with the tungsten-iron composite was cationized in order to label charged membranes in the kidney glomerular basement membrane. The small size of the particle allows the passage through fenestrated endothelia and thus the sensitive detection of markers and membranes *in vivo* without the concern of blood background. Finally, cellular toxicity of the composite agent is evaluated herein.

## 5.2 Methods

### 5.2.1 Synthesis of Cationized Tungsten-Iron Nanoparticle “ParaCF”

Ferritin is readily cationized using a carbodiimide method outlined in Danon et al. The same method is used here to cationize the surface of the WFe ferritin nanoparticles, rendering what is referred to as paraCF. Once cationized, the resultant paraCF was dialyzed two times against phosphate buffered saline (PBS).

### 5.2.2 Intravenous Injection of ParaCF in Adult Rats

All animal experiments were approved by the Arizona State University Institutional Animal Care and Use committee. Adult Sprague Dawley rats were anesthetized with a Ketamine - Xylazine cocktail (90mg/kg and 5mg/kg, respectively). A single bolus injection of 11 mg paraCF in 1 ml PBS was administered intravenously in 3 male sprague-dawley rats and imaged in at small animal 7T Bruker scanner 1.5h after injection.

### 5.2.3 *In vivo* Detection of Kidney Glomeruli, liver and spleen with MRI

The paraCF-injected rat was imaged 1.5 hr after injection using a  $T_1$ -weighted 2D gradient recalled echo (GRE) MRI pulse sequence (TE/TR = 10/54, field of view = 3x3 cm, matrix size = 256x256, slice thickness = 400  $\mu$ m). A naïve, un-injected rat was imaged using the same MRI pulse sequence and parameters. ParaCF labeling of the kidney glomerulus was quantified by normalizing the signal magnitude of the renal cortex to the muscle surrounding the spine (which is assumed to remain unlabeled by paraCF). The same normalization process was performed in the control rat.

The ability to image the kidney and spleen was only attained with the fabrication of a custom made surface coil. To optimize the volume coverage and depth penetration for the *in vivo* rat kidney scans a surface coil was designed with a diameter of 4.25cm, and 2.5cm depth penetration with number of loops in the coil of 5 ( $N_{\text{coil}} = 5$ ). The surface coil was made from magnet grade wire (Belden, St. Louis, MO), bread-board, and non-magnetic passive trimmers (Johanson, Boonton, NJ and ATC, Huntington Station, NY). All passive components were defined to be able to tune and match directly on the resonator within the magnetic field and account for the impedance shift of the sample prior to all *in vivo* measurements. Subsequently, the coil was connected to a 7T magnet via the Avance III RF Interface Adapter T12325 (Bruker, Billerica, MA) and placed on the abdomen of the rats.

#### 5.2.4 Immunohistochemistry

Following imaging of the live rats, the animal was perfused and the kidneys were extracted and fixed. Following dehydration and section, the kidney was stained with DAPI to visualize cell nuclei. Ferritin was labeled with a rabbit anti-ferritin antibody and with a secondary antibody labeled with Alexa594 against rabbit IgG. The immunostained sections were then imaged using a Confocal microscope.

#### 5.2.5 Cytotoxicity of WFe-Apoferritin Nanoparticles

A live/dead assay was performed following the instructions in the kit provided by the manufacturer (Biotium, Inc. Hayward, CA). Briefly, 20,000 3T3 cells were seeded onto 24-well plates and cultured for 1 day. The cell culture

media supplemented per the suggested growth of 3T3 NIH cells. The cocktail was made up of the following. Dulbecco's Modified Eagle Medium /+L-glutamine, 10% Bovine Serum, and 2% Penicillin/Streptomycin. The cells were then treated with 0nM (DPBS), 3nM, 17nM, 33nM, or 700nM of WFe nanocomposite. The Calcein AM and EthD-III dyes were added to a cell-PBS mixture and let react for 30 minutes. After such time, the fluorescence of calcein (530nm emission) and EthD-III (645nm emission) were obtained with an inverted fluorescence microscope. The live/dead percentages were obtained by means of a trypan blue stain. Briefly, 50 $\mu$ l of 0.4% Trypan blue solution was added to 50 $\mu$ l of the cell suspension prior to counting with a hemacytometer. Stained cells were counted as dead and accounted in the live/dead percentage calculations.

## 5.3 Results and Discussion

### 5.3.1 *In vivo* Detection of Kidney Glomeruli with T<sub>1</sub>-weighting

To confirm that WFe-apoferritin nanoparticles could also be used as targeted contrast agents, the surface was functionalized with amine groups to create a paramagnetic form of cationized ferritin ("paraCF"). Cationized ferritin (Figueiredo, Moreira, & Geraldés) is an example of a targeted, superparamagnetic contrast agent to detect and count individual glomeruli in the kidney with MRI (Beeman, Zhang, et al.; Bennett, Zhou, et al., 2008). CF also readily binds to the extracellular matrix of other organs containing fenestrated endothelia. However, CF is superparamagnetic and is therefore difficult to detect against the blood background *in vivo*. Also, due to its higher T<sub>1</sub> relaxivity, ParaCF may be more readily detected in non-toxic doses. To test this, cationized WFe-apoferritin was used using published methods (Danon, Goldstein, Marikovsky, &

Skutelsky, 1972) and injected it intravenously in rats. There was significant enhancement in *in vivo* MRI (Figure 29a) in the kidney and spleen compared to the naïve controls (Figure 29b). The image was normalized to the magnitude of surrounding muscle and set a threshold of 50% to map WFe-enhancement (Figure 29c). The labeled kidney cortex had punctate hyperintense areas, consistent in distribution with recent *ex vivo* results using CF. (Beeman, Georges, & Bennett, 2012) Images of control kidneys with no injections had no hyperintense spots (Figure 29d).

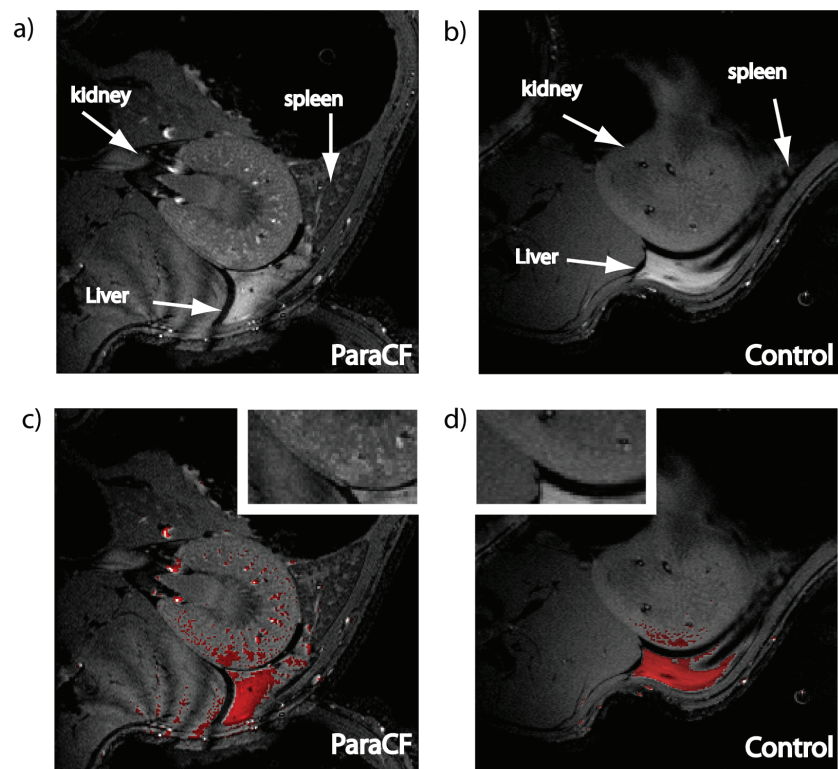


Figure 29. a) *In vivo* intravenous injection of paraCF labeling kidney glomeruli. b) Control image of a rat *in vivo* with no injection of agent. c) Thresholded image of paraCF labeled and, d) no injection of agent. Highlighted in red are pixels with intensities 50% higher than background muscle tissue, insets show cortex of paraCF kidney and control kidney.

It is clear that the glomeruli are labeled with paraCF showing evident hyperintensities in the cortex of the kidney, while control did not show significant enhancement over background.

### 5.3.2 Immunohistochemistry

Kidneys labeled with paraCF were then isolated after perfusing the animal; the kidney sections were then labeled with DAPI and anti-horse spleen ferritin antibody with a rabbit anti-ferritin antibody followed by a goat anti-rabbit IgG secondary antibody labeled with Alexa594. Figure 30 below illustrates the clear labeling of paraCf around the glomerulus. Native ferritin, on the other hand, did not accumulate in the charged membrane.

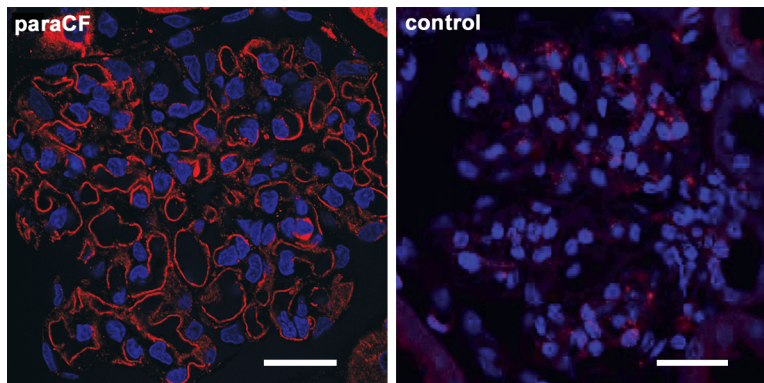


Figure 30. IHC of paraCF labeled glomerulus (left) and native ferritin control on the right. Ferritin immuno-stain in red is present only on in the paraCF labeled kidneys. Scale bars 20 $\mu$ m.

This result confirms that the punctate hyperintensities found in the *in vivo* MRI images are indeed the result of the paramagnetic version of cationized ferritin, “para CF”.

### 5.3.3 Cell Viability and Toxicity

Toxicity is important to the utility of any novel agent. To investigate the toxicity that the WFe-apoferritin nanoparticles may elicit to cells, adherent 3T3 fibroblasts were incubated with 0 to 700nM of WFe apoferritin for 24 hours. And the viability of cells after such exposure was quantified.

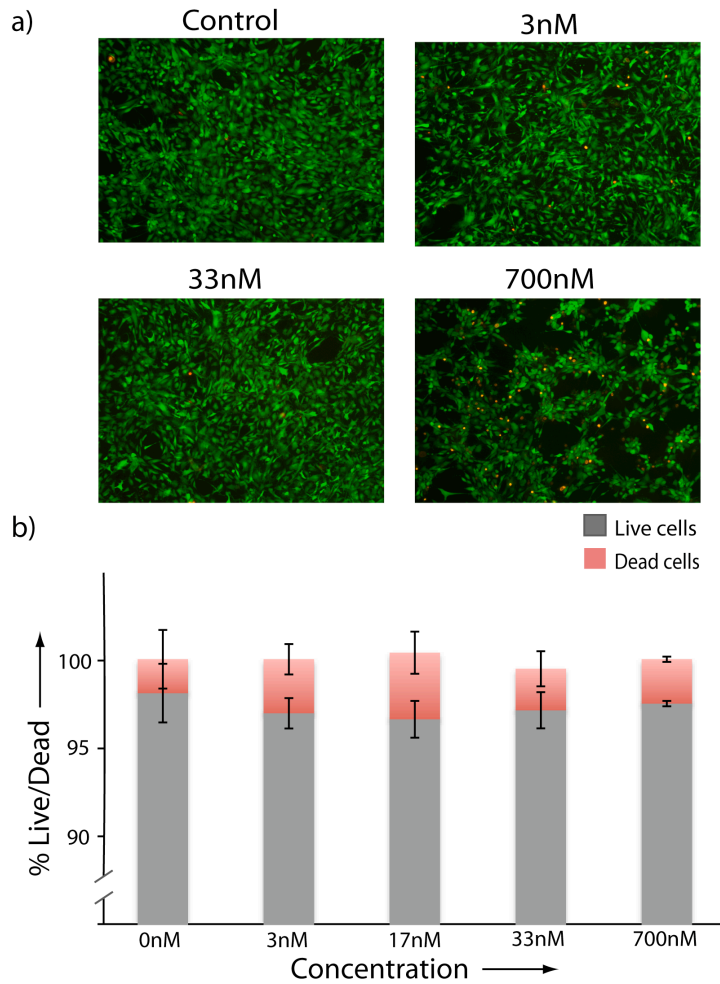


Figure 31. WFe nanoparticles are non-toxic in MRI-detectable concentrations. a) Fluorescence image of 3T3 fibroblasts incubated with WFe for 24h. Live cells are labeled with calcein (green) and dead cells are labeled with EthD-III (Figueiredo, et al.) b) Viability and cytotoxicity quantitative results

indicating no significant cell toxicity for particle concentrations lower than 700nM. Error bars indicate the standard error of the mean (n=3).

Cells were ~97% viable after exposure to nanoparticle concentrations lower than 33nM, equivalent to ~0.3mM metal (Figure 31). Cells exposed to concentrations above 700nM of nanoparticles were 93% viable. Therefore, the WFe nanoparticles are relatively non-toxic to cells in particle concentrations ranging from 3-700nM. These results come as no surprise, since ferritin has been known to be a relatively inert natural nanoparticle in the body (Cormode, et al., 2009). Also, cationized ferritin has been shown to be neither nephrotoxic nor hepatotoxic when injected intravenously in MRI-detectable concentrations (Beeman, et al., 2012).

Higher particle concentrations (>700nM) may be appropriate to investigate the LD<sub>50</sub> of the particles. However, such concentrations would not be representative of target concentrations *in vivo* as most targets are found in nanomolar to picomolar concentrations.

#### 5.4 Conclusions

The WFe nanoparticles were readily functionalized and detected in the glomerular basement membrane *in vivo*. The high T<sub>1</sub> relaxivity of the agent allowed for the detection of individual glomerulus *in vivo* without the need of perfusing the animal. To confirm the nature of the signal, immunohistochemistry showed that ferritin was indeed targeted to the charged membrane of the kidney glomerulus. The agent was sensitive and efficient enough to be distinguishable above the blood background of the kidney and spleen. Also, given the

tremendous concern of metal toxicity, cytotoxicity studies performed in mouse fibroblasts after a period of incubation with the apoferritin composite particles showed that they are not toxic at concentrations relevant for molecular imaging *in vivo*.

## CHAPTER 6

### SUMMARY AND FUTURE WORK

#### 6.1 Summary

Magnetic nanomaterials are important for a wide range of clinical and preclinical applications and rely on expertise in the physical, chemical, and biological aspects of both magnetization and material-biological interactions. Novel nanometer-scale magnetic materials, specifically functionalized and engineered for highly sensitive detection with MRI, open the door to tailored diagnostics and targeted therapy. Here, I explored the mechanisms of magnetization manipulation using apoferritin as a nano-reactor. Typical iron oxide nanoparticle contrast agents are composed of a metal oxide core stabilized and coated with a synthetic polymer, which in turn increases the size of the particle significantly. Apoferritin is uniform in size and shape and is small enough (8nm) to traverse through fenestrated endothelia. Apoferritin was loaded with magnetite crystals, adsorbed with  $Mn^{2+}$  ions onto the pores of its surface, and loaded with a tungsten-doped iron oxide crystal. All configurations resulted in distinct magnetic properties; it was found that re-loading the apoferritin cavity with magnetite crystals gave rise to increased  $T_2$  relaxivity and low  $T_1$  relaxivity. Adsorbing  $Mn^{2+}$  ions onto the surface of magnetoferritin resulted in an increased per-metal and per-particle  $r_1$  that has not been reported before. However, since the  $Mn^{2+}$  could not be adsorbed without the simultaneous addition of iron, the particle not only had increased  $r_1$  but also a significantly high  $r_2$ . This  $r_2/r_1$  made it unfeasible for imaging with conventional  $T_1$ -weighting. The addition of tungstate ligands during the growth of iron oxide crystal inside the apoferritin protein resulted in an amorphous crystal with superb  $r_2/r_1$  characteristics. The chemical

doping of the crystal with tungsten destroyed the long-range order within the crystal and prevented electron exchange among neighboring metal atoms. This atom-isolated structure results in decoupled magnetic moments reducing the magnetic anisotropic energy, thus creating a paramagnetic crystal. By decoupling the metal magnetic moments not only was the  $r_1$  significantly increased, but also the  $r_2$  was reduced to levels that allowed the sensitive detection window of 20-400nM with conventional  $T_1$ -weighting pulse sequences *in vivo*. Finally, this newly synthesized and magnetically engineered particle showed excellent *in vivo* targeting characteristics when the cationized version of the particle (ParaCF) was injected intravenously in rats to target the negatively charged basement membrane of the kidney glomeruli. For the first time, individual glomeruli could be imaged *in vivo* with  $T_1$ -weighting. In conclusion, the chemical doping of crystal oxides inside apoferritin may be a novel route towards the rational design of sensitive endogenous nanoparticle based  $T_1$  shortening contrast agents for molecular MRI.

## 6.2 Future Work

### 6.2.1 Adding Color to MRI with Doped Iron Oxide Crystals Inside Apoferritin

In molecular therapeutic and diagnostic research the most accurate methods to obtain molecular information from tissues is via ex-vivo histology. The level of resolution and specificity is greatly increased compared to Positron Emission Tomography (Medarova, et al.), Computed Tomography (CT) or MRI due to the use of sensitive antibody-bound fluorophores, genetically modified fluorescent proteins such as GFP, YFP, RFP, etc., and high resolution light microscopy. Although extremely specific and sensitive, their detection is only

achievable after biopsy or via a light endoscope. External molecular probes, such as quantum dots, have been developed with different wavelength emissions by varying their inorganic metallic core size. These sets of potentially specific and small probes are, however, composed of toxic metallic materials and their detection is limited by light penetration through tissue. Thus, there is an increasingly growing need to obtain similar kind of histological information *in vivo*, in three dimensions, and with high sensitivity.

Novel routes towards finding the “GFP” of MRI have been laid out by VanZijil P and coworkers with DIACEST agents as well as Pagel M and coworkers with PARACEST, their ability to obtain multiple target differentiation along with internal controls puts researchers a step closer towards achieving the goal of “histological MR imaging” (Ali, Liu, Shah, Flask, & Pagel, 2009; McMahon, et al., 2008). Multiple color MRI has been accomplished only with the use of diamagnetic chemical exchange saturation transfer (DIACEST) techniques. McMahon et al developed an array of color based on small changes on the exchangeable protons of different diamagnetic peptides. Peptides with different exchange rates resulting from aminoacids such as lysine, serine, arginine and threonine, were separated by their individual off-resonance frequencies. This very elegant and powerful technique provides with the capability to separate different targets within the same MR image (McMahon, et al., 2008).

With the same goal of separating different targets within the same image and the addition of color, I use the capability to tune relaxivity within the apoferritin cavity in order to obtain “colored particles”. By separating the  $r_2/r_1$  of

different particles, it is possible to detect each particle separately by performing several sequential scans with different TE/TR combinations.

The following spin echo equation was used to simulate and predict the point where each particle starts to “null” itself.

$$S = M_0(1 - 2e^{-(TR-TE/2)/T_1} + e^{-TR/T_1})e^{-TE/T_2} \quad \text{Eqn.22}$$

$$\Delta S = \frac{S - S(0)}{S(0)} \times 100 \quad \text{Eqn.23}$$

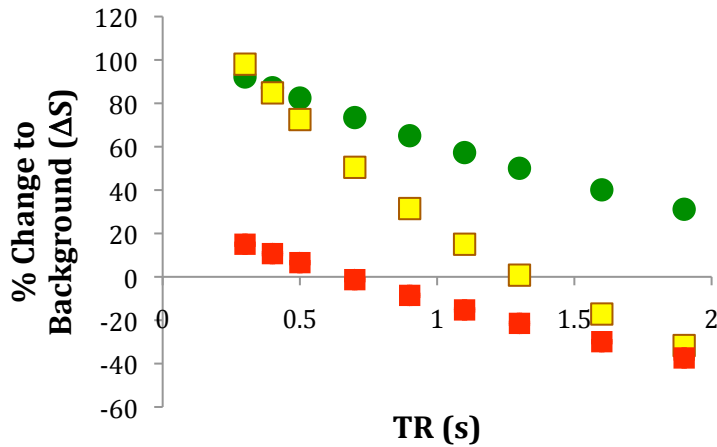


Figure 32. Simulation of percent signal change with respect to background. Red color has  $r_1= 2200\text{mM}^{-1}\text{s}^{-1}$  and  $r_2= 100100\text{mM}^{-1}\text{s}^{-1}$ . Yellow has  $r_1= 4500\text{mM}^{-1}\text{s}^{-1}$  and  $r_2= 40000\text{mM}^{-1}\text{s}^{-1}$ . Green has  $r_1= 3950\text{mM}^{-1}\text{s}^{-1}$   $r_2= 9500\text{mM}^{-1}\text{s}^{-1}$ . 100nM concentration of particles.

The relaxivities used in the simulations were representative of the Mn-magnetoferritin, MnWFe, and WFe particles. However, the relaxivities *in vivo* are dependent of the static magnetic field strength.

Two colors were tested *in vitro* on an agar phantom at different concentrations. Figure 33 below illustrates that the experimental measurements at 7T are in close agreement with the simulated data. The simulation is in very good agreement with the experimental data. Yellow particles are to be included in the experiment to distinguish three colors.

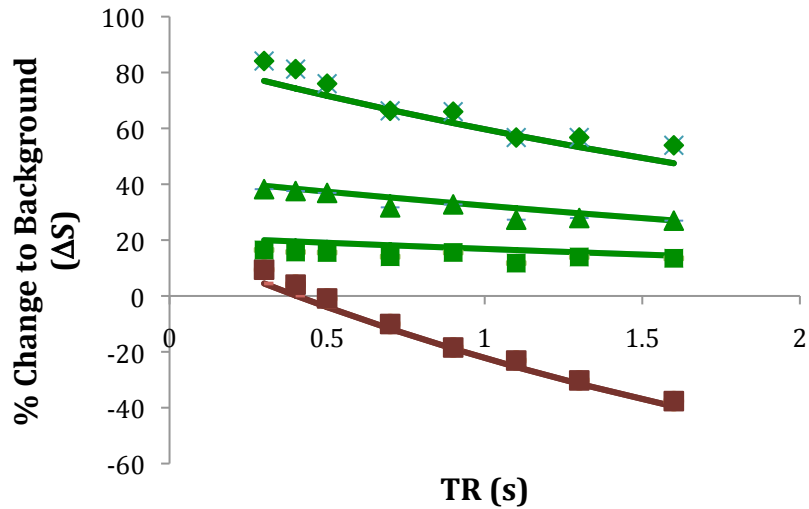


Figure 33. Lines represent simulated data with their respective relaxivities at 7T and filled markers are measured signal coming from a phantom. The multiple green lines represent different concentrations of contrast agent.

Figure 34 shows a preliminary *in vitro* experiment, where the green and red particles were imaged at varying TE/TR. Using a Matlab fitting tool it is possible to distinguish the cross-over points or lack there of at different concentrations for the particles.

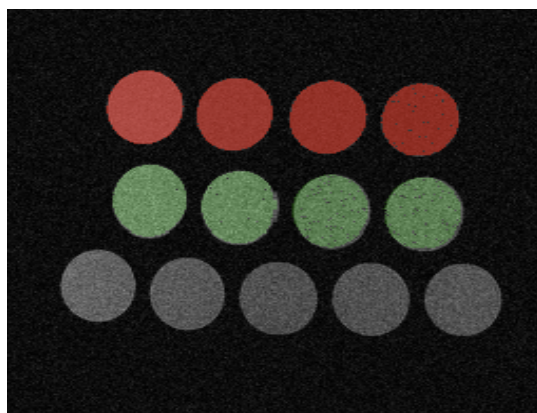


Figure 34. Post Processing of algorithm with Matlab to distinguish red and green-line crossover point. Red and green particles can be differentiated at different concentrations over background

Future work includes the addition of the yellow color into the scheme of agents and *in vivo* investigations. This novel acquisition technique could provide the ability to add color to MRI images to sensitively detect multiple targets (10s to 100s of nanomolar) at the same time in the same scan and using the same endogenous particle platform.

### 6.2.2 Cell Labeling with WFe-Apoferritin Nanoparticles

Nanomaterials can also be given both diagnostic and therapeutic capability, and imaging agents will simultaneously enable tracking of therapy. As the field evolves in conjunction with an increased understanding of basic biology and disease, novel applications will be identified that will take advantage of these agents or present opportunities to develop new ones. One area of major interest is in tracking cells that have been labeled with nanometer- to micron-sized superparamagnetic particles for MRI (Bulte, 2009; Cromer Berman, Walczak, & Bulte; Heyn, et al., 2006; Hill, et al., 2003; Nkansah, Thakral, & Shapiro; Rodriguez, et al., 2006; Shapiro, Sharer, Skrtic, & Koretsky, 2006; Shapiro,

Skrtic, & Koretsky, 2005; Tang & Shapiro). In a notable example of the potential for cell tracking, “magnetovaccination” has been recently developed to facilitate cell-to-cell transfer of labeled magnetic antigens on a tumor and subsequent detection by immune cell accumulation in the lymph nodes (Long, van Laarhoven, Bulte, & Levitsky, 2009). Future work would include the use of the WFe-apoferritin nanoparticles for cell labeling and tracking. Multiple experiments to evaluate the labeling efficiency in cells, and possible decrease in relaxivity due to cell compartmentalization need to be performed. A new relaxivity metric for in-cell particles may need to be introduced. Finally, implementing the aforementioned colored particles, multiple cell populations could be tracked simultaneously *in vivo*.

### 6.2.3 Chemical Doping with Different Ligands

As it was mentioned in this thesis, chemical doping with tungstate ligands allowed the formation of glass-like spin systems rendering amorphous crystals. This spin arrangement lead to an increased  $r_1$  and decreased  $r_2$  due to disruption of long range order and reduction of magnetic susceptibility to the paramagnetic regime. As shown in the introductory section, low spin  $\text{Fe}^{3+}$  systems result in  $1\mu_B$  uncoupled moments per atom. Thus, it is only evident that the paramagnetic susceptibility could be maximized if a higher paramagnetic moment could remain uncoupled per atom. This could be achieved either by using ligands with different symmetry resulting in smaller transitions (i.e. tetrahedral phosphates) or by doping lanthanide-oxide crystals, thus, having a large atomic moment. This could be accomplished by complexing a strong field ligand to  $\text{Gd}^{3+}$  or  $\text{Eu}^{3+}$  as shown by Barbosa and co-workers (Barbosa, et al., 2010).

## REFERENCES

- Accardo, A., Tesauro, D., Morelli, G., Gianolio, E., Aime, S., Vaccaro, M., et al. (2007). High-relaxivity supramolecular aggregates containing peptides and Gd complexes as contrast agents in MRI. *Journal of Biological Inorganic Chemistry*, 12(4843097519094366957related:7QlypogjNkMJ), 267-276.
- Aime, S., Castelli, D. D., Crich, S. G., Gianolio, E., & Terreno, E. (2009). Pushing the sensitivity envelope of lanthanide-based magnetic resonance imaging (MRI) contrast agents for molecular imaging applications. *Acc Chem Res*, 42(7), 822-831.
- Aime, S., Frullano, L., & Geninatti Crich, S. (2002). Compartmentalization of a gadolinium complex in the apoferritin cavity: a route to obtain high relaxivity contrast agents for magnetic resonance imaging. *Angew Chem Int Ed Engl*, 41(6), 1017-1019.
- Ali, M. Meser, Liu, Guanshu, Shah, Tejas, Flask, Chris A., & Pagel, Mark D. (2009). Using Two Chemical Exchange Saturation Transfer Magnetic Resonance Imaging Contrast Agents for Molecular Imaging Studies. *Accounts of Chemical Research*, 42(7), 915-924.
- Allen, M., Bulte, J. W., Liepold, L., Basu, G., Zywicke, H. A., Frank, J. A., et al. (2005). Paramagnetic viral nanoparticles as potential high-relaxivity magnetic resonance contrast agents. *Magn Reson Med*, 54(4), 807-812.
- Arosio, P., Ingrassia, R., & Cavadini, P. (2009). Ferritins: a family of molecules for iron storage, antioxidation and more. *Biochim Biophys Acta*, 1790(7), 589-599.
- Artemov, D., Mori, N., Okollie, B., & Bhujwalla, Z. M. (2003). MR molecular imaging of the Her-2/neu receptor in breast cancer cells using targeted iron oxide nanoparticles. *Magn Reson Med*, 49(3), 403-408.
- Barbosa, A. J., Maia, L. J. Q., Montanari, B., Goncalves, R. R., Messaddeq, Y., Ferreira, R. A. S., et al. (2010). Enhanced Eu<sup>3+</sup> Emission in Aqueous Phosphotungstate Colloidal Systems: Stabilization of Polyoxometalate Nanostructures. *Langmuir*, 26(17), 14170-14176.
- Beeman, S. C., Georges, J. F., & Bennett, K. M. Toxicity, biodistribution, and ex vivo MRI detection of intravenously injected cationized ferritin. *Magn Reson Med*.
- Beeman, S. C., Georges, J. F., & Bennett, K. M. (2012). Toxicity, biodistribution, and ex vivo MRI detection of intravenously injected cationized ferritin. *Magn Reson Med*.

- Beeman, S. C., Zhang, M., Gubhaju, L., Wu, T., Bertram, J. F., Frakes, D. H., et al. Measuring glomerular number and size in perfused kidneys using MRI. *Am J Physiol Renal Physiol*, 300(6), F1454-1457.
- Bennett, K. M., Shapiro, E. M., Sotak, C. H., & Koretsky, A. P. (2008). Controlled aggregation of ferritin to modulate MRI relaxivity. *Biophys J*, 95(1), 342-351.
- Bennett, K. M., Zhou, H., Sumner, J. P., Dodd, S. J., Bouraoud, N., Doi, K., et al. (2008). MRI of the basement membrane using charged nanoparticles as contrast agents. *Magn Reson Med*, 60(3), 564-574.
- Best, M. D. (2009). Click chemistry and bioorthogonal reactions: unprecedented selectivity in the labeling of biological molecules. *Biochemistry*, 48(28), 6571-6584.
- Bobo, R.H, Laske, D.W, Akbasak, A, Morrison, P.F, Dedrick, R.L, & Oldfield, E.H (1994). Convection-enhanced delivery of macromolecules in the brain. *Proceedings of the National Academy of Sciences of the United States of America*, 91(6), 2076.
- Brannon-Peppas, L., & Blanchette, J. O. (2004). Nanoparticle and targeted systems for cancer therapy. [Review]. *Adv Drug Deliv Rev*, 56(11), 1649-1659.
- Brooks, R. A., Moiny, F., & Gillis, P. (2001). On T2-shortening by weakly magnetized particles: the chemical exchange model. *Magn Reson Med*, 45(6), 1014-1020.
- Bulte, J. W. (2009). In vivo MRI cell tracking: clinical studies. *AJR Am J Roentgenol*, 193(2), 314-325.
- Bulte, J. W., Douglas, T., Mann, S., Frankel, R. B., Moskowitz, B. M., Brooks, R. A., et al. (1994). Magnetoferritin. Biomineralization as a novel molecular approach in the design of iron-oxide-based magnetic resonance contrast agents. *Invest Radiol*, 29 Suppl 2, S214-216.
- Bulte, J. W., Douglas, T., Mann, S., Frankel, R. B., Moskowitz, B. M., Brooks, R. A., et al. (1994). Magnetoferritin: characterization of a novel superparamagnetic MR contrast agent. *J Magn Reson Imaging*, 4(3), 497-505.
- Bulte, J. W., Douglas, T., Mann, S., Vymazal, J., Laughlin, P. G., & Frank, J. A. (1995). Initial assessment of magnetoferritin biokinetics and proton relaxation enhancement in rats. *Acad Radiol*, 2(10), 871-878.
- Bumb, A., Brechbiel, M. W., & Choyke, P. Macromolecular and dendrimer-based magnetic resonance contrast agents. *Acta Radiol*, 51(7), 751-767.

- Caravan, P., Farrar, C. T., Frullano, L., & Uppal, R. (2009). Influence of molecular parameters and increasing magnetic field strength on relaxivity of gadolinium- and manganese-based T1 contrast agents. *Contrast Media Mol Imaging*, 4(2), 89-100.
- Choi, J.H., Nguyen, F.T., Barone, P.W., Heller, D.A., Moll, A.E., Patel, D., et al. (2007). Multimodal biomedical imaging with asymmetric single-walled carbon nanotube/iron oxide nanoparticle complexes. *Nano Lett*, 7(4), 861-867.
- Colliex, C., Manoubi, T., & Ortiz, C. (1991). Electron-Energy-Loss-Spectroscopy near-Edge Fine-Structures in the Iron-Oxygen System. *Physical Review B*, 44(20), 11402-11411.
- Cormode, D. P., Jarzyna, P. A., Mulder, W. J., & Fayad, Z. A. Modified natural nanoparticles as contrast agents for medical imaging. *Adv Drug Deliv Rev*, 62(3), 329-338.
- Cormode, D. P., Jarzyna, P. A., Mulder, W. J., & Fayad, Z. A. (2009). Modified natural nanoparticles as contrast agents for medical imaging. *Adv Drug Deliv Rev*, 62(3), 329-338.
- Cranfield, C. G., Dawe, A., Karloukovski, V., Dunin-Borkowski, R. E., de Pomerai, D., & Dobson, J. (2004). Biogenic magnetite in the nematode *Caenorhabditis elegans*. *Proc Biol Sci*, 271 Suppl 6, S436-439.
- Cromer Berman, S. M., Walczak, P., & Bulte, J. W. Tracking stem cells using magnetic nanoparticles. *Wiley Interdiscip Rev Nanomed Nanobiotechnol*, 3(4), 343-355.
- Danon, D., Goldstein, L., Marikovsky, Y., & Skutelsky, E. (1972). Use of cationized ferritin as a label of negative charges on cell surfaces. *J Ultrastruct Res*, 38(5), 500-510.
- Dilnawaz, F., Singh, A., Mohanty, C., & Sahoo, S. K. (2010). Dual drug loaded superparamagnetic iron oxide nanoparticles for targeted cancer therapy. *Biomaterials*, 31(13), 3694-3706.
- Faraj, A. Al, Cieslar, K., Lacroix, G., Gaillard, S., Canet-Soulas, E., & Cremillieux, Y. (2009). In vivo imaging of carbon nanotube biodistribution using magnetic resonance imaging. *Nano Lett*, 9(3), 1023-1027.
- Figueiredo, S., Moreira, J. N., & Geraldes, Cfgc Supramolecular Protamine/Gd-loaded Liposomes Adducts as Relaxometric Protease responsive probes. *Bioorganic & Medicinal*.
- Frias, JC, Williams, KJ, Fisher, EA, & Fayad, Zahi A (2004). Recombinant HDL-like nanoparticles: a specific contrast agent for MRI of atherosclerotic plaques. *J. Am. Chem. Soc.*

- Geninatti Crich, S., Bussolati, B., Tei, L., Grange, C., Esposito, G., Lanzardo, S., et al. (2006). Magnetic resonance visualization of tumor angiogenesis by targeting neural cell adhesion molecules with the highly sensitive gadolinium-loaded apoferritin probe. *Cancer Res*, 66(18), 9196-9201.
- Gunn, J., Wallen, H., Veiseh, O., Sun, C., Fang, C., Cao, J., et al. (2008). A multimodal targeting nanoparticle for selectively labeling T cells. *Small*, 4(6), 712-715.
- Haacke M, Brown R, Thompson M, Venkatesan R (1999a). *Magnetic Resonance Imaging - Physical Principles and Sequence Design* (Vol. 1). Hoboken: John Wiley & Sons, Inc.
- Haacke M, Brown R, Thompson M, Venkatesan R (1999b). *Magnetic Resonance Imaging - Physical Principles and Sequence Design*. Hoboken: John Wiley & Sons, Inc.
- Haacke M, Brown RW (1999). In : *Magnetic Resonance Imaging: Physical Principles and Sequence Design*. John Wiley and Sons.
- Handl, H.L., Sankaranarayanan, R., Josan, J.S., Vagner, J., Mash, E.A., Gillies, R.J., et al. (2007). Synthesis and evaluation of bivalent NDP-alpha-MSH(7) peptide ligands for binding to the human melanocortin receptor 4 (hMC4R). *Bioconjug Chem*, 18(4), 1101-1109.
- Harris, J. M., & Chess, R. B. (2003). Effect of pegylation on pharmaceuticals. *Nat Rev Drug Discov*, 2(3), 214-221.
- Hein, C. D., Liu, X. M., & Wang, D. (2008). Click chemistry, a powerful tool for pharmaceutical sciences. *Pharm Res*, 25(10), 2216-2230.
- Hermanson, G. T. (2008). *Bioconjugate Techniques*. London, UK: Elsevier Inc.
- Heyn, C., Ronald, J. A., Mackenzie, L. T., MacDonald, I. C., Chambers, A. F., Rutt, B. K., et al. (2006). In vivo magnetic resonance imaging of single cells in mouse brain with optical validation. *Magn Reson Med*, 55(1), 23-29.
- Hill, J. M., Dick, A. J., Raman, V. K., Thompson, R. B., Yu, Z. X., Hinds, K. A., et al. (2003). Serial cardiac magnetic resonance imaging of injected mesenchymal stem cells. *Circulation*, 108(8), 1009-1014.
- Hofer, F. (1991). Determination of Inner-Shell Cross-Sections for Eels-Quantification. *Microscopy Microanalysis Microstructures*, 2(2-3), 215-230.
- Hogemann, D., Josephson, L., Weissleder, R., & Basilion, J. P. (2000). Improvement of MRI probes to allow efficient detection of gene expression. *Bioconjug Chem*, 11(6), 941-946.

- Hynynen, K. (2008). Ultrasound for drug and gene delivery to the brain. *Adv Drug Deliv Rev*, 60(10), 1209-1217.
- Jain, T. K., Richey, J., Strand, M., Leslie-Pelecky, D. L., Flask, C. A., & Labhassetwar, V. (2008). Magnetic nanoparticles with dual functional properties: drug delivery and magnetic resonance imaging. *Biomaterials*, 29(29), 4012-4021.
- Johansson, B.B. (1992). Experimental models of altering the blood brain barrier. *Prog Brain Res*, 91, 171-175.
- Jolck, R. I., Feldborg, L. N., Andersen, S., Moghimi, S. M., & Andresen, T. L. (2011). Engineering liposomes and nanoparticles for biological targeting. *Adv Biochem Eng Biotechnol*, 125, 251-280.
- Jordan, V. C., Caplan, M. R., & Bennett, K. M. Simplified synthesis and relaxometry of magnetoferritin for magnetic resonance imaging. *Magn Reson Med*, 64(5), 1260-1266.
- Jun, Y. W., Seo, J. W., & Cheon, J. (2008). Nanoscaling laws of magnetic nanoparticles and their applicabilities in biomedical sciences. *Acc Chem Res*, 41(2), 179-189.
- Kalman, F. K., Geninatti-Crich, S., & Aime, S. Reduction/dissolution of a beta-MnOOH nanophase in the ferritin cavity to yield a highly sensitive, biologically compatible magnetic resonance imaging agent. *Angew Chem Int Ed Engl*, 49(3), 612-615.
- Kalman, F. K., Geninatti-Crich, S., & Aime, S. (2010). Reduction/dissolution of a beta-MnOOH nanophase in the ferritin cavity to yield a highly sensitive, biologically compatible magnetic resonance imaging agent. *Angew Chem Int Ed Engl*, 49(3), 612-615.
- Karfeld, L.S., Bull, S.R., Davis, N.E., Meade, T.J., & Barron, A.E. (2007). Use of a genetically engineered protein for the design of a multivalent MRI contrast agent. *Bioconjug Chem*, 18(6), 1697-1700.
- Kasyutich O, Sarua A, Schwarzacher W (2008). Bioengineered magnetic crystals. *Journal of Physics D: Applied Physics*, 41(2008), 1-3.
- Kim, B. H., Lee, N., Kim, H., An, K., Park, Y. I., Choi, Y., et al. (2011). Large-scale synthesis of uniform and extremely small-sized iron oxide nanoparticles for high-resolution T1 magnetic resonance imaging contrast agents. *J Am Chem Soc*, 133(32), 12624-12631.
- Kim, T., Cho, E. J., Chae, Y., Kim, M., Oh, A., Jin, J., et al. Urchin-shaped manganese oxide nanoparticles as pH-responsive activatable T1 contrast agents for magnetic resonance imaging. *Angew Chem Int Ed Engl*, 50(45), 10589-10593.

- Kim, T., Momin, E., Choi, J., Yuan, K., Zaidi, H., Kim, J., et al. Mesoporous silica-coated hollow manganese oxide nanoparticles as positive T1 contrast agents for labeling and MRI tracking of adipose-derived mesenchymal stem cells. *J Am Chem Soc*, 133(9), 2955-2961.
- Kinoshita, M. (2006). Targeted drug delivery to the brain using focused ultrasound. *Top Magn Reson Imaging*, 17(3), 209-215.
- Kohler, N., Fryxell, G. E., & Zhang, M. (2004). A bifunctional poly(ethylene glycol) silane immobilized on metallic oxide-based nanoparticles for conjugation with cell targeting agents. *J Am Chem Soc*, 126(23), 7206-7211.
- Kolb, H. C., Finn, M. G., & Sharpless, K. B. (2001). Click Chemistry: Diverse Chemical Function from a Few Good Reactions. *Angew Chem Int Ed Engl*, 40(11), 2004-2021.
- Lee, J. H., Huh, Y. M., Jun, Y., Seo, J., Jang, J., Song, H. T., et al. (2007). Artificially engineered magnetic nanoparticles for ultra-sensitive molecular imaging. *Nature Medicine*, 13(1), 95-99.
- Levi, S., Luzzago, A., Cesareni, G., Cozzi, A., Franceschinelli, F., Albertini, A., et al. (1988). Mechanism of ferritin iron uptake: activity of the H-chain and deletion mapping of the ferro-oxidase site. A study of iron uptake and ferro-oxidase activity of human liver, recombinant H-chain ferritins, and of two H-chain deletion mutants. *J Biol Chem*, 263(34), 18086-18092.
- Li, B., Martin, A.L., & Gillies, E.R. (2007). Multivalent polymer vesicles via surface functionalization. *Chem Commun (Camb)*, 48, 734-741.
- Liu, Christina H, D'arceuil, Helen E, & De Crespigny, Alex J (2004). Direct CSF injection of MnCl<sub>2</sub> for dynamic manganese-enhanced MRI. *Magn Reson Med*, 51(5), 978-987.
- Liu, H.L., Hua, M.Y., Yang, H.W., Huang, C.Y., Chu, P.C., Wu, J.S., et al. (2010). Magnetic resonance monitoring of focused ultrasound/magnetic nanoparticle targeting delivery of therapeutic agents to the brain. *Proc Natl Acad Sci U S A*, 107(34), 15205-15210.
- Long, C. M., van Laarhoven, H. W., Bulte, J. W., & Levitsky, H. I. (2009). Magnetovaccination as a novel method to assess and quantify dendritic cell tumor antigen capture and delivery to lymph nodes. *Cancer Res*, 69(7), 3180-3187.
- Longmire, M., Choyke, P. L., & Kobayashi, H. (2008). Clearance properties of nano-sized particles and molecules as imaging agents: considerations and caveats. *Nanomedicine (Lond)*, 3(5), 703-717.
- Longmire, M., Choyke, P.L., & Kobayashi, H. (2008). Clearance properties of nano-sized particles and molecules as imaging agents: considerations and caveats. *Nanomedicine (Lond)*, 3(5), 703-717.

- Lonser RR, Walbridge S, Garmestani K, Butman JA, Walters HA, Vortmeyer AO, Morrison PF, Brechbiel MW, Oldfield EH (2002). Successful and safe perfusion of the primate brainstem: in vivo magnetic resonance imaging of macromolecular distribution during infusion. *Journal of Neurosurgery*, 97(4), 905-913.
- Lutz, J. F., & Zarafshani, Z. (2008). Efficient construction of therapeutics, bioconjugates, biomaterials and bioactive surfaces using azide-alkyne "click" chemistry. *Adv Drug Deliv Rev*, 60(9), 958-970.
- Madsen, S.J., & Hirschberg, H. (2010). Site-specific opening of the blood-brain barrier. *J. Biophotonics*, 3(5-6), 356-357.
- Maeda, H., Wu, J., Sawa, T., Matsumura, Y., & Hori, K. (2000). Tumor vascular permeability and the EPR effect in macromolecular therapeutics: a review. *J Control Release*, 65(1-2), 271-284.
- McElfresh, Mike (1994). *Fundamentals of Magnetism and Magnetic Measurements Featuring Quantum Design's Magnetic Property Measurement System*: Purdue University.
- McMahon, M. T., Gilad, A. A., DeLiso, M. A., Berman, S. M., Bulte, J. W., & van Zijl, P. C. (2008). New "multicolor" polypeptide diamagnetic chemical exchange saturation transfer (DIACEST) contrast agents for MRI. *Magn Reson Med*, 60(4), 803-812.
- Medarova, Z., Pham, W., Farrar, C., Petkova, V., & Moore, A. (2007). In vivo imaging of siRNA delivery and silencing in tumors. *Nat Med*, 13(3), 372-377.
- Meldrum, F. C., Douglas, T., Levi, S., Arosio, P., & Mann, S. (1995). Reconstitution of manganese oxide cores in horse spleen and recombinant ferritins. *J Inorg Biochem*, 58(1), 59-68.
- Meldrum, F. C., Heywood, B. R., & Mann, S. (1992). Magnetoferritin: in vitro synthesis of a novel magnetic protein. *Science*, 257(5069), 522-523.
- Miyawaki, J., Yudasaka, M., Imai, H., Yorimitsu, H., Isobe, H., Nakamura, E., et al. (2006). Synthesis of ultrafine Gd<sub>2</sub>O<sub>3</sub> nanoparticles inside single-wall carbon nanotubes. *J Phys Chem B*, 110(11), 5179-5181.
- Moghimi, S. M., Hunter, A. C., & Murray, J. C. (2001). Long-circulating and target-specific nanoparticles: theory to practice. *Pharmacol Rev*, 53(2), 283-318.
- Na, H. B., Lee, J. H., An, K., Park, Y. I., Park, M., Lee, I. S., et al. (2007). Development of a T1 contrast agent for magnetic resonance imaging using MnO nanoparticles. *Angew Chem Int Ed Engl*, 46(28), 5397-5401.

- Nasongkla, Norased, Bey, Erik, Ren, Jimin, Ai, Hua, Khemtong, Chalermchai, Guthi, Jagadeesh Setti, et al. (2006). Multifunctional polymeric micelles as cancer-targeted, MRI-ultrasensitive drug delivery systems. *Nano Lett*, 6(11), 2427-2430.
- Nkansah, M. K., Thakral, D., & Shapiro, E. M. Magnetic poly(lactide-co-glycolide) and cellulose particles for MRI-based cell tracking. *Magn Reson Med*, 65(6), 1776-1785.
- O'Handley, Robert (2000). *Modern magnetic materials: principles and applications*. New York: John Wiley & Sons, INc.
- Passaniti, A., & Roth, T. F. (1989). Coated vesicles from chicken liver bind ferritin. *J Cell Sci*, 92 ( Pt 2), 187-196.
- Pepperhoff, W, & Ancet, M (2001). *Constitution and Magnetism of Iron and its Alloys* New York: Springer.
- Querol, M., & Bogdanov, A., Jr. (2006). Amplification strategies in MR imaging: activation and accumulation of sensing contrast agents (SCAs). *J Magn Reson Imaging*, 24(5), 971-982.
- Rodriguez, O., Fricke, S., Chien, C., Dettin, L., VanMeter, J., Shapiro, E., et al. (2006). Contrast-enhanced in vivo imaging of breast and prostate cancer cells by MRI. *Cell Cycle*, 5(1), 113-119.
- Sana, B., Poh, C. L., & Lim, S. A manganese-ferritin nanocomposite as an ultrasensitive T2 contrast agent. *Chem Commun (Camb)*, 48(6), 862-864.
- Schellenberger, E. A., Sosnovik, D., Weissleder, R., & Josephson, L. (2004). Magneto/optical annexin V, a multimodal protein. *Bioconjug Chem*, 15(5), 1062-1067.
- Schellenberger, E. A., Weissleder, R., & Josephson, L. (2004). Optimal modification of annexin V with fluorescent dyes. *Chembiochem*, 5(3), 271-274.
- Schellenberger, E., Schnorr, J., Reutelingsperger, C., Ungethum, L., Meyer, W., Taupitz, M., et al. (2008). Linking proteins with anionic nanoparticles via protamine: ultrasmall protein-coupled probes for magnetic resonance imaging of apoptosis. *Small*, 4(2), 225-230.
- Seo, W. S., Lee, J. H., Sun, X., Suzuki, Y., Mann, D., Liu, Z., et al. (2006). FeCo/graphitic-shell nanocrystals as advanced magnetic-resonance-imaging and near-infrared agents. *Nat Mater*, 5(12), 971-976.
- Seo, WS., Lee, JH, Sun, X., Suzuki, Y., Mann, D., Liu, Z., et al. (2006). FeCo/graphitic-shell nanocrystals as advanced magnetic resonance-imaging and near-infrared agents. *Nat Materials*, 5, 971-976.

- Shapiro, E. M., Sharer, K., Skrtic, S., & Koretsky, A. P. (2006). In vivo detection of single cells by MRI. *Magn Reson Med*, 55(2), 242-249.
- Shapiro, E. M., Skrtic, S., & Koretsky, A. P. (2005). Sizing it up: cellular MRI using micron-sized iron oxide particles. *Magn Reson Med*, 53(2), 329-338.
- Shaw, J. L., Wright, A. C., Sinclair, R. N., Marasinghe, G. K., Holland, D., Lees, M. R., et al. (2004). Spin glass-like antiferromagnetic interactions in iron phosphate glasses. *Journal of Non-Crystalline Solids*, 345, 245-250.
- Silverthorn, Dee Unglaub (2004). *Human Physiology an Integrated Approach* (3rd ed.): Pearson.
- Sitharaman, B., Kissell, K.R., Hartman, K.B., Tran, L.A., Baikalov, A., Rusakova, I., et al. (2005). Superparamagnetic gadonanotubes are high-performance MRI contrast agents. *Chem Commun (Camb)*, 31, 3915-3917.
- Sitharaman, B., & Wilson, L.J. (2006). Gadonanotubes as new high-performance MRI contrast agents. *Int J Nanomedicine*, 1(3), 291-295.
- Song, Y., Kohlmeir, E.K., & Meade, T.J. (2008). Synthesis of multimeric MR contrast agents for cellular imaging. *J Am Chem Soc*, 130(21), 6662-6663.
- Sperling, R. A., & Parak, W. J. (2010). Surface modification, functionalization and bioconjugation of colloidal inorganic nanoparticles. *Philos Transact A Math Phys Eng Sci*, 368(1915), 1333-1383.
- Stanisz, G. J., Odrobina, E. E., Pun, J., Escaravage, M., Graham, S. J., Bronskill, M. J., et al. (2005). T1, T2 relaxation and magnetization transfer in tissue at 3T. *Magn Reson Med*, 54(3), 507-512.
- Stich, T. A., Lahiri, S., Yeagle, G., Dicus, M., Brynda, M., Gunn, A., et al. (2007). Multifrequency Pulsed EPR Studies of Biologically Relevant Manganese(II) Complexes. *Appl Magn Reson*, 31(1-2), 321-341.
- Sun, C., Veiseh, O., Gunn, J., Fang, C., Hansen, S., Lee, D., et al. (2008). In vivo MRI detection of gliomas by chlorotoxin-conjugated superparamagnetic nanoprobe. *Small*, 4(3), 372-379.
- Tang, K. S., & Shapiro, E. M. Enhanced magnetic cell labeling efficiency using -NH<sub>2</sub> coated MPIOs. *Magn Reson Med*, 65(6), 1564-1569.
- Taylor, K. M., Rieter, W. J., & Lin, W. (2008). Manganese-based nanoscale metal-organic frameworks for magnetic resonance imaging. *J Am Chem Soc*, 130(44), 14358-14359.

- Uchida, M., Terashima, M., Cunningham, C. H., Suzuki, Y., Willits, D. A., Willis, A. F., et al. (2008). A human ferritin iron oxide nano-composite magnetic resonance contrast agent. *Magn Reson Med*, 60(5), 1073-1081.
- Vasalatiy, O., Zhao, P., Zhang, S., Aime, S., & Sherry, A. D. (2006). Catalytic effects of apoferritin interior surface residues on water proton exchange in lanthanide complexes. *Contrast Media & Molecular Imaging*, 1(1), 10-14.
- Weiseh, O., Gunn, J. W., & Zhang, M. Q. (2010). Design and fabrication of magnetic nanoparticles for targeted drug delivery and imaging. *Advanced Drug Delivery Reviews*, 62(3), 284-304.
- Weiseh, O., Sun, C., Gunn, J., Kohler, N., Gabikian, P., Lee, D., et al. (2005). Optical and MRI multifunctional nanoprobe for targeting gliomas. *Nano Lett*, 5(6), 1003-1008.
- von Maltzahn, G., Ren, Y., Park, J. H., Min, D. H., Kotamraju, V. R., Jayakumar, J., et al. (2008). In vivo tumor cell targeting with "click" nanoparticles. *Bioconjug Chem*, 19(8), 1570-1578.
- Wang, A. Z., Bagalkot, V., Vasilliou, C. C., Gu, F., Alexis, F., Zhang, L., et al. (2008). Superparamagnetic iron oxide nanoparticle-aptamer bioconjugates for combined prostate cancer imaging and therapy. *ChemMedChem*, 3(9), 1311-1315.
- Wardeska, J. G., Viglione, B., & Chasteen, N. D. (1986). Metal ion complexes of apoferritin. Evidence for initial binding in the hydrophilic channels. *J Biol Chem*, 261(15), 6677-6683.
- Webb, B., Frame, J., Zhao, Z., Lee, M. L., & Watt, G. D. (1994). Molecular entrapment of small molecules within the interior of horse spleen ferritin. *Arch Biochem Biophys*, 309(1), 178-183.
- Weil, J.A, Bolton, J.R, & Wertz, J.E (1994). *Electron Paramagnetic Resonance. Elementary Theory and Practical Applications*. New York: John Wiley & Sons.
- Weissleder, R., Kelly, K., Sun, E. Y., Shtatland, T., & Josephson, L. (2005). Cell-specific targeting of nanoparticles by multivalent attachment of small molecules. *Nat Biotechnol*, 23(11), 1418-1423.
- Wiener, E. C., Brechbiel, M. W., Brothers, H., Magin, R. L., Gansow, O. A., Tomalia, D. A., et al. (1994). Dendrimer-based metal chelates: a new class of magnetic resonance imaging contrast agents. *Magn Reson Med*, 31(1), 1-8.
- Wong K.K.W, Douglas T, Gider S, Awschalom D.D., Mann S. (1998). Biomimetic Synthesis and Characterization of Magnetic Proteins (Magnetoferritin). *Chemistry of Materials*, 10(January 19, 1998), 279-285.

- Xu, L., Vagner, J., Alletti, R., Rao, V., Jagadish, B., Morse, D.L., et al. (2010). Synthesis and characterization of a Eu-DTPA-PEGO-MSH(4) derivative for evaluation of binding of multivalent molecules to melanocortin receptors. *Bioorg Med Chem Lett*, 20(8), 2489-2492.
- Xu, L., Vagner, J., Josan, J., Lynch, R.M., Morse, D.L., Baggett, B., et al. (2009). Enhanced targeting with heterobivalent ligands. *Mol Cancer Ther*, 8(8), 2356-2365.
- Yablonskiy, D. A., & Haacke, E. M. (1994). Theory of NMR signal behavior in magnetically inhomogeneous tissues: the static dephasing regime. *Magn Reson Med*, 32(6), 749-763.
- Yang, X., & Chasteen, N. D. (1999). Ferroxidase activity of ferritin: effects of pH, buffer and Fe(II) and Fe(III) concentrations on Fe(II) autoxidation and ferroxidation. *Biochem J*, 338 ( Pt 3), 615-618.
- Yiu, H. H., McBain, S. C., Lethbridge, Z. A., Lees, M. R., & Dobson, J. (2010). Preparation and characterization of polyethylenimine-coated Fe<sub>3</sub>O<sub>4</sub>-MCM-48 nanocomposite particles as a novel agent for magnet-assisted transfection. *J Biomed Mater Res A*, 92(1), 386-392.
- Yoon, T. J., Lee, H., Shao, H., Hilderbrand, S. A., & Weissleder, R. (2011). Multicore assemblies potentiate magnetic properties of biomagnetic nanoparticles. *Adv Mater*, 23(41), 4793-4797.
- Yu, M. K., Jeong, Y. Y., Park, J., Park, S., Kim, J. W., Min, J. J., et al. (2008). Drug-loaded superparamagnetic iron oxide nanoparticles for combined cancer imaging and therapy in vivo. *Angew Chem Int Ed Engl*, 47(29), 5362-5365.

APPENDIX A

IACUC PROTOCOL APPROVAL FOR ANIMAL EXPERIMENTATION

IACUC Use Only	
Date:	IACUC Protocol No.: 12-1235R

**ANIMAL USE PROTOCOL  
ARIZONA STATE UNIVERSITY INSTITUTIONAL ANIMAL CARE AND USE COMMITTEE  
(revised October 2011)**

Please read "Instructions for Completing the Animal Use Protocol" before completing. Upon approval, this protocol will become a public record so please follow instructions carefully.

**PROJECT/PROGRAM TITLE:** Extracellular Matrix Targeting MRI Contrast Agents

**SPECIES REQUESTED:** Rats and Mice

**I. PERSONNEL INFORMATION**

- A. A single member of the university faculty and/or Principal Investigator (PI) is considered the responsible individual.

NAME: Kevin M. Bennett TITLE: Assistant Prof.  
AFFILIATION: SBHSE Office Phone # 480-727-9790  
Cell Phone #: 443-789-8679 E-Mail: Kevin.m.bennett@asu.edu

- B. Additional contact, if any, for IACUC business

NAME: TITLE:  
AFFILIATION: Office Phone #  
Cell Phone #: E-Mail:

- C. Protocol Type

Non-funded research

Grant / Contract (Also submit grant proposal with this protocol)

Granting Agency: American Heart Association Deadline:  
Proposal Title: MRI-based techniques to measure whole-kidney nephron endowment  
ASU Proposal # or Award #: 12BGIA9840020  
Co-Investigator(s): Wu (Comp Sci), Bertram (Monash U)

APPENDIX B

LICENCES TO REPRODUCE COPYRIGHTED MATERIAL

**NATURE PUBLISHING GROUP LICENSE  
TERMS AND CONDITIONS**

Nov 05, 2012

This is a License Agreement between Maria V Clavijo Jordan ("You") and Nature Publishing Group ("Nature Publishing Group") provided by Copyright Clearance Center ("CCC"). The license consists of your order details, the terms and conditions provided by Nature Publishing Group, and the payment terms and conditions.

**All payments must be made in full to CCC. For payment instructions, please see information listed at the bottom of this form.**

License Number	3022331391361
License date	Nov 05, 2012
Licensed content publisher	Nature Publishing Group
Licensed content publication	Nature Medicine
Licensed content title	Artificially engineered magnetic nanoparticles for ultra-sensitive molecular imaging
Licensed content author	Jae-Hyun Lee ,Yong-Min Huh ,Young-wook Jun ,Jung-wook Seo ,Jung-tak Jang et al.
Licensed content date	Jan 1, 2007
Volume number	13
Issue number	1
Type of Use	reuse in a thesis/dissertation
Requestor type	academic/educational
Format	print and electronic
Portion	figures/tables/illustrations
Number of figures/tables/illustrations	1
High-res required	no
Figures	Figure 1
Author of this NPG article	no
Your reference number	
Title of your thesis / dissertation	Design of Apoferritin-Based Nanoparticle MRI Contrast Agents Through Controlled Metal Deposition
Expected completion date	Dec 2012
Estimated size (number of pages)	200
Total	0.00 USD

**JOHN WILEY AND SONS LICENSE  
TERMS AND CONDITIONS**

Oct 23, 2012

---

This is a License Agreement between Maria V Clavijo Jordan ("You") and John Wiley and Sons ("John Wiley and Sons") provided by Copyright Clearance Center ("CCC"). The license consists of your order details, the terms and conditions provided by John Wiley and Sons, and the payment terms and conditions.

**All payments must be made in full to CCC. For payment instructions, please see information listed at the bottom of this form.**

License Number	3015000422980
License date	Oct 23, 2012
Licensed content publisher	John Wiley and Sons
Licensed content publication	Wiley Interdisciplinary Reviews - Nanomedicine and Nanobiotechnology
Book title	
Licensed content author	Veronica Clavijo-Jordan, Vikram D. Kodibagkar, Scott C. Beeman, Bradley D. Hann, Kevin M. Bennett
Licensed content date	Apr 9, 2012
Start page	345
End page	365
Type of use	Dissertation/Thesis
Requestor type	Author of this Wiley article
Format	Print and electronic
Portion	Full article
Will you be translating?	No
Order reference number	
Total	0.00 USD

[Terms and Conditions](#)

**TERMS AND CONDITIONS**

This copyrighted material is owned by or exclusively licensed to John Wiley & Sons, Inc. or one of its group companies (each a "Wiley Company") or a society for whom a Wiley Company has exclusive publishing rights in relation to a particular journal (collectively WILEY). By clicking "accept" in connection with completing this licensing transaction, you agree that the following terms and conditions apply to this transaction (along with the billing and payment terms and conditions established by the Copyright Clearance Center Inc., ("CCC's Billing and Payment terms and conditions"), at the time that you opened your Rightslink account (these are available at any time at <http://myaccount.copyright.com>)

**JOHN WILEY AND SONS LICENSE  
TERMS AND CONDITIONS**

Nov 02, 2012

This is a License Agreement between Maria V Clavijo Jordan ("You") and John Wiley and Sons ("John Wiley and Sons") provided by Copyright Clearance Center ("CCC"). The license consists of your order details, the terms and conditions provided by John Wiley and Sons, and the payment terms and conditions.

**All payments must be made in full to CCC. For payment instructions, please see information listed at the bottom of this form.**

License Number	3020970878120
License date	Nov 02, 2012
Licensed content publisher	John Wiley and Sons
Licensed content publication	Magnetic Resonance in Medicine
Book title	
Licensed content author	Greg J. Stanisz,Ewa E. Odrobina,Joseph Pun,Michael Escaravage,Simon J. Graham,Michael J. Bronskill,R. Mark Henkelman
Licensed content date	Aug 5, 2005
Start page	507
End page	512
Type of use	Dissertation/Thesis
Requestor type	University/Academic
Format	Print and electronic
Portion	Figure/table
Number of figures/tables	1
Number of extracts	
Original Wiley figure/table number(s)	Table 1
Will you be translating?	No
Order reference number	
Total	0.00 USD

[Terms and Conditions](#)

**TERMS AND CONDITIONS**

This copyrighted material is owned by or exclusively licensed to John Wiley & Sons, Inc. or one of its group companies (each a "Wiley Company") or a society for whom a Wiley Company has

**JOHN WILEY AND SONS LICENSE  
TERMS AND CONDITIONS**

Oct 23, 2012

---

This is a License Agreement between Maria V Clavijo Jordan ("You") and John Wiley and Sons ("John Wiley and Sons") provided by Copyright Clearance Center ("CCC"). The license consists of your order details, the terms and conditions provided by John Wiley and Sons, and the payment terms and conditions.

**All payments must be made in full to CCC. For payment instructions, please see information listed at the bottom of this form.**

License Number	3015000274819
License date	Oct 23, 2012
Licensed content publisher	John Wiley and Sons
Licensed content publication	Magnetic Resonance in Medicine
Book title	
Licensed content author	Veronica Clavijo Jordan,Michael R. Caplan,Kevin M. Bennett
Licensed content date	Oct 26, 2010
Start page	1260
End page	1266
Type of use	Dissertation/Thesis
Requestor type	Author of this Wiley article
Format	Print and electronic
Portion	Full article
Will you be translating?	No
Order reference number	
Total	0.00 USD

[Terms and Conditions](#)

**TERMS AND CONDITIONS**

This copyrighted material is owned by or exclusively licensed to John Wiley & Sons, Inc. or one of its group companies (each a "Wiley Company") or a society for whom a Wiley Company has exclusive publishing rights in relation to a particular journal (collectively WILEY"). By clicking "accept" in connection with completing this licensing transaction, you agree that the following terms and conditions apply to this transaction (along with the billing and payment terms and conditions established by the Copyright Clearance Center Inc., ("CCC's Billing and Payment terms and conditions"), at the time that you opened your Rightslink account (these are available at any time at <http://myaccount.copyright.com>)

[Terms and Conditions](#)

APPENDIX C

STATEMENT OF PERMISSION FROM CO-AUTHORS

The co-authors of the following published articles have granted permission to re-use data, and text in this dissertation from the following articles.

“Simplified Synthesis and Relaxometry of Magnetoferritin for Magnetic Resonance Imaging”

“Principles and Emerging Applications of Nanomagnetic Materials in Medicine”